# MAGNETIZING THE UNIVERSE DURING THE EPOCH OF REIONIZATION

A Dissertation
Presented to
The Academic Faculty

By

Daegene Koh

In Partial Fulfillment
of the Requirements for the Degree
Doctor of Philosophy in the
School of Physics

Georgia Institute of Technology

May 2017

**MAGNETIZING THE UNIVERSE DURING THE EPOCH OF REIONIZATION**

Approved by:

Professor John Wise, Advisor
School of Physics
*Georgia Institute of Technology*

Professor Tamara Bogdanovic
School of Physics
*Georgia Institute of Technology*

Professor David Ballantyne
School of Physics
*Georgia Institute of Technology*

Professor Pablo Laguna
School of Physics
*Georgia Institute of Technology*

Professor Rachel Kuzio de Naray
Department of Physics & Astronomy
*Georgia State University*

Date Approved: March 27, 2017

## ACKNOWLEDGEMENTS

First, I'd like to thank my advisor John Wise, who supported my numerous venturous in astrophysics as well as my forays into completely non-academic realms. Under his mentorship, I've been able to explore the world of computational astrophysics while retaining the flexibility to develop skills in teaching as well as policy work. I am truly grateful to have John as my doctoral advisor.

I thank my proposal committee members David Ballantyne and Tamara Bogdanovic, who've provided guidance as needed throughout my career at Georgia Tech and also my full committee members Pablo Laguna and Rachel Kuzio de Naray for providing valuable feedback on this thesis. Of course, I have to acknowledge the members of the Center for Relativistic Astrophysics and in particular, I want to point out Deirdre Shoemaker and Pablo Laguna who provided me with many a late night libations.

Lastly, I thank my loving parents who trusted and supported me throughout this pursuit. I certainly could not have completed this work without their care and support.

## TABLE OF CONTENTS

## LIST OF TABLES

## LIST OF FIGURES

## SUMMARY

Magnetic fields are speculated to affect the collapse dynamics in early star formation to influence the IMF, which may be imprinted in the local metal-poor population. These fields arise by the amplification of primordial fields during the formation of the first stars (Pop III) and from their feedback. We study the former using MHD simulations with a uniform seed field from cosmological initial conditions to the formation and supernova of a Pop III star. We find that a weak seed field can be amplified to $\mu$G at the density peak and by a factor of 100 around the shell of the supernova shock. We also explored the dynamics of metal-poor mini-halos, enriched by Pop III supernova, in varying metallicities and Lyman-Werner flux to study the minimum collapse mass. Furthermore, Pop III stars are significant drivers of reionization at high redshift (z $>$10). We use semi-numeric methods including Pop III stars as ionizing sources and find smaller characteristic H II bubbles sizes while calculating an optical depth, $\tau_{\rm e} = 0.0569$, consistent with the latest results from Planck. The resulting ionization fields can efficiently model the ionizing UV background in cosmological simulations. These results are essential to building a full MHD simulation of the first galaxies.

# CHAPTER 1
# INTRODUCTION AND BACKGROUND

Starting with the mechanics as formulated by Isaac Newton, humans have attempted to use the rigors and rules of mathematics to discern the behavior of the physical world from the smallest of particles to the largest of cosmic structures. Despite the innumerable successes this particular approach has had, there is a realm of phenomena that is not as easily illuminated by interpreting a single or even a set of equations. This is the realm of non-linear dynamics which often deals with chaotic behaviors of systems that span a large range of scales. From the beating of the human heart, the whims of the weather, to the swirling plasmas in the depths of the universe, we are forced to make constant compromises between accuracy, interpretability, and even time to fully understand as we have done previously. Truly, it is a frontier of knowledge of humankind.

In this work, we concern ourselves with a specific portion of this frontier, namely, the physics of structure formation in the early universe. Starting from the Big Bang, the universe graduates from the physically, chemically, and thermodynamically simple linear phase, which one can parameterize with a small collection of well-suited values, to the turbulent expanse filled with sudden explosions and gargantuan objects that exist far beyond our terrestrial experience. This period can also be doubly viewed as an observational frontier as current state of the art instruments are incapable of directly capturing the details of this early time.

This is a tale of compromises between accuracy, interpretability, and time as we explore this frontier. But first, we must present some background.

## 1.1 Foundations of ΛCDM

Our understanding of modern cosmology has been largely shaped by a body of observations that support the existence of dark matter and dark energy. The former term was likely first coined by Henri Poincaré [1] who actually denied that dark matter, or matière obscure as he called it, should exist at all and posited that luminous matter should account for the entirety of the mass of galaxies. It was not until 1933, when Fritz Zwicky [2] used the virial theorem to estimate the mass of the Coma cluster only to find the mass to be 400 times greater than the mass of the observed luminous matter. He thus attributed the missing mass to dunkle Materie, or dark matter. Finally, Vera Rubin starting from the 1960s used galaxy rotation curves to demonstrate that the rotational velocities stay high, rather than decaying, far beyond the reach of the gravitational potential of the luminous matter implying that the bulk of the mass of galaxies must lie in dark matter [3].

Although subsequent observations have only further cemented the argument for dark matter, the precise nature of the individual particles that make up the material is still unknown. What is known is that the particles must be what is known as cold, as opposed to warm or hot. This refers not to the temperature of the particles but rather the thermal velocities. Hot dark matter refers to particles that must retain relativistic speeds at the time they decoupled from other matter and radiation [4]. However, such particles would result in large cluster-like structures that would subsequently fragment to form galaxies, in direct contrast to observational work [5]. Thus, alternative particles were considered, whose larger masses and lower thermal velocities would allow for a bottom-up structure formation scenario. The favored model is that of cold dark matter with masses on the order of 100 GeV, which provides a good match to observed clustering of galaxies [6]. Warm dark matter can also match observed clustering with the added of effect of suppressing the formation of dark

matter halos smaller than typical dwarf galaxy host halos. The biggest drawback to these models is that there is no clear candidate for particles that fit the warm dark matter energy range. The most promising candidate, thus, is a type of cold dark matter known as Weakly Interacting Massive Particles (WIMPs), which are supersymmetric particles that lie well within the mass range that is expected of cold dark matter. However, direct detection efforts by LUX and SuperCDMS have not been successful in a detection, resulting in a renewed interest in warm dark matter models.

The other key element in our understanding of the universe is dark energy. The first main evidence of its existence was considered after the discovery of a particular pattern found in the observations of Type Ia supernovae. These supernovae were spread apart further than was expected by cosmological models at the time, implying that the expansion of the universe is accelerating at the present day [7]. Perlmutter *et al.* [8] then took these data to estimate a value for the cosmological constant energy density, which we now interpret as dark energy. It is commonly known that Einstein had originally proposed the cosmological constant as an ad-hoc addition to the equations of general relativity to enforce a static universe. However, it was quickly discarded once it was observed that the universe appeared to be expanding [9], ruling out a static universe. The presence of this dark energy was further cemented by precise measurements of the Cosmic Microwave Background (CMB) which provided much information regarding the make up of the universe. In particular, only about 30% of the universe consists of baryonic and dark matter, leaving the larger 70% to dark energy.

Thus, it is with these discoveries that we find ourselves with the Lambda-Cold Dark Matter ($\Lambda$CDM) cosmology model as a framework to understand the universe, acknowledging that dark energy and dark matter dominate the dynamics of our universe. Figure 1.1 shows a cartoon schematic of this model. In this model, the universe

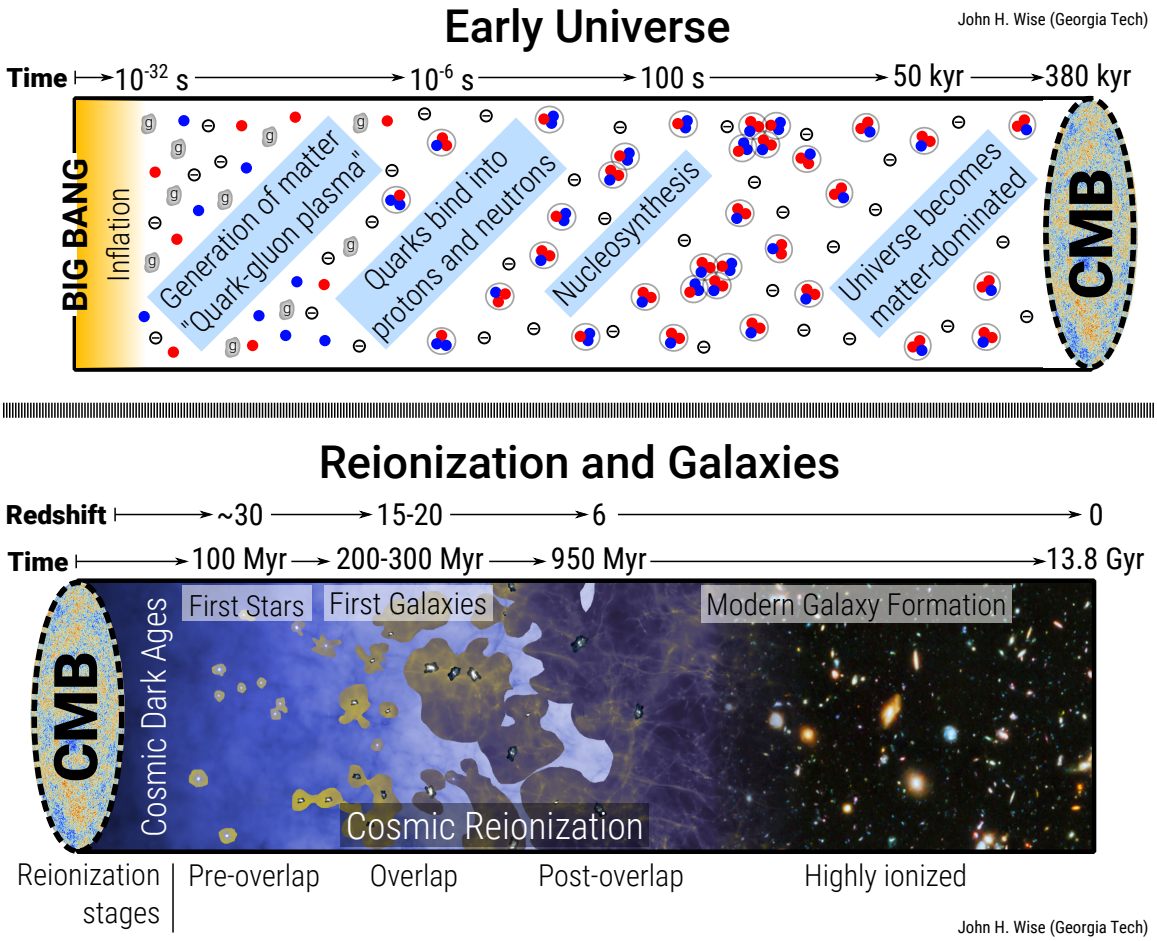


Figure 1.1: Time evolution of the universe in a ΛCDM cosmology. Top panel shows the phase transitions occurring from the Big Bang until recombination. Bottom panel shows structure formation starting from the emission of the CMB to the present day. Taken from Wise [10].

expanded from a singularity, or a point of infinite density and temperature, going through a period of exponential inflation while forming baryonic matter. Then the universe continued to expand and cool until the electrons recombined with protons to form atoms enabling photons to decouple from them. Finally, gravity begins to amplify the fluctuations in matter distribution to begin forming the zoo of the cosmic structures that are observed in the present universe.

### 1.1.1 Initial Conditions for Galaxy Formation

The focus of this work will be on this latest period in which stars and galaxies as we know them today form. To study this process, we require two things: an understanding of the initial conditions and a physical model for the evolution of the system.

Let us first consider the initial conditions. Without getting into details, we understand that the quantum fluctuations during cosmic inflation will result in Gaussian random fields of perturbations. This is particularly important because for Gaussian random fields, the power spectrum can describe the distribution entirely providing a powerful tool. For an average random volume of the universe, let us define the correlation function as

$$\xi(|\vec{x}_1 - \vec{x}_2|) = \left\langle \sigma(\vec{x}_1)\sigma(\vec{x}_2) \right\rangle \tag{1.1}$$

where $\xi$ is the two-point correlation function and $\sigma$ is the density field. Then, a density field can be given by the Fourier transform of the power spectrum as follows

$$\sigma(\vec{x}) = \frac{1}{(2\pi)^3} \int d^3k \sqrt{P(k)} \lambda_{\vec{k}} e^{i\vec{k}\cdot\vec{x}} \tag{1.2}$$

where $P$ is the power spectrum and $\lambda$ are complex random numbers that represent random amplitudes. Thus, if we have a measurement of the initial power spectrum, we

can simply scale a randomly generated field by it to generate a statistically identical set of initial conditions. Luckily, the CMB provides this information. This then provides the so-called cosmological initial conditions.

Now, we must evolve these initial conditions. We assume that the density perturbations in the universe evolve according to the equations of fluid dynamics. Below are the continuity, Euler, and Poisson equations expressed in comoving coordinates to account for the expansion of spacetime and recast in terms of overdensity $\sigma$

$$\frac{\partial \sigma}{\partial t} + \frac{1}{a}\nabla \cdot \left[(1+\sigma)\vec{v}\right] = 0 \tag{1.3}$$

$$\frac{\partial \vec{v}}{\partial t} + \frac{\dot{a}}{a}\vec{v} + \frac{1}{a}(\vec{v}\cdot\nabla)\vec{v} = -\frac{\nabla\Phi}{a} - \frac{\nabla P}{a\bar{\rho}(1+\sigma)} \tag{1.4}$$

$$\nabla^2\Phi = 4\pi G\bar{\rho}a^2\sigma, \Phi \equiv \sigma + a\ddot{a}x^2/2 \tag{1.5}$$

where a is the cosmological scale factor, $x$ is the position, $P$ is the pressure, $\vec{v}$ is the peculiar velocity, $\Phi$ is the gravitational potential, and $\bar{\rho}$ is the mean density. During the early universe, when the perturbations are small, we take the following assumption that the linear evolution of the perturbation grows as

$$\sigma(\vec{x}, a) = D(a)\sigma_i(\vec{x}) \tag{1.6}$$

where $D(a)$ is the growth factor [11]. This enables an efficient evolution of the initial conditions to a later redshift as long as we are still in the linear regime, for $\sigma \lesssim 0.2$.

In practice, galaxy formation can be studied starting from these initial conditions in a variety of ways, ranging from entirely analytic models all the way to completely numerical models. This work focuses primarily on the latter in which we use the currently known physics to numerically evaluate future timesteps starting from above cos-

mological initial conditions. In these cosmological simulations, there are two central components: dark matter and baryonic gas. Dark matter is most commonly treated by taking discretized mass samples represented by collisionless particles evolved by the Boltzmann equation

$$\frac{\partial f_i}{\partial t} + \dot{\vec{x}}\frac{\partial f_i}{\partial \vec{x}} + \ddot{\vec{x}}\frac{\partial f_i}{\partial \dot{\vec{x}}} = C \tag{1.7}$$

where $\vec{x}$ are positions of a given element, $f_i$ is the probability density function, and C is the collision integral which is set to 0 in the case of collisionless dark matter particles. The solution to this equation is given by the characteristic equations which are the simple Newtonian equations of motions

$$\frac{d\vec{x}}{dt} = \vec{u}, \frac{d\vec{u}}{dt} = -\nabla\Phi \tag{1.8}$$

where $\Phi$ is the gravitational potential given by the Poisson equation. This can then be evaluated to using a variety of numerical techniques. As dark matter interacts only gravitationally, we require no other physics to describe them.

On the other hand, baryonic physics are not limited to just gravitational interactions. Instead, they must be modeled with the full equations of hydrodynamics which include Equations 1.3,1.4,1.5, and also the energy equation given by

$$\frac{\partial}{\partial t}\left[\rho\left(\frac{v^2}{2} + \epsilon\right)\right] + \nabla\cdot\left[\rho\left(\frac{v^2}{2} + \frac{P}{\rho} + \epsilon\right)\vec{v}\right] - \rho\vec{v}\cdot\nabla\Phi = \mathcal{H} - \mathcal{C} \tag{1.9}$$

expressed in terms of the density, $\rho$, velocity, $\vec{v}$, pressure, $P$, and specific energy $\epsilon$ without accounting for cosmological expansion. Also, $\mathcal{H}$ and $\mathcal{C}$ are respectively the heating and cooling rates of the gas which encapsulates much of the physics of the dynamics. Here, the numerous heating and cooling physics from radiation and the chemical network must be coupled in to produce self-consistent solutions. Finally, the equations must be closed with an assumed equation of state which relates the

pressure of the gas to the density, such as $P = K\rho^{\gamma}$ where $\gamma = 5/3$.

In this model, we find that gravity amplifies density perturbations and forms dark matter halos, quasi-spherical concentrations of dark matter particles that are gravitationally bound. The potentials created by the halos eventually attracts gas, which is able to cool and collapse to form galaxies. However, the non-linearity of the dynamics of the gas and numerous feedback prescriptions will produce different characteristics in each of these galaxies, leaving us to decipher the relative importance of certain physics. In the next subsection, we will discuss some of the predictions made about the early universe using these models.

### 1.1.2 Formation of Metal-Free Stars

Following chronological order, the first objects to form in the universe were metal-free primordial stars, so called Population III stars. Within the ΛCDM paradigm, we expect structure formation to proceed in a bottom-up fashion. That is, the first objects to form should be the smallest which assemble together to form the largest structures at later times. Thus, the first objects to form must have formed in small dark matter halos with M $< 10^8$ $M_{\odot}$, or mini-halos at a redshift of z = 20-30 [12, 13]. As such, we have no observational confirmation of the existence of these objects. At this early period in the history of the universe, there were no mechanisms in place to produce elements heavier than lithium, leaving only the primordial elements, hydrogen and helium, as fuel for structure formation. Moreover, these mini-halos had virial temperatures, T $\sim$ 1000 K, below the $10^4$ K threshold at which atomic hydrogen lines serve as efficient coolant [14]. The combination of the two resulted in highlighting the importance of the role of molecular hydrogen in these early structures [15, 16]. Thus, the non-equilibrium chemistry of the primordial elements and molecular hydrogen were explored, finding a number of different pathways for the formation of molecular hydrogen, the most important of which is $H + e^- \rightarrow H^- + \gamma$ leading

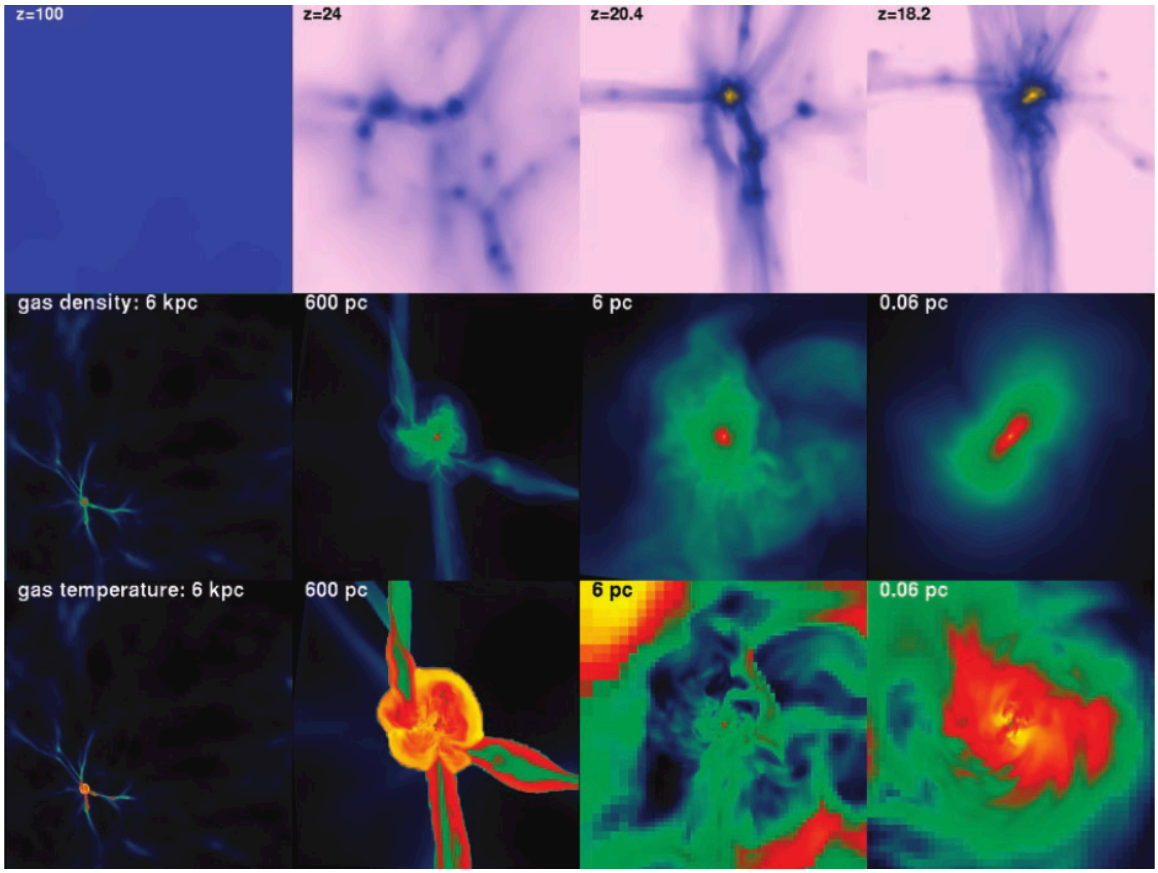


Figure 1.2: Projections and slices of the time evolution of the collapsing cloud in which the star forms. Top panels show projections centered at the formation site of the star. The middle and bottom panels show slices of the density and temperature at different resolutions. Taken from Abel *et al.* [21]

to $H^- + H \rightarrow H_2 + e^-$ [17, 18]. Once the gas clouds had collected beyond a critical molecular fraction of $f_{H_2} > 10^{-4}$, these clouds could then collapse to form the first stars [19, 20]. With fewer channels for fragmentation compared to the present day, early studies predicted the formation of stars with characteristic masses, $M \sim 100$ $M_\odot$ [21, 22]. Figure 1.2 shows the formation site of these stars taken from Abel *et al.* [21].

The formation of a star is not an instantaneous event, however. The gas cloud first collapses self-similarly prior to forming a hydrostatic core, which accretes gas [23]. Omukai and Nishi [24] calculated the former collapse phase using one-dimensional

simulations that took into account the radiative transfer of molecular hydrogen. They found that the collapse proceeds identically as in present-day star formation following the Larson-Penston similarity solution [25, 26]. At the end of the collapse, a small hydrostatic core with mass, M $\sim 10^{-3}$M$_{\odot}$, is formed. Initial studies also using one-dimensional calculations tracing the gas accretion phase showed that inefficient radiative feedback from the protostar enabled high accretion rates leading to large stellar masses in agreement with the previous formation calculations [27, 28]. However, three-dimensional calculations starting from cosmological initial conditions with protostar-scale resolution showed the fragmentation and then formation of two spatially separated cores, providing evidence of binary Pop III formation [29]. Although this simulation was not continued to the accretion phase, due to computational constraints, it demonstrated the possibility of fragmentation rather than single massive stars, which was the previously accepted scenario. Other studies then used sink particles to show evidence of fragmentation during the gas accretion phase further cementing the ubiquitousness of fragmentation [30, 31].

Once the star is formed, it immediately lights up producing radiative feedback to the surrounding interstellar medium. There are multiple dimensions to this feedback which will be briefly highlighted here. The first is the production of soft UV photons in the Lyman-Werner (LW) band. Because molecular hydrogen is fragile, the emission of the LW photons from these stars can easily photodissociate nearby molecular clouds [32]. As Pop III stars continue to form, they will then begin to build up a background of these LW photons that will then negatively affect the formation of future Pop III stars. In fact, the mass at which the primordial gas clouds collapse becomes sensitive to the strength of this background at all redshifts [33, 20]. On the other hand, once a gas cloud builds up a significant $H_2$ column density, it can also be self-shielded against this background as well [34, 35].

Higher energy radiation from Pop III stars can also photoheat the surrounding

medium. This feedback very efficiently photoevaporates the gas shutting off further star formation [36]. The ionizing photons also begin to form an extended H II region which spans 1-3 kpc [37, 38, 39, 40]. Thus begins the process of cosmic reionization, a topic that will be discussed in the very next section. Also, the contribution of these primordial H II regions to the process of reionization is also the central topic of Chapter 4.

One looming uncertainty about the first stars is the lack of constraints on the Initial Mass Function (IMF). Although recent efforts have simulated over 1000 mini-halos to obtain a statistical constraint [41], there are still many unresolved details and computational difficulties that prevent pinpointing an exact functional form. Overall, we know that massive stars emit light at much greater amounts than smaller stars resulting in a relatively short lifespan. From stellar evolution models, we expect that Pop III stars will die in a Type II core collapse supernova for $11 \lesssim M_\star/\mathrm{M}_\odot \lesssim 40$ [42], or in a pair-instability supernova expelling greater total energy for $140 \lesssim M_\star/\mathrm{M}_\odot \lesssim 260$ [43]. The gas that is processed in these stars will then undergo stellar nucleosynthesis to produce heavy elements that are ultimately carried out to their surroundings via supernova feedback [44, 45, 46]. Some of the supernovae will leave more massive black hole remnants which could potentially be seeds that grow to become supermassive black holes observed presently in the centers of galaxies [47, 48].

### 1.1.3 Formation of the the First Galaxies

Following several cycles of star formation, these mini-halos that once hosted Pop III stars will merge together to form the first dwarf galaxies. We will take the operational definition that a virialized object that is above $\mathrm{T} = 10^4$ K, the threshold above which atomic cooling lines are efficient, is a first galaxy. These objects must have had corresponding masses of $\mathrm{M} \simeq 10^8$ $\mathrm{M}_\odot$. The progenitor mini-halos must have had a

number of Pop III star formation events which would then process the ISM enriching the surroundings with metals. Supernovae from these stars could enrich nearby mini-halos with metals which could then directly form metal-poor, or Population II, stars prior to the recovery of the host halo [49]. Otherwise, these halos will recover their gas and undergo subsequent star formation after about 10 million years [50]. In particular, this transition from Pop III stars to Pop II stars is also of interest. The first generation of metal-poor stars must have formed directly as a consequence of the enrichment process triggered by primordial supernovae. Therefore, the chemical abundance patterns of such stars must be direct tracers of primordial supernovae providing more insight in to the properties of Pop III stars. This particular path of probing the first stars is known as stellar archaeology [51] and recent observations of carbon-enhanced metal-poor stars (CEMPs) have ignited an interest in the hunt for signs of the first stars [52]. The first galaxies are expected be an ideal environment in which this transition occurs.

Although we currently do not have any direct observations of any of these objects, there are a few places where we can see hints of the first galaxies. The first is looking at similar sized objects in the Local Group. Some of the dwarf galaxies that are near by may be from the first generation of galaxies that were formed that were eventually merged in naturally as structure formation progressed. Of particular interest are the Ultrafaint Dwarf Galaxies (UFD) which are the the least intrinsically luminous galaxies in the Local Group with $L_{tot} \lesssim 10^5 L_\odot$ [53]. These objects are speculated to have a minimum number of star-formation events which can potentially lead to more readily extracting the details of the early chemical enrichment processes.

Another such class of objects are globular clusters. Nearly every observed galaxy of a sufficient stellar mass ($> 10^7 M_\odot$) contains a globular cluster system. The globular clusters (GCs) themselves have a color bimodality allowing for distinguishing between a blue, metal-poor (BGC) population and a red, metal-rich population [54].

In particular, BGCs are of significant interest because their relative age ($\geq$10 Gyr) [55] places them in the correct epoch to be related to the formation of the first galaxies. Thus, understanding the mechanisms through which globular clusters formed may be central to understanding how the first galaxies were assembled.

Furthermore, because they are the first galaxies, these objects are relatively simple compared to present day galaxies, like our Milky Way. Because they have fewer star formation events in their histories, they have relatively little contamination from the physics of dust and metals, which can add significant complications in the dynamics of the gas. Also, their small sizes enable them to be sufficiently resolved starting from cosmological initial conditions to insert the details of the currently established set of physics for the galaxy formation process. In the next section, we will introduce how these objects start the latest phase transition of the universe.

## 1.2 Epoch of Reionization

As the first stars light up and emit radiation ionizing their immediate surroundings, the dark ages come to an end to trigger the beginning of the Epoch of Reionization (EoR). The EoR begins with Pop III stars and is driven by starlight from subsequently formed galaxies and galaxy clusters ending once the entire universe is fully ionized. This process is not completely trivial as gas that is once ionized can then recombine returning to the neutral state. For example, Pop III stars can leave relic H II regions as the surrounding gas recombines resulting in partially ionized gas. Thus, to accurately capture the physics of this period, one must keep track of both the sources and sinks of ionizing radiation. In the following sections, we will briefly summarize the key physics involved during the period and the connection to observations.

### 1.2.1 Physics of Reionization

During the EoR, the central physics are that of ionization and recombination, which can be represented by the chemical equation

$$H + \gamma \leftrightarrow \mathrm{H}^+ + e^- \tag{1.10}$$

When the energy of the incoming photon, $\gamma$, is greater than 13.6 eV, then the neutral hydrogen will absorb this photon kicking out the electron. The opposite reaction, or recombination, occurs simply through Coulomb attraction as demonstrated in electrostatics. We can then quantify the rates at which these processes occur.

First, the ionization rate must be proportional to the rate at which ionizing photons are being produced. The rate is given by

$$\dot{\mathcal{N}}_I = \sigma_{\mathrm{HI}} n_{\mathrm{HI}} F \ \mathrm{cm}^{-3} \ \mathrm{s}^{-1} \tag{1.11}$$

where $\sigma_{\mathrm{HI}}$ is the photoionization cross-section, or the probability that a single photon will be absorbed, $n_{\mathrm{HI}}$ is the number density of neutral hydrogen in a given volume, and $F$ is the ionizing radiation flux.

On the other hand, since recombination occurs via Coulomb interaction, the rate must be simply proportional to the concentration of the two ion populations. Thus, the recombination rate is given by

$$\dot{\mathcal{N}}_R = n_{\mathrm{e}} n_{\mathrm{p}} \alpha_{\mathrm{n}}(T) \ \mathrm{cm}^{-3} \ \mathrm{s}^{-1} \tag{1.12}$$

where $n_{\mathrm{e}}$ and $n_{\mathrm{p}}$ are the electron and proton number densities respectively, and $\alpha_{\mathrm{n}}$ is the temperature-dependent recombination rate coefficient for a given electron level n. One can then sum this rate over all the electron levels of hydrogen to get a total recombination rate, which is known as 'case A'. However, as Equation 1.10 shows,

the recombination process emits out a photon as well. In the situation of the electron going directly to the ground state, or n =1, a photon exactly at the energy of hydrogen ionization is emitted, which will then propagate out to ionize another nearby hydrogen atom effectively producing net zero recombination. Thus, it is useful for us to consider the total recombination rate ignoring the n =1 scenario. The sum of these rates are then referred to as 'case B'.

In a region with ionizing sources, we can equate the two rates to then calculate an ionization fraction. However, in the case that stars are the sources of ionization, we also know that stars can only produce a finite amount of ionizing radiation before succumbing to their end. Thus, there must be an equilibrium state where the ionized volume no longer expands [56]. We can set the recombination rate equal to the ionizing photon luminosity to calculate the extent of this volume.

$$\frac{4}{3}\pi R^3 x_{\rm e} n_{\rm p} \alpha_{\rm B}(T) = \dot{\mathcal{N}}_\gamma \tag{1.13}$$

where $R$ is the radius of the ionized region, $\alpha_{\rm B}$ is the 'case B' recombination coefficient, and $\dot{\mathcal{N}}_\gamma$ is the ionizing photon luminosity. We can then solve for this radius, which is referred to as the Strömgren radius, given by

$$R_s = \left[\frac{3\dot{\mathcal{N}}_\gamma}{4\pi n_{\rm H}^2 \alpha_{\rm B}(T)}\right]^{1/3} \approx 3.44 \left(\frac{n_{\rm H}}{100\ {\rm cm}^{-3}}\right)^{-2/3} \left(\frac{\dot{\mathcal{N}}_\gamma}{10^{49}\ {\rm s}^{-1}}\right)^{1/3} \left(\frac{T}{10^4\ {\rm K}}\right)^{-0.282} {\rm pc} \tag{1.14}$$

where $x_e \equiv n_e/n_{\rm H}$, and we've taken the assumption that $n_e = n_p$ for pure hydrogen gas. Such regions are effectively the building blocks of reionization. Initially, Pop III stars will form disjoint isolated primordial H II regions which will merge and grow as more ionizing sources are produced in subsequent star formation events. These ionized bubbles will then begin to overlap one another as they begin to fill in significant volumes of the universe. Finally, the ionized regions fill the majority of the

volume of the universe as the small pockets of neutral plasma are eventually wiped away by the ionizing radiation.

Given this general outlook, an obvious question to pose may be what are the sources of ionization that are principally responsible for ionizing the universe. At first glance, quasars appear to be an attractive candidate in that they are brightest sources of radiation known in the universe. However, the number density of quasars are too low at high redshift to account for all of reionization [57]. Instead, starlight becomes the primary candidate for reionizing the entire universe. The quest then becomes understanding the details of the process of reionization as a whole. If starlight in galaxies are indeed the primary drivers during the EoR, then a better understanding of the EoR will necessarily provide deeper insight into the details of galaxy and structure formation in the universe. In the next section, we will discuss the current and upcoming observational constraints to aid us in this effort.

### 1.2.2 Current and Future Observational Constraints

The CMB not only provides constraints on the cosmological parameters but also constraints on the timing of the EoR. Here, the key value is the optical depth to Thomson scattering, $\tau$, which refers to the CMB photons that scatter off of free electrons floating about on the way to Earth. This scattering makes an imprint on the polarization of the CMB which can then be measured to provide an integrated value of the Thomson scattering optical depth. Figure 1.3 shows the measurements of $\tau$ starting from the WMAP mission to the latest results from the Planck satellite. Note the systematic decrease in the value of $\tau$ as we increase the precision in the measurements. As $\tau$ is an integrated value, the smaller the value, the later reionization must have started. The end of reionization is well constrained by quasar spectra as will be discussed shortly. Thus, a smaller $\tau$ also implies a shorter duration for the entire EoR. The latest constraints from the Planck satellite put the average reionization

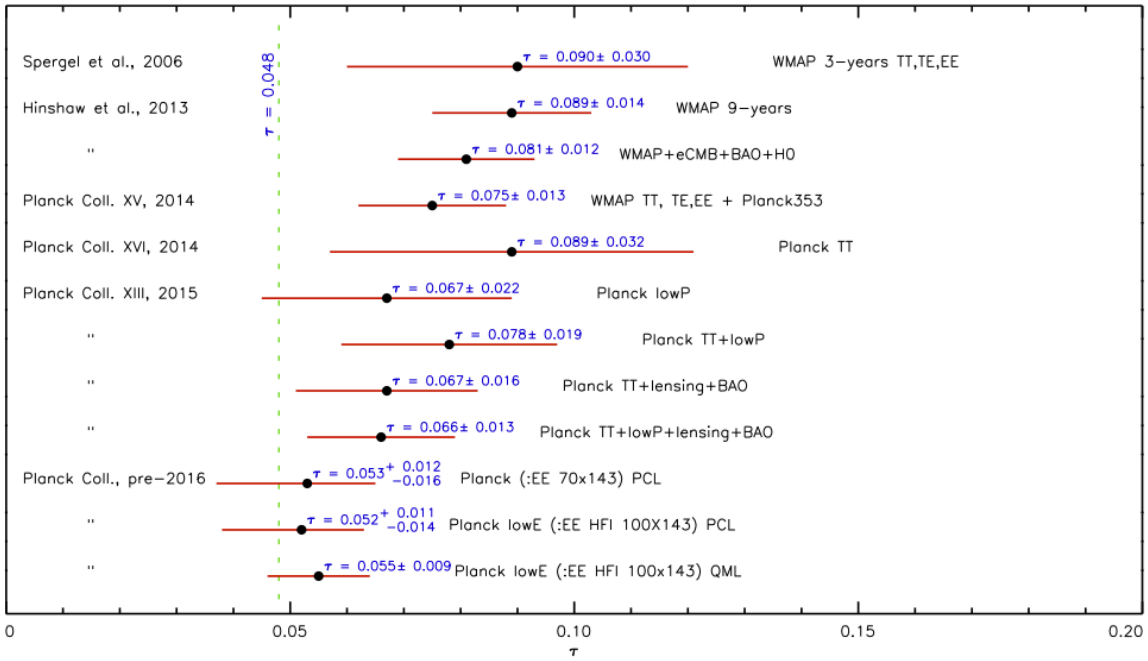


Figure 1.3: Measurements of the optical depth to Thomson scattering, $\tau$, starting with the WMAP 3-year results to the Planck Satellite 2016 Intermediate results. The value of $\tau$ has been significantly reduced since the initial measurement implying a much shorter duration for the Epoch of Reionization. Taken from Planck [59].

redshift, that is when the ionization fraction is half, at z = 7.8 to 8.8 [58].

The next key constraint for the EoR comes from the absorption spectra of quasi-stellar objects (QSOs), or quasars. Looking at these spectra shows a progression in which a trough following the peak flux is extinguished at z $\sim$ 6 [60]. This trough is known as the Gunn-Peterson trough, who identified the trough as an indication of the ionization state of the IGM surrounding the quasar [61]. In a highly ionized medium, the optical depth to Lyman-alpha (Ly$\alpha$) photons is high and all photons would thus be absorbed. Thus, these measurements constrain the EoR to have ended by z $\sim$ 6.

The most promising observations of the EoR, however, likely come from the hyperfine transition line in neutral hydrogen, also known as the 21-cm line [62]. These states arise when the intrinsic spins of the electron and proton in the neutral hydrogen are parallel or anti-parallel. Even with the advent of the James Webb Space Telescope (JWST), the likelihood of observing the very first luminous objects is quite

low [63]. However, the observations from upcoming radio telescopes should be able to detect 21-cm signals to arbitrarily high redshift down to the 'dark ages'. As we go back further in time, more of the IGM is neutral. The absorption and emission by neutral hydrogen is imprinted on to the 21-cm differential brightness temperature given by

$$T_b \simeq 26.9\left(\frac{1+z}{10}\right)^{1/2}\left(\frac{T_{\rm s}-T_{\rm CMB}}{T_{\rm s}}\right)\text{mK} \tag{1.15}$$

where $T_{\rm s}$ is the spin temperature indicating the relative occupancy of the electron spin levels, and $T_{\rm CMB} = 2.73(1+z)$ k is the CMB temperature. Measurement of the evolution of temperature would then directly probe the ionization history during the EoR. Upcoming large radio telescope arrays such as the Hydrogen Epoch of Reionization Array (HERA) [64] and the Square Kilometer Array (SKA) [65] should be able to map the EoR to precisions previously unattainable down to z $\sim$ 30.

### 1.3 Magnetic Fields in the Early Universe

With the progression of structure formation in the universe during the EoR, magnetic fields are also built up resulting a wide range of field strengths. Observations of the universe reveal the presence of magnetic fields at scales ranging from planets all the way to the voids between large cosmological structures [66, 67]. Moreover, measurements of galaxies show corresponding field strengths of up to tens of $\mu$G [68]. These observations imply a reciprocal relation between galaxy formation and magnetic field build up. How each process affects the other is a key question that is still under exploration. The physics of magnetic fields in plasmas is not trivially studied using analytic techniques, so it becomes a difficult problem to pull out immediate intuition regarding the dynamical impact they may have.

However, to give a heuristic argument for how magnetic fields can play a role, let

us first consider the scalar magnetic virial theorem, which is given by the following

$$\mathcal{W} + 2\mathcal{U} + \mathcal{M} = P_{ext} \oint x \cdot \hat{n}\, dA - \oint x \cdot \overleftrightarrow{T}\ \hat{n}\, dA \tag{1.16}$$

where $\overleftrightarrow{T}$ is the Maxwell Stress Tensor, $P_{ext}$ is the external pressure, the self-gravitational energy of the gas is given by

$$\mathcal{W} = -\frac{1}{2} G \int_V \int_V \frac{\rho(x)\rho(x')}{|x - x'|} d^3x' d^3x \tag{1.17}$$

where $\rho$ is the density, the thermal energy of the gas is given by

$$\mathcal{U} = \frac{3}{2} \int_V P d^3x \tag{1.18}$$

where $P$ is the gas pressure, and the magnetic energy contained in volume $V$ is given by

$$\mathcal{M} = \int_V \frac{|\vec{B}|^2}{8\pi} d^3x \tag{1.19}$$

which provides the equation of state for a system in virial equilibrium, such as a galaxy.

Applying Equation 1.16 to a isothermal gas cloud, we will define $4\pi R^3 \equiv \oint x \cdot \hat{n} dA$, and introduce some dimensionless terms $\alpha$ and $\beta$. Then we can rewrite the gravitational term and magnetic terms as

$$\mathcal{W} = -\alpha \frac{GM^2}{R} \tag{1.20}$$

$$\mathcal{M} + \oint x \cdot \overleftrightarrow{T}\ \hat{n}\, dA = \beta \frac{\Phi^2}{R} \tag{1.21}$$

Finally, plugging in Equations 1.20 and 1.21 to Equation 1.16, we can rearrange

the terms to read as the following,

$$P_{ext} = \frac{1}{4\pi}(-\alpha\frac{GM^2}{R^4} + \beta\frac{\Phi^2}{R^4} + 3\frac{a^2M}{R^3}) \tag{1.22}$$

where $a^2 = kT/m$ = constant and $M$ is the mass of the cloud.

We can see from this equation that the magnetic term has the effect of acting against gravitational collapse. Along with turbulence support, this term can potentially have the effect of sustaining gas clouds from collapse allowing for further growth.

### 1.3.1 Relevant Scales in MHD

Numerical studies of magnetic fields naturally involve the coupling of magnetic fields to the equations of hydrodynamics that govern the baryonic dynamics. Rather than deriving the full set of magnetohydrodynamic(MHD) equations, in this section we will highlight the key equations to understand the relevant scales in astrophysical contexts.

First is the induction equation,

$$\frac{\partial\vec{B}}{\partial t} + \nabla \times (\vec{B} \times \vec{v}) = -\nabla \times (\eta\nabla \times \vec{B}) \tag{1.23}$$

where $\vec{B}$ is the magnetic field, $\vec{v}$ is the fluid velocity, $\eta$ is the electrical resistivity. This equation effectively governs the evolution of the magnetic field strength in a fluid. If we take $\eta$ to be zero, we are left with the standard ideal MHD condition of flux freezing, in which the field lines can be thought of as being frozen into the plasma. This also results in a MHD scenario in which the field lines can never break. Using dimensional analysis on the three terms in Equation 1.23, we find

$$\frac{BV}{L} + \frac{BV}{L} \sim \eta\frac{B}{L^2} \tag{1.24}$$

which can then be reduced to

$$\frac{LV}{\eta} \sim 1 \tag{1.25}$$

Thus, we define the first relevant scale, the magnetic Reynolds number, given by $R_m = \frac{LV}{\eta}$, where $L$ and $V$ are the characteristic length and velocity scales respectively. This term can be understood as the relative importance of induction to diffusion of the magnetic field. Thus, if $R_m$ is less than 1, then diffusion must be significant in the system. In a typical molecular cloud, we can take $L \sim 10$ pc, $V \sim 3$ km s$^{-1}$, and $\eta \sim 10^{22}$cm$^2$ s$^{-1}$ [69] which gives us $R_m \sim 1000$. Thus, on these scales, magnetic diffusion is not significant.

Next, we introduce the momentum equation including the magnetic term

$$\frac{\partial}{\partial t}(\rho\vec{v}) = -\nabla \cdot (\rho\vec{v}\vec{v}) - \nabla P + \rho v \nabla^2 \vec{v} + \frac{1}{4\pi}(\nabla \times \vec{B}) \times \vec{B} \tag{1.26}$$

where $\rho$ is the density, and $P$ is the pressure. We can once again perform a dimensional analysis reduction to look at the terms which results in

$$1 \sim 1 + \frac{c_s^2}{V^2} + \frac{v}{VL} + \frac{B^2}{\rho V^2} \tag{1.27}$$

where $c_s$ is the speed of sound. Thus, we can now define the Alfvén Mach number, $M_A = \mathrm{V}/v_A$, in terms of the Alfvén speed, $v_A = \mathrm{B}\ /\ \sqrt{4\pi\rho}$. When $M_A \ll 1$, then the magnetic term dominates the dynamics, while for $M_A \gg 1$, the magnetic term is negligible. Once again, for typical molecular clouds, we can take $n \sim 100$ cm$^{-3}$, $B \sim \mu$G, and $V \sim 3$km s$^{-1}$, then $v_A$ is also a few km s$^{-1}$. This means that magnetic fields can have some influence, highlighting their potential significant role in the dynamics.

The final relevant scale is known as plasma beta which is defined as

$$\beta = \frac{p}{p_{mag}} = \frac{nk_BT}{B^2/(2\mu_0)} \tag{1.28}$$

which is the ratio of the gas pressure to magnetic pressure. Thus, it directly relates the relative importance of the magnetic field in the dynamics of a fluid. The smaller the $\beta$ value, the greater the magnetic field contribution.

### 1.3.2 Primordial Magnetic Fields

In this section, we will begin by considering the initial conditions of the problem at hand. In fact, a particular difficulty in understanding magnetic fields in the early universe is that the exact sources of the initial primordial magnetic field is unknown. This is further compounded with the uncertainty in the magnitudes of the initial field strengths. The particular sources have been speculated to be a number of different mechanisms which can be broadly separated into two categories: astrophysical processes after the start of structure formation and physics prior to recombination [70].

We will first consider the latter category which primarily refers to early universe phase transitions. In the early universe, there are periods as the plasma cools where matter changes phases from quark-gluon to mesons and baryons (i.e. hadronic phase) and where the electroweak symmetry breaks into the electromagnetic and the weak [71]. These periods are referred to as phase transitions, quantum-chromodynamic (QCD) and electroweak (EW) transitions respectively. Now the exact order of these transitions is not well constrained. If they are second-order, it will proceed smoothly in an adiabatic manner. However, if the order is first-order, then there are bubbles of the next phase that formed that can shock the surrounding medium. These mechanisms were explored by Hogan [72], Quashnock *et al.* [73] and Sigl *et al.* [74], who found that fields on the order B $\sim 10^{-29}$ G and B $\sim 10^{-20}$ G can be generated during

the QCD and EW transitions respectively.

A more exotic production scenario occurs during cosmic inflation. During inflation, the inflaton scalar field can be coupled to the electromagnetic field to produce fields as large as B $\sim 10^{-9}$ G [75]. Kandus *et al.* [76] found that charged scalar fields during inflation can produce currents which then lead to the formation of magnetic fields. The greatest drawback to these scenarios, unfortunately, is that there are virtually no constraints on the variety of physical mechanisms that can be evoked to produce these fields.

Thus, we come back to astrophysical processes. The most popular mechanism of primordial magnetic field is likely the Biermann battery. This mechanism is concisely represented by adding a term to the ideal MHD induction equation, originally introduced as Equation 1.23 [77]

$$\frac{\partial \vec{B}}{\partial t} + \nabla \times (\vec{B} \times \vec{v}) = \frac{cm}{e} \frac{1}{1+\chi} \frac{\nabla p \times \nabla \rho}{\rho^2} \tag{1.29}$$

where $c$ is the speed of light, $m$ is average mass per particle, $e$ is the charge of an electron, $p$ is the pressure, $\rho$ is the density, and $\chi$ is the ionization fraction. This term can be understood by looking at the cross product. When the density and pressure gradients are misaligned, the electrons drift faster than the protons and generating a net electric field in a closed loop circling the gradients [78]. Figure 1.4 shows a cartoon of the setup and the closed contour in which the net electric field is generated. This net field then produces an electromotive force which generates the magnetic field by Faraday's law. This effect was first explored in the cosmological context in numerical simulations by Xu *et al.* [79], who found peak magnetic field strengths of B $\simeq 10^{-9}$ G at the center of a star forming halo at z = 17.55, not yet strong enough to have any dynamical impact on the gas evolution. However, they could be sufficient to explain the galactic magnetic field assuming different amplification processes.

The final potential candidate for primordial magnetic field generation are the first

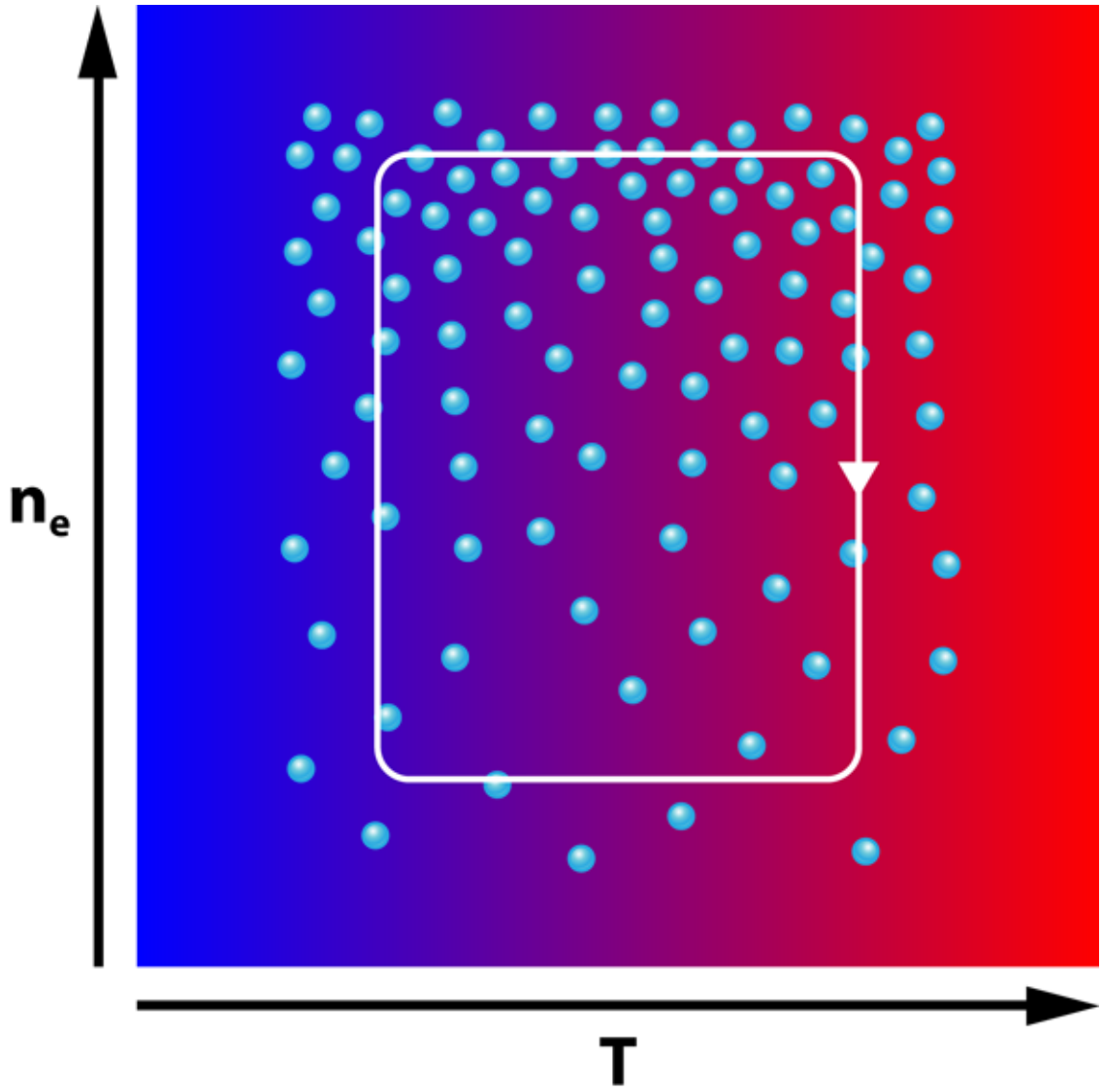


Figure 1.4: Schematic of the Biermann battery effect. The particles represent the electrons which are scattered about according to the density and temperature gradients. They form electric fields flowing through the highlighted loop which will lead to the production of an electromotive force and thus magnetic fields. From APS/Alan Stonebraker.

stars. Whichever way the fields are generated, stellar dynamos can efficiently amplify the seed fields which are then subsequently carried out to the surrounding medium via winds or supernova feedback. Bisnovatyi-Kogan *et al.* [80] and Pudritz and Silk [81] proposed models in which fields can be generated in protostellar gas clouds via a Biermann battery mechanism. This is a particularly attractive model because it has been shown that magnetic fields can play an important role in carrying out the angular momentum during the collapse phase of star formation enabling the protostellar core to be formed [82]. Furthermore, Machida and Doi [83] showed that the presence of magnetic fields during the accretion phase can result in different end scenarios for Pop III stars. Namely, when the magnetic field strength is $B > 10^{-12}\ (n/1\ \mathrm{cm}^{-3})^{2/3}$ G, the field can suppress fragmentation resulting in a single massive star. If the strength is increased further, it results in binaries, further emphasizing the potential importance of the magnetic fields.

Unfortunately, the observational constraints are limited in their ability to select out the sole or multiple origins of the primordial magnetic field. The latest results from the Planck Collaboration in measuring the effects of a stochastic primordial magnetic background on the CMB anisotropies by measuring the polarization of dust have resulted in a rather loose constraint of $B < 4.4$ nG [84]. This is further compounded by the fact that magnetic fields can be quite efficiently amplified through a number of mechanisms. These amplification mechanisms will be discussed next.

### 1.3.3 Growth of Magnetic Fields

Magnetic fields can be amplified in two primary methods: compression and dynamos. The former can be understood by considering a uniform ideal spherical collapse of a gas cloud where the magnetic field is frozen into the plasma. As the flux is conserved, the field strength must then scale with the cross-sectional area of the collapsing cloud. Alternatively, one can also visualize the field lines squeezing together as the total

volume is decreased. The scaling of the field strength is then given by the following

$$B \propto \frac{1}{A} \propto \frac{1}{r^2} \propto \rho^{2/3} \tag{1.30}$$

where $A$ is the cross-sectional area of a sphere, and $r$ is the radius of the sphere.

Dynamos, on the other hand, are a turbulent process that can lead to great amplification. Astrophysical dynamos can be further differentiated by the associated length scale. Large-scale dynamos can be on galactic scales where the turbulence driven by various stellar feedback and MHD instabilities can lead to twisting and tangling of the magnetic field lines [85]. This is most simply described by a mean-field theory which recasts Equation 1.23 as

$$\frac{\partial \vec{\mathbf{B}}}{\partial t} + \nabla \times (\vec{\mathbf{B}} \times \vec{\mathbf{V}}) = \nabla \times \vec{\mathcal{E}} \tag{1.31}$$

where $\vec{\mathbf{B}}$ and $\vec{\mathbf{V}}$ are the ensemble averaged values of the magnetic and velocity fields, and $\vec{\mathcal{E}}$ is the electromotive force generated by the turbulent terms [86].

The small-scale dynamos, however, operate at scales that are of the order or smaller than the energy carrying the turbulence. This was first explored by Kazantsev [87], who worked out the growth of the instability that leads to the amplification of the magnetic field. Since then, this mechanism has been studied in the context of the formation of the first stars providing a plausible scenario through which significant field strengths are generated from weak primordial fields [88, 89].

These mechanisms are key to understanding the build up of magnetic fields that traces hierarchical structure formation. In Chapter 3, we extend the exploration further by pushing beyond the formation of the first stars to understand the dynamical growth of magnetic fields until after the death of the first stars.

## 1.4 Computational Techniques

The investigations laid out in this work are primarily computational in nature and thus make use of cosmological simulation codes. In particular, the adaptive mesh refinement (AMR) software Enzo is used. Enzo is an open-source fully coupled radiation transport hydrodynamics code that is parallelized over MPI and OpenMP protocols used for a wide-range of physical and astrophysical applications varying in computational demand. Unlike the popular cosmological simulation code Gadget which is a Lagrangian code, Enzo is a Eulerian code. The two types differ in the method in which the equations of hydrodynamics are discretized. In the former, the fluid itself is discretized, represented as particles. For the latter, space itself is discretized onto a grid while the modeled fluid travels between grids in terms of the dynamical flux. The AMR scheme then allows for arbitrary precision in regions of physical interest based on an astute selection of 'refinement criteria' by further splitting up cells into even smaller cells. This splitting is done dynamically enabling the flow of gas to be traced to high precision as the simulation is evolved. It also includes a number of models for various physics that are relevant to cosmological structure formation, such as star formation and feedback. Specific details of the implementation of the code can be found in the method paper [90]. Furthermore, the details of the relevant physics models can be found in the individual chapters.

## 1.5 Thesis Overview

Within the current framework of galaxy formation in a ΛCDM universe, we are now at a place to begin probing the details of early structure formation. This thesis works to understand the details of the dynamics and of the first objects that were formed in the universe and how they led to the formation of the first galaxies. In particular, our focus is on mini-halos, the smallest dark matter structures in which the first stars

are thought to be born in.

In Chapter 2, we investigate the effect of metallicity on the collapse masses of gas clouds in the early universe. Such objects are potential sites for the formation of the first metal-poor stars and this exploration provides insight to the conditions required for this mode of star formation as well as the transition from Pop III to Pop II stars.

Then in Chapter 3 we investigate the amplification of magnetic fields in the first mini-halos. Previous explorations stopped prior to the formation of the star, but this work shows the first numerical calculation from cosmological initial conditions following through to the formation, main sequence, and death of a Pop III star.

Next, we use a semi-numerical simulation code to study the impact of these primordial objects on reionization in Chapter 4. The code is extended to include mini-halos as potential sources and we compare the resulting ionization histories with that of standard models.

Continuing from the previous chapter, we then, in Chapter 5, propose a new computational method to produce cosmological simulations in an efficient manner without the use of fully coupled radiative transfer while maintaining some level of accuracy.

Finally, in Chapter 6 we briefly summarize the key results stemming from this work and conclude with future work to be carried out.

# CHAPTER 2
# EFFECT OF METALLICITY ON THE COLLAPSE OF PREGALACTIC GAS CLOUDS

In this chapter, we begin by exploring a relatively simple premise. Star formation occurs in the potential wells that attract gas clouds and gravitationally collapse. The minimum mass of the gas cloud above which this process can occur is an important value that can dictate the abundance of stars that are formed. This value has been explored in previous works for metal-free gas clouds. However, the introduction of metals can greatly change collapse dynamics by providing alternative cooling mechanisms. We explore this effect in this chapter. This particular work has been submitted for publication in the Monthly Notices of the Royal Astronomical Society. This work was co-authored by John Wise who ran the actual simulations and provided the data.

## 2.1 Introduction

The complex gas dynamics within mini-halos at the start of the Epoch of Reionization has profound effects on subsequent structure formation. In the case of primordial metal-free gas clouds, the key cooling agent that drives the star formation process is molecular hydrogen $H_2$ which dominates for temperatures below $10^4$ K, the maximum virial temperature of a mini-halo. The conditions for gravitational collapse as a result of efficient $H_2$ cooling is a well studied problem. However, $H_2$ is also easily photodissociated by soft UV photons with energies below 13.6 eV, in the Lyman-Werner (LW) bands of $H_2$ [32]. In these mini-halos that are able to efficiently cool, the first metal-free stars (Population III) will then emit such photons and dissociate the surrounding $H_2$ providing a negative feedback effect [91, 92]. Furthermore, the LW emission from a cosmological stellar population will build up a radiation back-

ground (LW background) that will influence $H_2$ abundances, and thus the collapse dynamics of halos, at relatively large distances beyond the immediate vicinity of the sources [93]. Machacek *et al.* [33] (M01) and Yoshida *et al.* [20] initially explored the collapse dynamics of these mini-halos incorporating this LW background in cosmological simulations. The former also used a number of spatial- and time-independent LW background strengths to provide a relationship between the minimum collapse mass of mini-halos and the LW flux. This minimum collapse mass is an important quantity that can provide estimates for the primordial star formation rates in the early universe.

Moreover, in M01, the effects of self-shielding were neglected, opting for an optically-thin approximation. As significant $H_2$ column densities are built-up, gas in halo centers can self-shield against the LW background to suppress photodissociation. This effect was estimated by Draine and Bertoldi [34] who provided simple analytic approximations, who found that a $H_2$ column density $> 10^{14}$ cm$^{-2}$ was required to see significant effects. Then in Yoshida *et al.* [20] and Glover and Mac Low [94], this effect was better approximated by calculating the exact column densities in only the Cartesian directions, the so-called six-ray approximation. However, most recent work has shown that an accurate 3D treatment of the effects of self-shielding results in photodissociation rates that differ from previous estimates by as much as an order of magnitude [35]. Similarly, Hartwig *et al.* [95] showed significant differences in the value of the critical UV flux required for gas collapse by calculating the column densities in 3D simulations.

But not only do the Pop III stars emit these soft UV photons to dissociate $H_2$, a fraction will also die in supernovae, in either the core-collapse or the pair-instability flavors [43, 96]. The metals formed from these primordial supernovae eventually enrich their surroundings to set the stage for future generations of metal-poor star formation [45, 36]. Once enriched, there are a number of different channels through which the

next generation metal-poor stars can form. First, the metal-enriched gas clouds can merge into larger halos which will then collapse to form stars [97, 98]. Secondly, the original halo can recover and collapse again after some extended recovery period [50]. Or thirdly, the supernova can externally enrich nearby mini-halos that survive the blastwave [49]. In each of these scenarios, the metal-enriched gas cloud must then cool and collapse to begin forming stars. However, unlike in the primordial mini-halos where the abundance of $H_2$ singly determined the collapse dynamics, metals add a degree of complication. The additional atomic and molecular transitions increase the number of channels by which the gas clouds can cool [99, 100, 101]. Just as the formation of Pop III stars was explored through the thorough understanding of the collapse dynamics of mini-halos and chemistry of $H_2$, the formation of these first metal-poor stars can be better understood by studying the interplay of metal- and $H_2$-cooling in these metal-enriched mini-halos.

Our primary goal then is to extend the work done in M01 to understand the collapse dynamics of metal-enriched mini-halos. To this end, we will explore the effects of variances in both the strength of the LW background as well as the metallicity of the gas. Secondly we extend the M01 results to include $H_2$ self-shielding. In this paper, we present the results from a series of cosmological simulations exploring this parameter space. The following section describes the setup for our suite of simulations. Then in Section 2.3, we present the results for the minimum collapse mass from our simulations. Finally, in Section 2.4, we discuss some of the neglected physics and conclude.

## 2.2 Methods

### 2.2.1 Simulation Setup

Our simulations were all run using the ENZO simulation code v2.5 [90], an adaptive mesh refinement (AMR) code that uses an N-body adaptive particle-mesh solver to

follow dark matter dynamics. We utilize a nine-species (H I, H II, He I, He II, He III, $e^-$, $H_2$, $H_2^+$, $H^-$) non-equilibrium chemistry model [18] using the $H_2$ cooling rates from Glover and Abel [102]. In order to solve the equations of hydrodynamics, we use the piece-wise parabolic method (PPM) and the Harten-Lax-van-Leer with contact (HLLC) Riemann solver for accurate shock capturing.

Each simulation has a top grid resolution of $512^3$ cells, and we employ a total of 10 levels of refinement, refining cells when any of the following criteria are met: (i) relative baryon overdensity of 8, (ii) relative DM overdensity of 8, and (iii) local Jeans length [103]. For the first criteria, we employ super-Lagrangian refinement, where the cells are refined more aggressively, i.e. a lower density refinement threshold, at higher levels[1]. We also require the local Jeans length to be covered by at least 4 cells in each direction. The effective spatial resolution is 1.41 comoving parsecs at the finest refinement level with an effective dark matter mass resolution of 99.1 $M_\odot$.

We initialized the simulations at $z = 150$ with a 500 $h^{-1}$ comoving kpc box and run them down to $z = 10$. All the simulations employ the same realization of initial conditionss, generated with the MUSIC initial condition generator [104] using second-order Lagrangian perturbation theory and the Planck 2015 best fit cosmological parameters [105]: $\Omega_\mathrm{M} = 0.3089$, $\Omega_\Lambda = 0.6911$, $\Omega_b = 0.0486$, $h = 0.6774$, $\sigma_8 = 0.8159$, and $n_\mathrm{s} = 0.9667$ with the variables having their typical definitions.

The main parameter space explored in this work is that of the strength of the LW background and the metallicity. For the LW background, we employ a uniform constant background at all redshifts for five different values, $J_{21} = (0, 0.01, 0.1, 1, 10)$, where $J_{21}$ is the specific intensity in units of $10^{-21}$ erg $s^{-1}$ $cm^{-2}$ $Hz^{-1}$ $sr^{-1}$. Likewise, we apply a constant uniform metallicity at all redshifts for four different values, Z $= (0, 10^{-4}, 10^{-3}, 10^{-2})$ $Z_\odot$. Lastly, we approximate the effects of LW radiative self-shielding using the spherically averaged "Sobolev-like" length method in Wolcott-

[1]This feature is triggered with the ENZO parameter `MinimumMassForRefinementLevelExponent` = -0.25 [see 90, for more details].

Green *et al.* [35] which attenuates the LW background in regions of high density, allowing efficient $H_2$ cooling. In order to compare with M01, we also run simulations without self-shielding for each metal-free simulation. In total, we have a complete suite of a 24 simulations spanning the parameter space.

As our simulations also include metals, we add the effects of radiative cooling from fine-structure transitions in metals using the method in Smith *et al.* [106]. This method involves using the tabulated cooling data generated with CLOUDY which considers the following logarithmically spaced range of variables: (i) density: $10^{-6}$ to $10^{6}$ cm$^{-3}$, $\Delta = 0.25$ dex, (ii) temperature: 10 to $10^{8}$ K, $\Delta = 0.1$ dex, (iii) electron fraction: $10^{-6}$ to 1, $\Delta = 0.25$ dex, and (iv) metallicity: $10^{-6}$ to 1 $Z_{\odot}$, $\Delta = 1$ dex, where $\Delta$ is the spacing. We use the CMB radiation spectrum and ignore dust cooling as our simulations do not reach high enough densities, where it significantly contributes to the cooling rate above $\sim 10^{12}$ cm$^{-3}$.

### 2.2.2 Treatment of Collapsed Peaks

Once a density peak reaches the maximal refinement level, we call the peak "collapsed". After a peak has collapsed, we insert an artificial pressure support to prevent the peak from collapsing further, which can cause numerical instabilities. This is the same method as used in M01 where an effective pressure term, the greater of the thermal pressure and $KG\rho_b^2\Delta x_f^2/\mu$, is used for each cell. $\rho_b$ is the baryon density in the cell, $\Delta x_f$ is the cell width at the finest refinement level, K is a dimensionless constant set to be 100, and $\mu = 1.22 m_{\rm H}$ is the mean mass per particle. We also set the cooling rate to be zero in cells that have reached a number density of $n \geq 10000$ cm$^{-3}$ to provide an additional check against excessive collapse. These methods result in unphysical behavior of the cores of the haloes, however, they enable us to maintain the collapsed state while evolving the simulation further in time as we are not interested in the dynamical properties of the individual peaks. Visual inspection shows excessive

fragmentation and disk formation but these effects are not physical and should not be taken as representative behavior of halos during this epoch.

## 2.3 Results

### 2.3.1 Halo Sample

Our analysis is focused on the final dataset at $z = 10$, as the dependence of the dense gas fraction on redshift is negligible because of the time-independent LW background and static metal enrichment. Moreover, as we are interested in the collapsed state of individual haloes, it is important to first construct a catalogue of haloes. For this purpose, we use the ROCKSTAR halo finder [107] to identify all the haloes that consists of at least 100 dark matter particles. From this list, we further limit our analysis to massive haloes that have more than 1000 dark matter particles and filter out any subhaloes that ROCKSTAR may have identified. This results in a catalogue of $\sim 2000$ halos for each simulation. In Figure 2.1, we show the representative cumulative halo number density from the run with zero metallicity and no LW background compared with analytic result. The analytic halo mass function was generated with the form

$$\frac{dn}{dM} = f(\sigma)\frac{\bar{\rho}_m}{M}\frac{d\ \ln\ \sigma^{-1}}{dM} \tag{2.1}$$

where $\bar{\rho}_m$ is the mean density, $\sigma$ is the root mean squared variance of the linear density field, and $f(\sigma)$ is the weighted distribution of first crossing of random walks. This functional form is taken from Tinker *et al.* [108] calculated using the python software package RABACUS [109]. As our DM mass resolution is around 100 $M_\odot$, we begin to see deviation from the analytic result below $10^5 M_\odot$. Likewise, we see deviation at the high mass end above $10^{6.5} M_\odot$ because of the lack of statistics for halos at this mass range in our relatively small box.

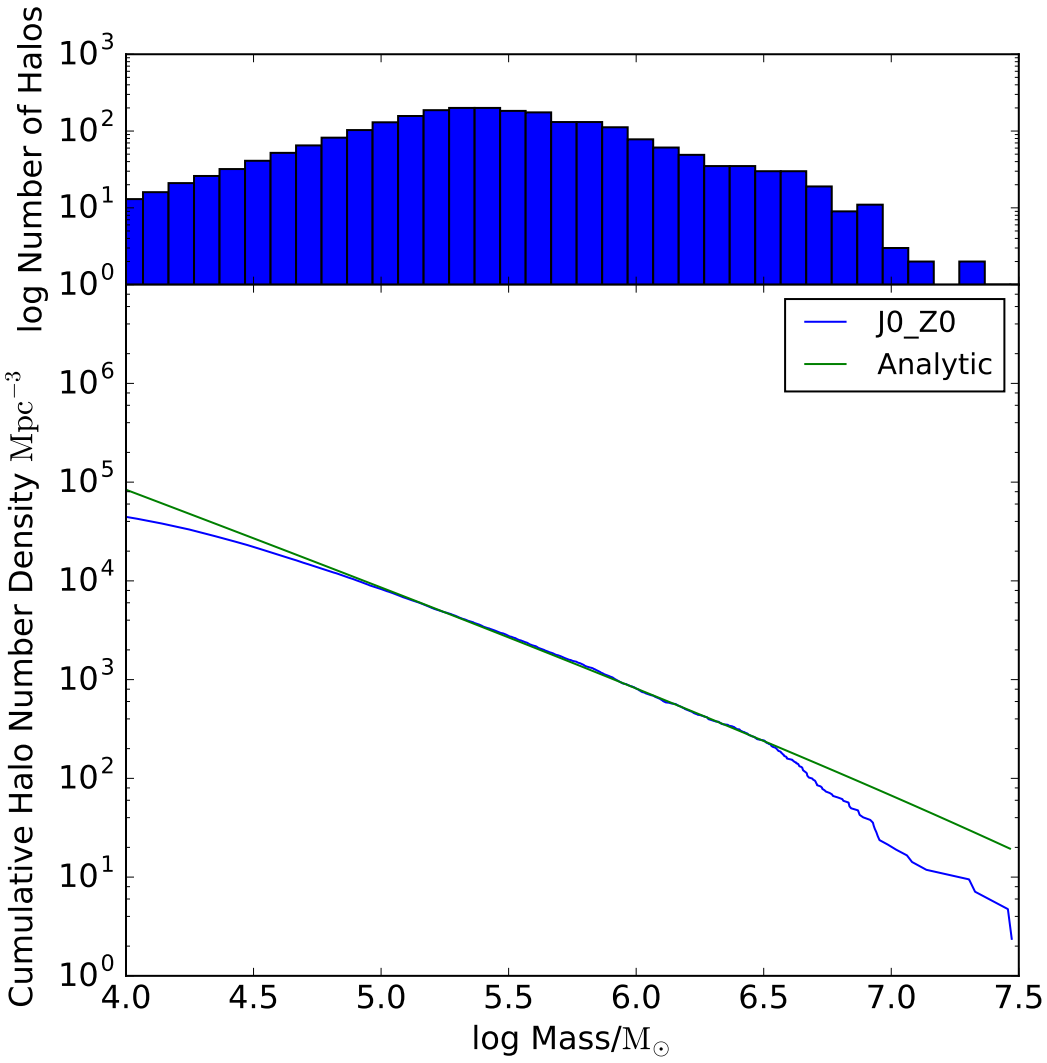


Figure 2.1: The cumulative number density of halos as a function of halo mass. The blue line shows the data taken from our fiducial run without a LW background or metals, which is meant to be representative sample as the distribution of halo masses does not significantly change between the various runs. The green line shows an analytic calculation for comparison. Above, we show the mass distribution of halos in the same run. At high mass ranges, there are very few halos.

### 2.3.2 Collapse Mass

We consider the collapse masses of the halos at a single snapshot at the end of each of the simulations at z = 10. For each halo, we check if any cell within a sphere of its virial radius has a number density greater than 330 $cm^{-3}$, the value assumed in M01. If so, we consider a halo collapsed as such a halo has met the condition for star formation. Once we check the collapsed state of each halo, we can sort the halos by their virial mass and identify the minimum mass of collapse for each simulation. This method is an approximation for the exact mass at which a halo may collapse. Because our analysis is done at a single snapshot, halos that we consider to be collapsed may have collapsed at an earlier time. This time delay, however, should only significantly affect the recorded collapse masses at the higher mass range for M $> 10^{6.5} M_{\odot}$ because we do not have enough halos to statistically obtain an accurate value for the minimum collapse mass. A more accurate method of calculating the exact collapse masses would involve generating merger trees for each of the halos we identify as collapsed at z = 10, and then tracing the most massive progenitors for each halo backwards in time to identify the initial point in which it collapsed. However, any further precision in the minimum collapse mass gained from this method would be far less than the statistical uncertainty at the higher mass range. Therefore, the minimum collapse mass reported at high mass ranges M $> 10^{6.5} M_{\odot}$ should be taken as an upper limit to the actual value.

*Effects of Self-Shielding*

Self-shielding was initially neglected in the analysis in M01 because initial estimates of the magnitude of the effect by Draine and Bertoldi [34] were significantly underestimated. Figure 2.2 shows the minimum collapse mass as a function of the LW background strength for both self-shielding-enabled and no-self-shielding cases. Direct comparisons with M01 show some differences, which we attribute to using the

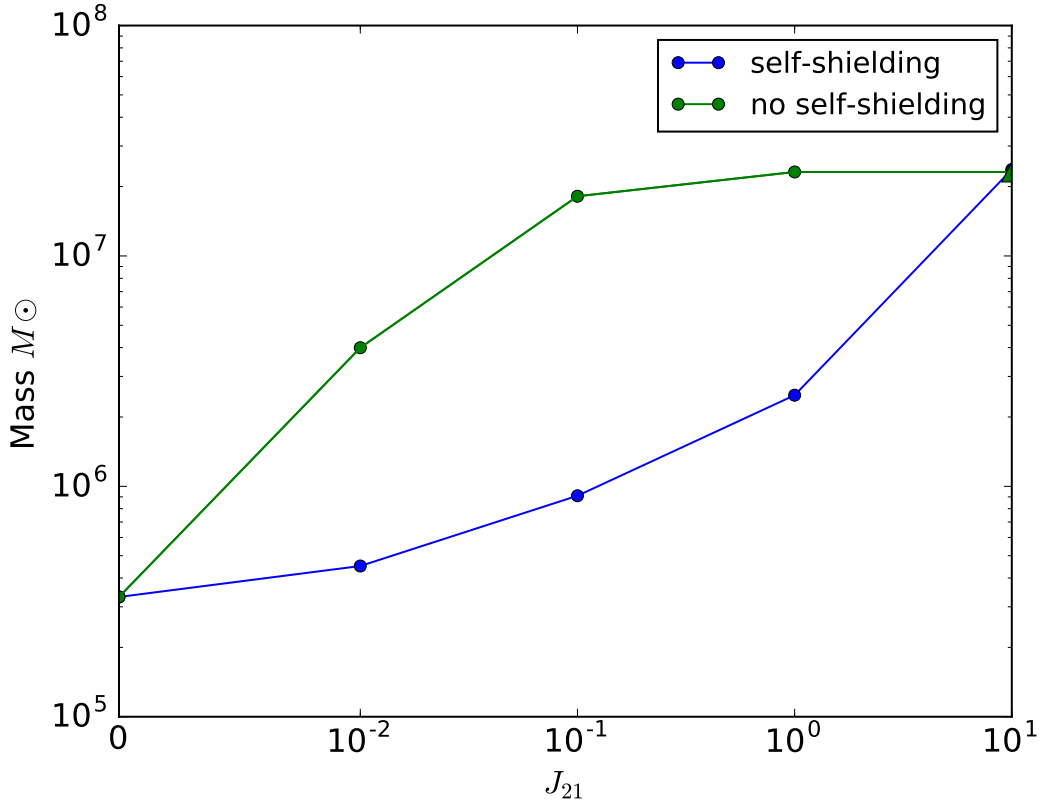


Figure 2.2: Plot of minimum collapse mass as a function of $J_{21}$. The blue line shows the base case which includes the effects of self-shielding, while the green line does not. For $J_{21} = 0$, there is no difference as there is no background flux for self-shielding to take effect against. In the case of $J_{21} = 10$ without self-shielding, there is a placeholder marker at the mass of the most massive halo as no halos have collapsed by the end of simulation at z = 10.

updated $H_2$ cooling rates from Glover and Abel [102]. In the no-shielding case, the LW background efficiently dissociates the $H_2$ and prevents cooling at even the highest mass haloes. This is in contrast with M01, who reported efficient cooling at even a weak LW flux of $F_{LW} = 10^{-22}$ erg $s^{-1}$ $cm^{-2}$ $Hz^{-1}$.

For the run with $J_{21} = 1$ without self-shielding, we find that only the most massive halo in the box has collapsed, whose total mass is 2.3 x $10^7$ $M_\odot$. However, as previously noted, in each of the runs, the halo likely collapsed at an earlier time and therefore with a lower mass. But because there is only one halo that collapsed at these LW background strengths, this collapse mass should be taken as an upper limit. In the case of $J_{21} = 10$, we find that none of the halos have collapsed by $z = 10$.

Once self-shielding is included, we see evidence of cooling at lower masses. The shielding prescription prevents the LW background from penetrating through the dense regions where $H_2$ can efficiently form unhindered. This results in cooling in our sample of haloes even at a relatively high LW background strength of $J_{21} = 1$. Once at $J_{21} = 10$, however, we see that self-shielding is not sufficient to prevent the dissociation of $H_2$ and once again only the most massive halo has collapsed.

At all LW background strengths, the differences in the minimum collapse mass are over an order of magnitude. The drastic differences in the minimum collapses masses for the two cases strongly suggest that self-shielding is an important effect and should always be included in any serious study of star formation at high-redshifts.

*With Respect to Photodissociating Background*

Next, we consider the effect solely due to the change in the strength of LW background for constant values of metallicities while including the effects of self-shielding. Figure 2.3 shows the minimum collapse mass as a function of $J_{21}$ for different metallicities. As expected, with no LW background, we observe efficient cooling even at masses down to $M = 2 \times 10^5$ $M_\odot$ consistent with M01 and Yoshida *et al.* [20]. Increased

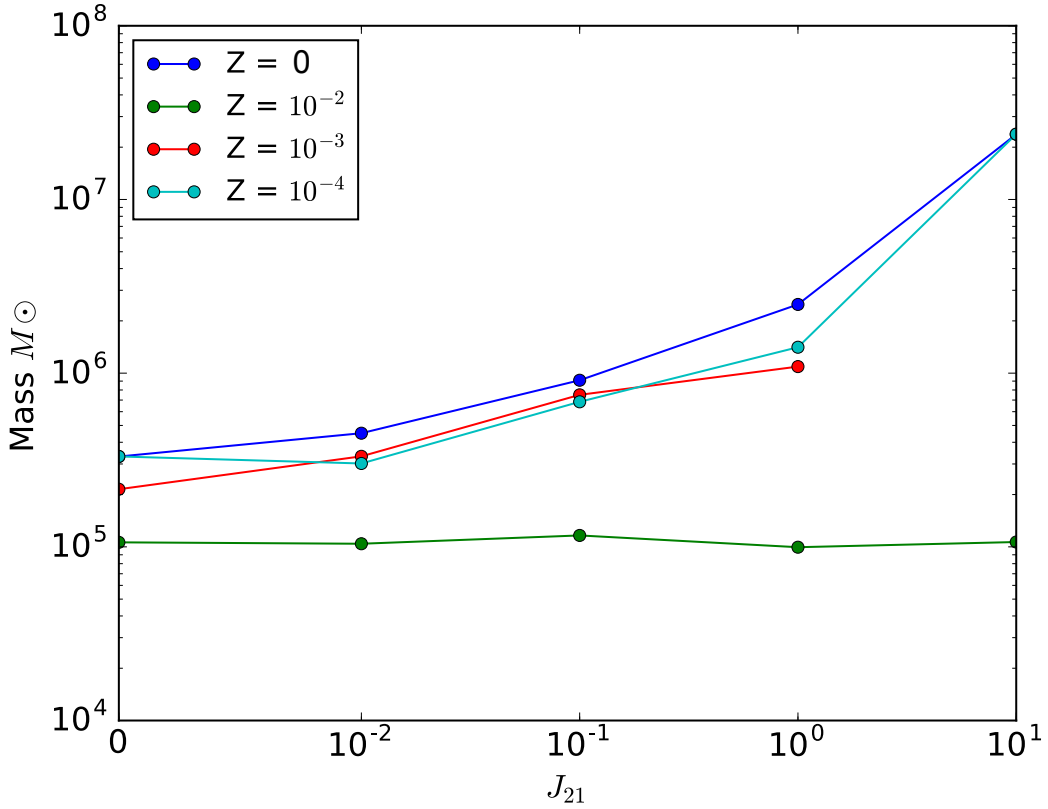


Figure 2.3: Plot of minimum collapse mass as a function of $J_{21}$ for different metallicities. There are minimal differences for any given LW background strength for metalliticities Z $\leq 10^{-3}$. However, for Z $= 10^{-2}$ $Z_\odot$, we see very efficient cooling independent of the LW background strength.

LW background strengths result in an increase in the minimum collapse mass as well. With increased flux, the photons can effectively dissociate $H_2$ to prevent collapse. This trend is also consistent with the results of M01. At the strongest LW background strengths with $J_{21} = 10$, only the most massive halo is able to collapse. In one particular case with Z $= 10^{-3}$ $Z_\odot$, we find none of the halos have collapsed by the end of the simulation at z $= 10$. The only deviation from this general trend can be found in the Z $= 10^{-2}$ $Z_\odot$ line where the minimum collapse mass does not change as a function of the LW background strength. This will be discussed in more detail in the following subsection.

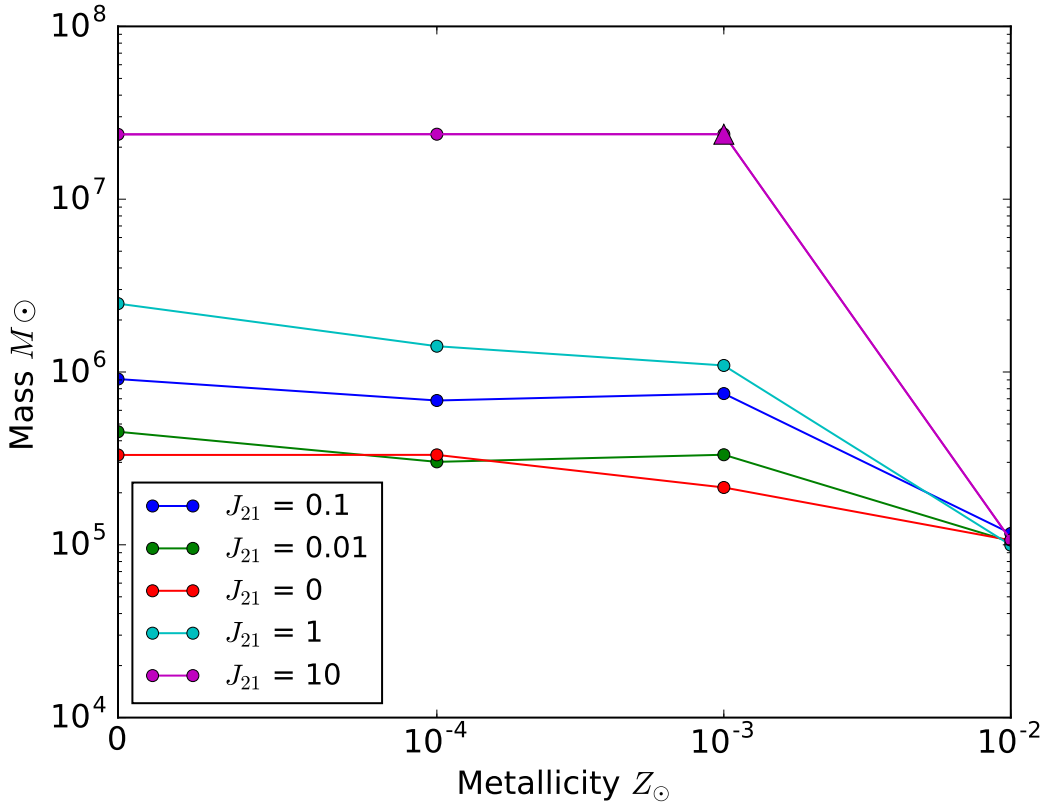


Figure 2.4: Plot minimum collapse mass as a function of metallicity. The triangle marker in the $J_{21} = 10$ is a placeholder marker to prevent displaying a misleading trend as no halo has collapsed in this particular run. All the lines show a largely flat trend, or perhaps small cooling effect from the metal cooling at the smallest metallicities. At Z = $10^{-2}$ $Z_\odot$, we find efficiently cooled halos around M = $10^5$ $M_\odot$ independent of the LW background strength.

*With Respect to Metallicity*

We now consider the effect of varying the metallicity for constant values of LW flux. Figure 2.4 shows the same minimum collapse mass data points from Figure 2.3 rearranged as a function of metallicity for constant LW background strengths. Qualitatively, we find a small downward trend from the metal-free case to the $Z = 10^{-3}$ $Z_\odot$ case, which is most clearly shown in the $J_{21} = 1$, indicating that metal cooling is prompting collapses in slightly smaller halos. In the other lines, the trend is largely flat, presumably due to the smaller sizes of the halos that do not have a high enough

virial temperature to invoke efficient metal cooling. For $J_{21} = 10$, there is only one halo collapsed in the metal-free and $Z = 10^{-4}$ $Z_\odot$ cases, which is the most massive halo. Although no halo has collapsed in the $Z = 10^{-3}$ $Z_\odot$ run, we inserted a placeholder datapoint to show a more accurate trendline. However, a pronounced difference can be seen for all simulations with $Z = 10^{-2}$ $Z_\odot$, where the minimum mass drops significantly down to $M = 10^5$ $M_\odot$, even further below the case with no LW background. This implies that between $Z = 10^{-2}$ $Z_\odot$ and $Z = 10^{-3}$ $Z_\odot$, there exists a critical metallicity, above which the metal-cooling becomes sufficiently efficient to be the dominant cooling mechanism over $H_2$ cooling, regardless of the LW background strength.

*Distribution of Collapsed Halos*

Figure 2.5 shows the fraction of collapsed halos to total halos as a function of halo mass. The starting point for each line indicates the minimum collapse masses shown in Figures 2.2, 2.3, 2.4, while any halo with the masses above the end point of each of the lines is collapsed. The distribution of collapsed halos is largely unchanged between different values of metallicity and LW flux. Based on the starting and end points, we can see that any halo that is an order of magnitude greater than the minimum collapse mass for a given metallicity and LW background pair is guaranteed to be collapsed.

## 2.4 Discussion and Conclusion

### 2.4.1 Neglected Processes

While we have explored a relatively large parameter space of the key variables in the cooling process, there are a few effects that we have not considered. As we have neglected any star formation or feedback, our simulations assume a fully neutral interstellar medium. Once ionized by a stellar source, the thermodynamics of the gas

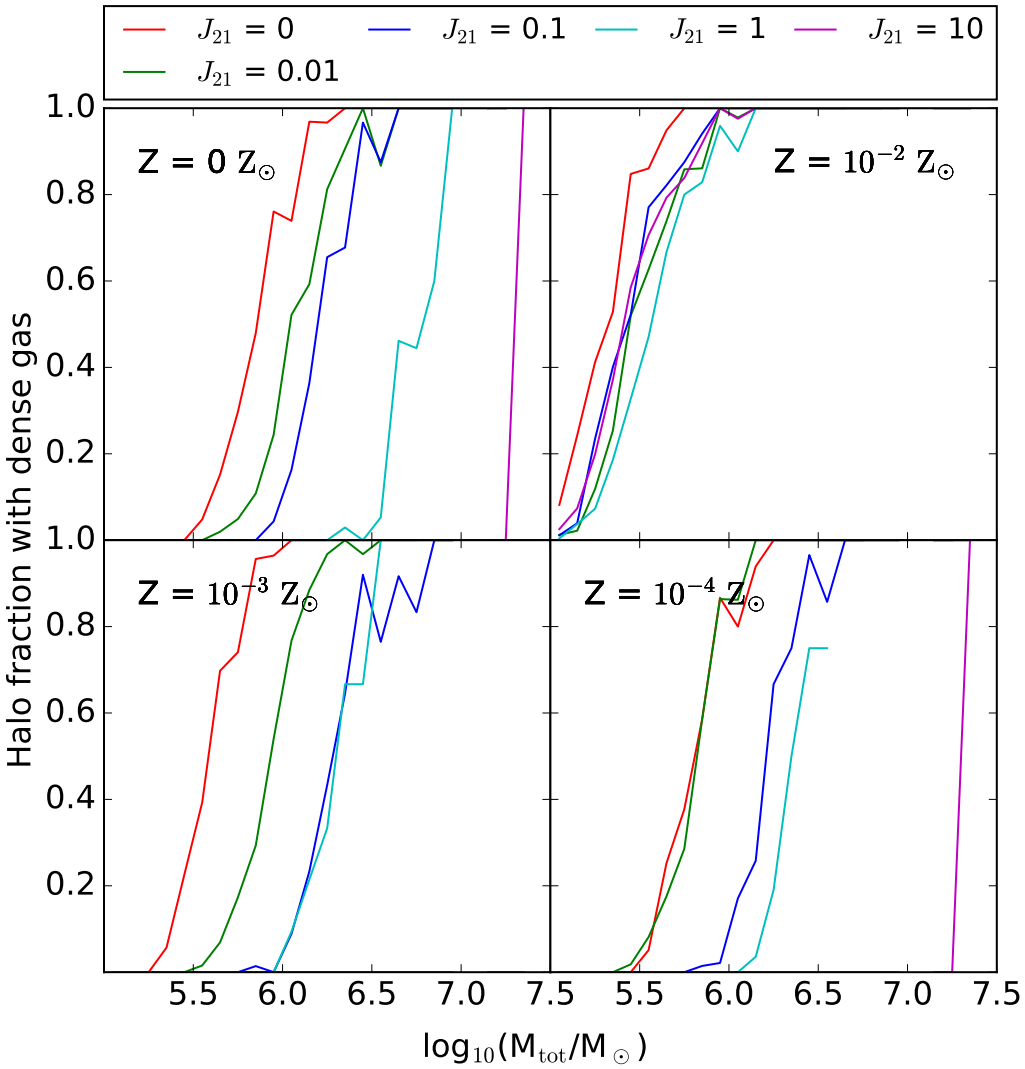


Figure 2.5: Fraction of collapsed halos to total number of halos as a function of halo mass.

should be altered. In particular, we showed the efficient cooling of halos with M $= 10^5$ $M_\odot$ can occur when the metallicity exceeds some critical value between Z $= 10^{-3}$ $Z_\odot$ and Z $= 10^{-2}$ $Z_\odot$. This exact scenario is unlikely to occur in a cosmological context, as any mini-halo must have been enriched through multiple star formation cycles to reach such high metallicities and thus the surrounding region must be ionized. However, there exist rare clumps which survive both the ionization front from stars and the subsequent supernovae that are strongly enriched. Our results can provide a basis to explain the collapse dynamics of such regions.

While previous results demonstrated marginal differences in star formation with the inclusion of relative streaming velocities of baryonic and non-baryonic matter [110, 111, 112], more recent results tell a different story. Ahn [113] relaxed the condition of limiting the large-scale density environment to be that of the global mean density to find significant differences in the resulting power spectrum. Such differences can result in major changes in the dynamics of mini-halos in the early universe, which has yet to be fully explored.

Moreover, the artificial pressure support that we introduced results in unphysical disk formation in many of the mini-halos. Consequently, the dynamics of mergers between these mini-halos may also be affected, such as the dynamical heating resulting from the mergers. However, given the large number of halos at the lower mass ranges, we expect these effects to only manifest in the mass distributions of the collapsed halos, if at all.

### 2.4.2 Conclusion

We present an extension of M01 by determining the minimum collapse mass of metal-enriched mini-halos for various LW background strengths and metallicities. We reiterate the importance of incorporating an approximate model of self-shielding [35] in studies that attempt to resolve the formation of Pop III stars as the minimum

mass for collapse can be affected by more than an order of magnitude. Our results also show that a critical metallicity exists between $Z = 10^{-3}\ Z_{\odot}$ and $Z = 10^{-2}\ Z_{\odot}$ where metal-cooling becomes the dominant cooling mechanism enabling mini-halos to collapse at a mass as low as $M = 10^5\ M_{\odot}$ independent of the strength of the LW flux.

# CHAPTER 3
# AMPLIFICATION OF MAGNETIC FIELDS IN A PRIMORDIAL H II REGION AND SUPERNOVA

Magnetic fields are often invoked in discussions of star formation as they can potentially play a significant role at multiple stages. Majority of these studies are done in idealized or isolated simulation work that does not fully capture the realistic environment of structure formation. Continuing on theme of understanding the dynamics of mini-halos, we explore the growth of magnetic fields in a single mini-halo starting from cosmological initial conditions through the formation of a primordial H II region as well the expansion of the remnant formed following a single supernova. This work has been published in the Monthly Notices of the Royal Astronomical Society [114]. This work was co-authored by John Wise who provided the initial idea and some of the analysis techniques.

## 3.1 Introduction

Magnetic fields are everywhere in the present day universe [see 85, for a review]. Various observations reveal the presence of magnetic fields at scales ranging from planets all the way to the voids between large cosmological structures [66, 67]. Moreover, measurements of galaxies show corresponding field strengths of up to 10s of $\mu$G [68].

Such fields may originate from the amplification of primordial fields in the early universe. These primordial fields may have been generated during the electroweak and QCD phase transitions [74]. Furthermore, Wagstaff *et al.* [115] demonstrated that sufficient turbulent conditions are realized in the radiation dominated universe prior to the onset of structure formation to produce field strengths on the order of $B_0^{\rm rms} \sim (10^{-6} - 10^{-3})$ nG on scales of 0.1 - 100 pc, sufficient to explain the magnetic

field strengths found in the intergalatic medium (IGM) [116]. Alternatively, Naoz and Narayan [117] found that primordial magnetic fields are expected to be generated through the Biermann battery mechanism [78] during linear structure formation through vorticity produced by scale-dependent temperature fluctuations.

On the other hand, the study of Population III star formation has been largely carried out without the addition of such magnetic fields. Earlier, these stars were thought to have been massive $M_\star \sim 100$ $M_\odot$ with suppressed fragmentation largely forming in isolation [21]. However, follow up studies with longer integration times at higher densities resulted in fragmentation, suggesting that Population III binaries are possible [29, 111, 118]. In particular, metal-free gravitational collapses in cosmological simulations have been followed until the formation of a protostellar shock [119], capturing the dynamics and fragmentation of the surrounding accretion disk [31]. In the very early stages of disk fragmentation, the majority of protostars have masses $M_\star < 1$ $M_\odot$ and some might be ejected from the central system [31, 120]. The final stellar masses are ultimately determined when the protostellar radiation quenches the accretion flow. Most recently, Hirano *et al.* [41] followed the formation and evolution of 1540 Pop III star-forming clouds, extracted from a cosmological simulation with a far-ultraviolet radiation background, with axisymmetric radiation hydrodynamic simulations. They found two distinct populations of metal-free stars, those formed in relative isolation versus those formed under the influence of $H_2$-dissociating external feedback. They found an initial mass function (IMF) with two peaks at $M_\star \simeq 250$ $M_\odot$ and 25 $M_\odot$ for the former population and a single peak at $M_\star \simeq 400$ $M_\odot$ for the latter population, demonstrating that metal-free star formation could indeed favor a top-heavy IMF.

As these stars begin to emit ionizing photons, they photoionize and photoheat their host halos and surrounding medium, creating a cosmological H II region. The particular radiative characteristics of Pop III stars were explored by Tumlinson and

Shull [121] and Schaerer [122] using evolutionary synthesis models. The latter results were then taken to study the resulting H II regions in one-dimensional hydrodynamics calculations [37, 38] showing that they span a typical radius of 1–3 kpc. Follow up three-dimensional studies with radiative transfer largely confirmed these results [39, 40]. At the end of its lifetime, the star dies in a Type II core collapse supernova for $11 \lesssim M_\star/\mathrm{M}_\odot \lesssim 40$ [42], or in a pair-instability supernova for $140 \lesssim M_\star/\mathrm{M}_\odot \lesssim 260$ [43]. These forms of stellar feedback were incorporated in numerical studies performed by Kitayama and Yoshida [44], Greif *et al.* [45], and Whalen *et al.* [46] tracing the near complete evacuation of baryons from the host halo. In particular, [45] characterized the behavior of the SN remnant in a numerical study following the four classical distinct sequential phases: free expansion, Sedov-Taylor, pressure-driven snowplow, and momentum-conserving snowplow [123]. Mixing of heavy elements expelled from the first stars can lead to fragmentation and low-mass metal-enriched star formation in neighboring minihalos and direct halo descendants, hosting the first galaxies [36, 124, 49].

Both analytic and numerical studies have demonstrated the amplification of a seed magnetic field by small scale dynamos during the collapse of primordial halos [125, 126]. In the absence of turbulence or other dynamo action, gravitational collapse can enhance the magnetic field strength as $B \propto \rho^{2/3}$ assuming the field is frozen to the fluid. Building upon this analytical work, Sur *et al.* [88] inserted a seed field of $B_{\mathrm{rms}} \sim 1$ nG into an isolated Bonnor-Ebert sphere, resulting in fields $\sim 10^{-3}$ G at a baryon density $n \sim 10^{14}$ cm$^{-3}$. Such fields may become dynamically important in subsequent star formation by potentially reducing fragmentation of molecular clouds [30]. Even without a seed field, Xu *et al.* [79] showed that significant fields can be formed through the Biermann battery effects. They found a peak magnetic field strength of 1 nG at a baryon density $n \sim 10^{10}$ cm$^{-3}$ at the center of the star forming halo at $z \simeq 18$. These fields, resulting from the Biermann term, are never strong

enough to become dynamically important, but rather set a lower bound on fields that would exist during Pop III star formation.

Furthermore, Federrath *et al.* [127] simulated the collapse of an isothermal Bonnor-Ebert sphere with a seed magnetic field and turbulent velocity fields showing that a minimum resolution of 32 elements per Jeans length is required to properly resolve dynamo action. As they increased the resolution up to 128 elements, they found significantly increased amplification rates with no signs of convergence. Turk *et al.* [128] then performed a full numerical calculation from cosmological initial conditions demonstrating similar results. They also found that a minimal resolution of 64 elements per Jeans length is required fully capture vortical motions that can enhance magnetic fields. These results imply the need for a much more stringent resolution requirement to fully explore Pop III star formation.

Thus far, these works have all mainly focused on the generation and evolution of magnetic fields during the primordial collapse, but they all stop short of the formation of the star. In this paper, we present calculations following the evolution of magnetic fields throughout the formation, main sequence, and aftermath of a Pop III star starting from cosmological initial conditions. We follow the magnetic amplification rates as the supernova remnant expands into the surrounding medium. In the following section, we describe the specifics of the numerical simulations. In Section 3.3, we present the amplification of the initial background magnetic field. We then discuss the missing physics that may potential influence our results in Section 3.4. Finally, we summarize our results in Section 3.5.

## 3.2 Methods

### 3.2.1 Simulation Setup

The simulations described subsequently have all been conducted with the ENZO simulation code v2.4 [90]. ENZO is an adaptive mesh refinement (AMR) code that uses an

N-body adaptive particle-mesh solver to follow dark matter dynamics. We utilize a nine-species (H I, H II, He I, He II, He III, $e^-$, $H_2$, $H_2^+$, $H^-$) non-equilibrium chemistry model [18] using the $H_2$ cooling rates from Glover and Abel [102]. To solve the ideal magneto-hydrodynamical (MHD) equations, we use the Godunov MUSCL (monotone upstream-centered schemes for conservation laws) algorithm with the Dedner hyperbolic cleaning method to enforce $\nabla \cdot B = 0$ [129, 130]. We also use the Harten-Lax-van-Leer (HLL) Riemann solver with piecewise linear reconstruction for accurate shock capturing.

We initialized the simulation at $z = 150$ with a $250h^{-1}$ comoving kpc box. The initial conditions were generated with the MUSIC initial condition generator [104] using second-order Lagrangian perturbation theory and the Planck 2013 best fit cosmological parameters [131]: $\Omega_{\rm M} = 0.3175$, $\Omega_\Lambda = 0.6825$, $\Omega_b = 0.049$, $h = 0.6711$, $\sigma_8 = 0.8344$, and $n_{\rm s} = 0.9624$ with the symbols having their typical definitions.

First, we ran a dark matter only simulation with a $256^3$ top grid with 8 levels of adaptive mesh refinement to $z = 12$. Next, we used the Rockstar halo finder [107] to identify the most massive halo with a virial mass $M_{\rm vir} = 2.3 \times 10^6 {\rm M}_\odot$ and radius $r_{\rm vir} = 316$ pc. We then calculate the initial Lagrangian volume centered on this halo that is a sphere with a radius of $4r_{\rm vir}$. The zoom-in initial conditions have two nested grids around this Lagrangian volume at $z = 150$. The effective dark matter mass resolution is 1.6 $\rm M_\odot$ in the high-resolution region, which is bounded by a cuboid with dimensions of $(72.3 \times 70.3 \times 76.2)$ comoving kpc$^3$ resolved by $(296 \times 288 \times 312)$ cells. We only allow the mesh to be refined in the exact Lagrangian volume of this sphere up to a maximum level of 15, corresponding to a maximal comoving spatial resolution of 0.04 pc.

The cells are flagged for refinement if one or more of the following criteria are met: (i) relative baryon overdensity of 3, (ii) relative DM overdensity of 3, and (iii) local Jeans length [103]. For the first criteria, we employ super-Lagrangian refinement,

where the cells are refined more aggressively, i.e. a lower density refinement threshold, at higher levels[1]. We also require the local Jeans length to be covered by at least 64 cells in each direction in order to fully resolve the vortical motions that can amplify the magnetic field as demonstrated by Federrath *et al.* [127] and Turk *et al.* [128].

Furthermore, a time-dependent Lyman-Warner optically thin radiation background modeled in Wise *et al.* [132] is utilized in the simulation, which is based on the semi-analytical model of Wise and Abel [133]. This model considers the LW contributions of both Pop III stars and galaxies and is valid at higher redshifts ($z \geq 12$) before metal-enriched stars dominate the cosmic emissivity. We use the functional form of the background evolution in Wise *et al.* [97],

$$\log_{10} J_{21}(z) = A + Bz + Cz^2 + Dz^3 + Ez^4, \tag{3.1}$$

where (A, B, C, D, E) = (-2.567, 0.4562, -0.02680, $5.882 \times 10^{-4}$, $-5.056 \times 10^{-6}$), and $J_{21}$ is the specific intensity in units of $10^{-21}$ erg s$^{-1}$ cm$^{-2}$ Hz$^{-1}$ sr$^{-1}$. Modulating this background, we include a prescription for radiative self-shielding taken from Wolcott-Green *et al.* [35] which reduces LW flux to supress $H_2$ cooling in haloes.

Each simulation was evolved until the most massive halo undergoes catastrophic cooling and collapse, and we momentarily stop the simulation at a refinement level of 15. We outputted data every 24.2 Myrs until this point. Once the halo collapsed, we then allow for star formation and feedback and wrote data every $10^5$ yr until the end of the simulation, 2 Myr after the supernova. By writing data at a relatively small time interval, we are able to trace the evolution of the regions around the star and ensuing supernova. The runs all end around $z = 14.4$. We ran the simulations on the Comet supercomputer at the San Diego Supercomputing Center using 12 nodes with 12 cores per node for each simulation. The runs took approximately 10 days each for

[1]This feature is triggered with the ENZO parameter `MinimumMassForRefinementLevelExponent` = –0.2 [see 90, for more details].

a total computational time of 100,000 core hours. All of the analysis were performed with the analysis and visualization toolkit YT [134].

### 3.2.2 Initial Magnetic Field

We conducted a total of three runs. Each run used the same initial conditions described previously. At the start of each simulation, we seed the box with a initial uniform background field of a given field strength purely in the $z$-direction. The seed fields are given in proper magnetic field strengths that are proportional to the square of the scale factor. The only difference between the runs is the initial seed magnetic field strength. Observations of high-energy photons from blazars put the lower limit of a background field at $10^{-15}$ G [135] while the upper limit on the field strength produced by primordial phase transitions is at $10^{-20}$ G [74]. Globally, the most recent constraint from CMB measurements puts the upper limit for the comoving field strength at scale of 1 Mpc at 4.4 nG [84]. Given the large uncertainty in the background field strength, we chose three different values. In the base case run, H2R, there is no seed magnetic field. In the runs H2R.B1 and H2R.B2, a proper seed field of $10^{-10}$ G and $10^{-14}$ G, respectively, was placed at the start. These correspond to comoving fields strengths of $4.4 \times 10^{-15}$ G and $4.4 \times 10^{-19}$ G.

### 3.2.3 Star Formation and Feedback

We only consider Pop III star formation in this work, and here we briefly describe the prescription for the formation and subsequent feedback mechanisms. We represent a single Pop III star using a single star particle [40, 97]. A particle is formed in a cell when the following criteria have been met.

1. An overdensity of $1 \times 10^6$ ($\sim 6000$ cm$^{-3}$ at $z = 15$).

2. A converging gas flow ($\nabla \cdot \mathbf{v}_{\rm gas} < 0$).

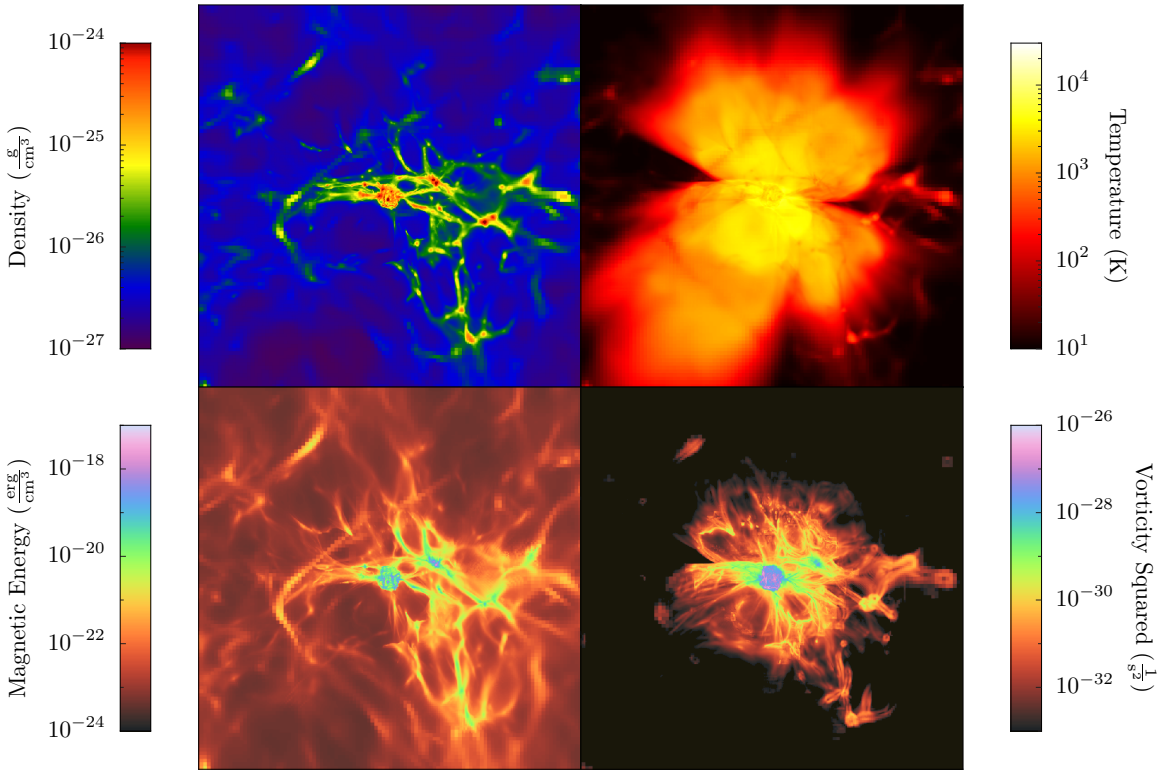


Figure 3.1: Mass-weighted projections of density, temperature, magnetic energy, and vorticity squared centered around the most massive halo at the end of the B1 run. Each projection has a width of 10 kpc. The H II region produced by the star is most prominently displayed in the temperature plot.

3. A molecular hydrogen fraction $f_{H_2} > 5 \times 10^{-4}$.

Given the uncertainty about the initial mass function of Pop III stars, we chose a fixed mass of 40 $M_\odot$ as the stellar mass. Then after the formation criteria are met, an equal mass of gas is then removed from the computation grid in a sphere containing twice the stellar mass and is centered on the particle. This particle is then initialized with the mass-weighted velocity of gas contained in the sphere. Moreover, we manually limited the simulation to prevent the formation of any subsequent stars after the first star was formed to minimize the computational stress of following multiple halos since our focus was only on the most massive halo.

After the formation, the star particle becomes a point source of $H_2$-dissociating, hydrogen- and helium-ionizing radiation. For the dissocating radiation, we approximate the radiation intensity as a $1/r^2$ field that is centered at the star particle, providing additional intensity on top of the background (Equation 3.1). The ionizing radiation field is evolved with adaptive ray tracing based on the HEALPix framework and is coupled self-consistently to the hydrodynamics [136]. As the rays propagate outwards from the source, they are adaptively split into child rays when the solid angle associated with the parent ray $\theta = 4\pi/(12 \times 4^L)$, where L is the HEALpix level, is larger than 20% the cell area. We use a discretized spectrum for the radiation with the following luminosities and photon energies: for $H_2$ dissociating radiation, $L_\gamma = 2.90 \times 10^{49}$ s$^{-1}$; for hydrogen ionizing photons, $L_\gamma = 2.47 \times 10^{49}$ s$^{-1}$ and $E_{\rm ph} = 28$ eV, which is appropriate for the near-constant $10^5$ K surface temperatures of Pop III stars; we also have helium singly and doubly ionizing radiation with lumonisities and photon energies of $L_\gamma = 1.32 \times 10^{49}$ s$^{-1}$, $E_{\rm ph} = 30$ eV and $L_\gamma = 8.80 \times 10^{46}$ s$^{-1}$, $E_{\rm ph} = 58$ eV, respectively [122]. At the end of its lifetime of 3.7 Myr, the star particle dies as a Type II supernova with a standard explosion energy of $10^{51}$ erg. The blast wave produced is modeled by injecting the thermal energy and ejecta mass into a sphere with a 5 pc radius. This injection is smoothed over the surface for numerical stability and is well resolved at initialization showing agreement with the Sedov-Taylor solution [36].

## 3.3 Results

We focus on the evolution of the magnetic field strength and morphology through the formation, main sequence, and supernova of a Pop III star, paying special attention to the amplification of primordial magnetic fields as the gas is processed by stellar radiation and the supernova. First, we visually inspect any morphological differences between the three simulations with varying initial magnetic field strengths. We then

quantify any field amplification that is caused by small dynamo actions beyond the expected compressional amplification.

### 3.3.1 Visual inspection

The most massive halo has a mass of $6.0 \times 10^5$ $M_\odot$ at the time of collapse at $z = 14.66$. A Pop III star forms near the center of the halo and begins to emit radiation heating up the entire region. Figure 3.1 shows projections of the entire H II region at the end of main sequence spanning a 10 kpc box. All three simulations have nearly identical characteristics at this time. The temperature projection clearly shows the extent of the region that is photoheated by the star. The H II region grows in a typical fashion, breaking out of the host halo within ∼300 kyr. The ionization front leaves behind dense neutral clumps that create shadows and form cometary structures similar to ones observed in the Galaxy (also see Figure 3.2). By the end of main sequence, the H II region has grown to 2 proper kpc, enveloped by a partially ionized and heated medium, resulting from the higher energy radiation that has a longer mean free path and can penetrate farther into the neutral IGM. The shielding from the nearby halos and filaments result in the butterfly shape of the region as seen in previous works [39, 40]. We also show the projections of magnetic energy where $u_{\rm B} = B^2/8\pi$ and the square of the fluid vorticity $\omega^2$ where $\omega = \nabla \times \mathbf{v}$. The growth of the magnetic field strength is directly related to the vortical fluid motion, and its evolution can be expressed as

$$\frac{\partial \mathbf{B}}{\partial t} + \nabla \times (\mathbf{B} \times \mathbf{v}) = 0, \tag{3.2}$$

in the ideal MHD case, i.e. when electrical resistivity is negligible. The vorticity evolution equation can be derived from the Navier-Stokes equation and can be written as

$$\frac{D\omega}{Dt} = -\omega \nabla \cdot \mathbf{v} - \frac{\nabla P \times \nabla \rho}{\rho^2} + \nu \nabla^2 \omega, \tag{3.3}$$

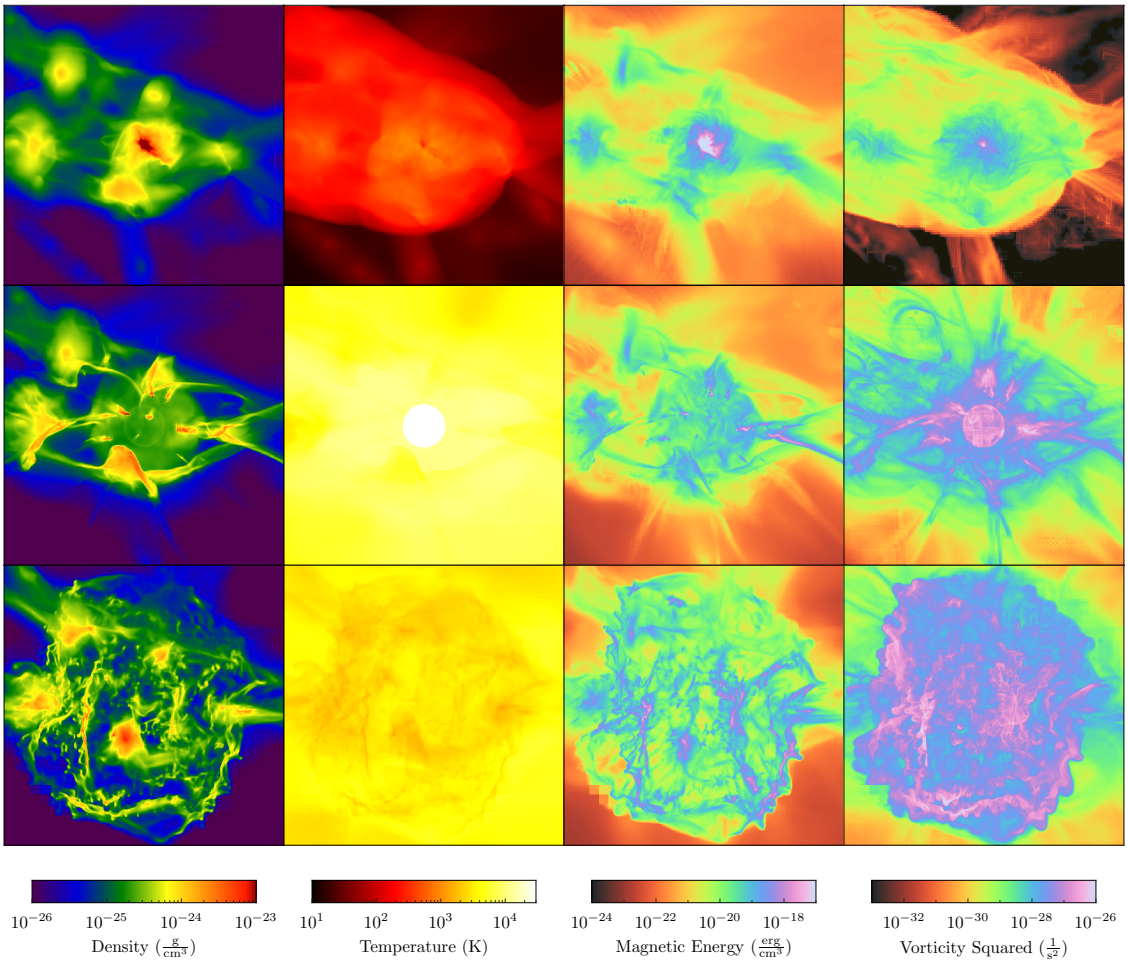


Figure 3.2: Density-weighted projections of density, temperature, magnetic field, and vorticity squared for the B1 run at three different times. Each projection has a field of view of 700 pc. The top panels show projections immediately following the birth of the star. The middle panels show the death of the star, and then 2 Myr after the supernova explosion at the bottom. Significant magnetic energy and vorticity is generated in the supernova remnant. The vorticity projection shows some grid artifacts as a result of the rendering which does not reflect the data.

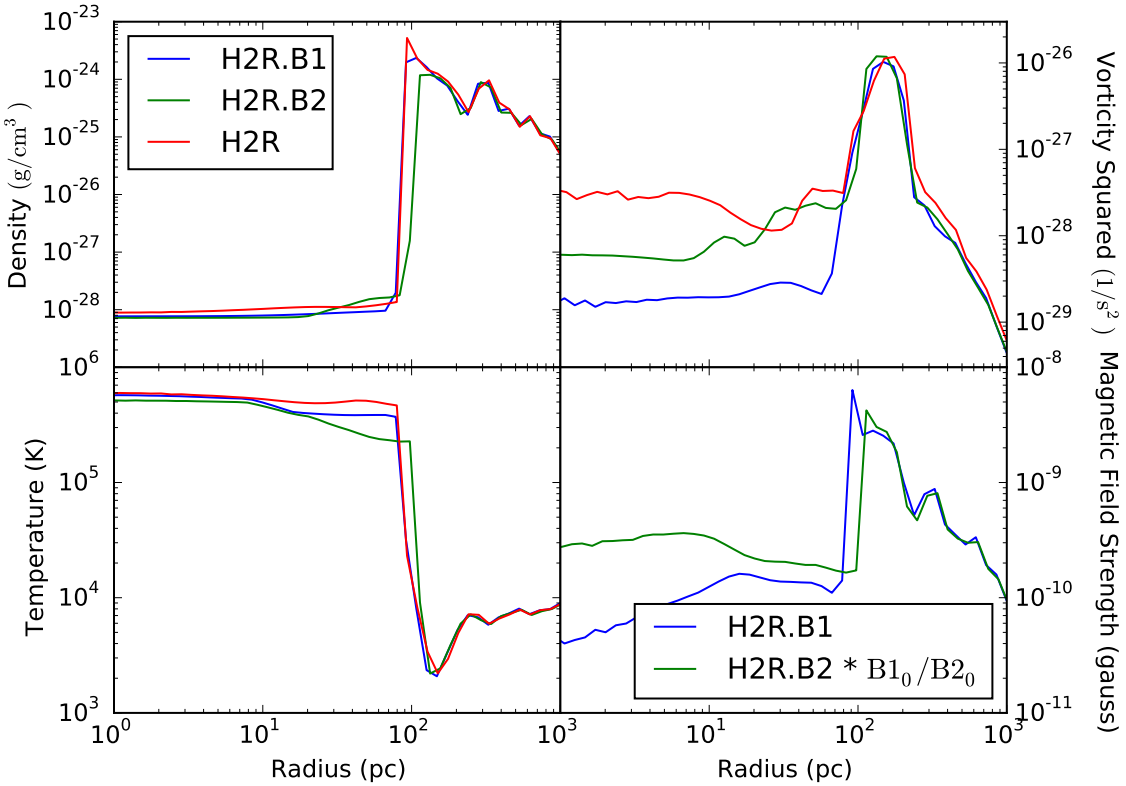


Figure 3.3: Radial profiles of density, temperature, magnetic field strength, and vorticity squared for all three runs at the end of the simulation 2 Myr after the supernova, centered about the star particle. In the magnetic field profiles, the field strengths in the H2R.B2 run have been scaled by $B1_0/B2_0$ where $B1_0, B2_0$ are the initial seed values of $10^{-10}$ G and $10^{-14}$ G respectively for better comparison.

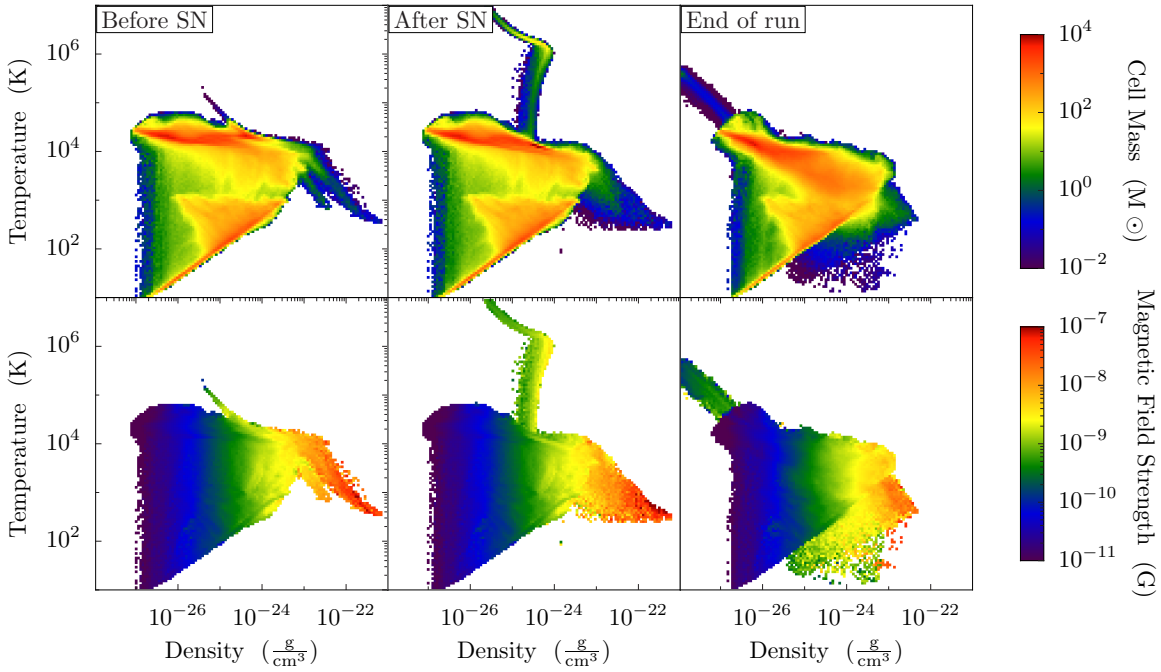


Figure 3.4: Phase plots of $\rho - T$ right before (left) and after (middle) the supernova, and at the end of the run (right). The top row shows the H2R.B1 run weighted by mass and the bottom row shows the same run weighted by magnetic field strength. The peak, representing the supernova, shows signs of amplification when compared with regions at the same density at lower temperatures.

where $\nu$ is the visocity, and we only consider non-viscous fluids ($\nu = 0$) in our simulations. Here $D/Dt$ is the fluid derivative, $P$ is the pressure, and $\rho$ is the density. The first term describes the stretching and compression of vortical motions, and the second term comes from non-barotropic flows, $P \neq P(\rho)$, which occur at or near shock fronts. In the lower panels of Figure 3.1, the presence of vortical structures as shown in the regions of high vorticity imply increased turbulent energy. Because magnetic field amplification is directly related to the vorticity and thus compression, regions of significant magnetic energy and vorticity are co-located with the regions of high density where gravitational collapse has compressed the field lines.

Figure 3.2 depicts the same projected quantities of the H2R.B1 run at the birth of the star, the death of the star, and 2 Myr after the supernova with a field of view of 700 pc. In the first row, we see the high density region near the center of the halo

where star is formed. This is also the point of peak vorticity in the entire run, arising from the compression of the gas (also see Figure 3.5). The emitted radiation then evacuates the surrounding gas greatly reducing the baryon density before the death of the star. The ionization fronts also photo-evaporate the gaseous envelopes of some of the nearby halos and filaments, compressing them and producing thin filaments in their shadows. The star lives for about 3.7 million years after which it dies in the form of a Type II supernova.

In the second row of Figure 3.2, there is a clearly delineated shell representing the supernova shock that propagates outwards. The shock mechanically compresses the gas producing regions of enhanced magnetic energy. By the end of the simulations, the supernova has completely disrupted the halo as shown in the bottom row panels. In its wake, the shock leaves behind little knots carrying metals which will eventually dissipate into the ISM. Although the host halo has been completely disrupted, there remains a smaller halo located below the main halo that manages to survive the irradiation and blastwave. This particular halo, now enriched by the metals carried out by the supernova, is likely to be a candidate for hosting second generation star formation. Smith *et al.* [49] found that the core of a comparable mini-halo following the supernova of a nearby Pop III star is enriched to $\sim 2 \times 10^{-5}$ $Z_{\odot}$.

### 3.3.2 Comparison of radially averaged quantities

In general, the morphology of the halos is not significantly affected by the presence of the magnetic field. To make a quantitative comparison, we calculate mass-weighted radial profiles, shown in Figure 3.3, within a sphere of 1 kpc radius centered on the Pop III star in all three runs at the end of the simulation, about 2 Myr after the supernova. The density and temperature profiles, in particular, show little deviation between the three runs. They also show the approximate location of the supernova shock which at this point is a radius of $\sim 150$ pc. At this point, the remnant is well

into the snowplow phase, in line with evolution of the SN remnant as shown in Greif *et al.* [45]. The shock has completely blown out the gas reducing the density within the shock radius to $\rho = 10^{-28}$ g cm$^{-3}$. Furthermore, the reverse shock heats the gas interior to the remnant initially to $\sim 10^8$ K and subsequently cools through $PdV$ work to $T = 5 \times 10^5$ K. As the shock front expands outwards, the dense shell is able to efficiently cool below $10^4$ K. The temperature and density gradients between shell and the hot interior drive turbulence resulting in magnetic field amplification.

However, notable differences can be seen in the vorticity profile where the difference between the H2R and the H2R.B1 run is more than an order of magnitude inside of the shock radius. For the H2R.B2, the vorticity squared sits between the two runs at $\omega^2 \simeq 6 \times 10^{-29}$ s$^{-2}$. This difference in vorticity is reflected in the magnetic field strength profiles. The magnetic field strength profile of H2R.B2 has been scaled up by a factor of $10^4$, corresponding to the ratio of initial field strengths, for better comparison with the H2R.B1 run. Recall that the initial seed field strength in the H2R.B1 run was $10^{-10}$ G, 4 orders of magnitude greater than that of H2R.B2. Within the shock radius, the H2R.B2 shows a greater average field strength reflecting the greater vorticity. At this time, the peak magnitudes, which are co-located with the shock radius, are $6.3 \times 10^{-9}$ G for H2R.B1 and $4.2 \times 10^{-13}$ G for H2R.B2. Furthermore, comparing the values shows that the magnitude of the amplification is independent of the initial field strength value because the magnetic field is still dynamically unimportant.

Figure 3.4 shows the $\rho - T$ diagram of the H2R.B1 run immediately before and after the supernova and 2 Myr after the supernova. The prominent peak in the second column represents the newly formed supernova remnant. As the magnetic field does not affect the dynamics, we do not see any significant differences in the three runs. The bottom row shows the same plot as the top row but shows the mass-weighted average magnetic field strength in each cell rather than the mass. In the bottom

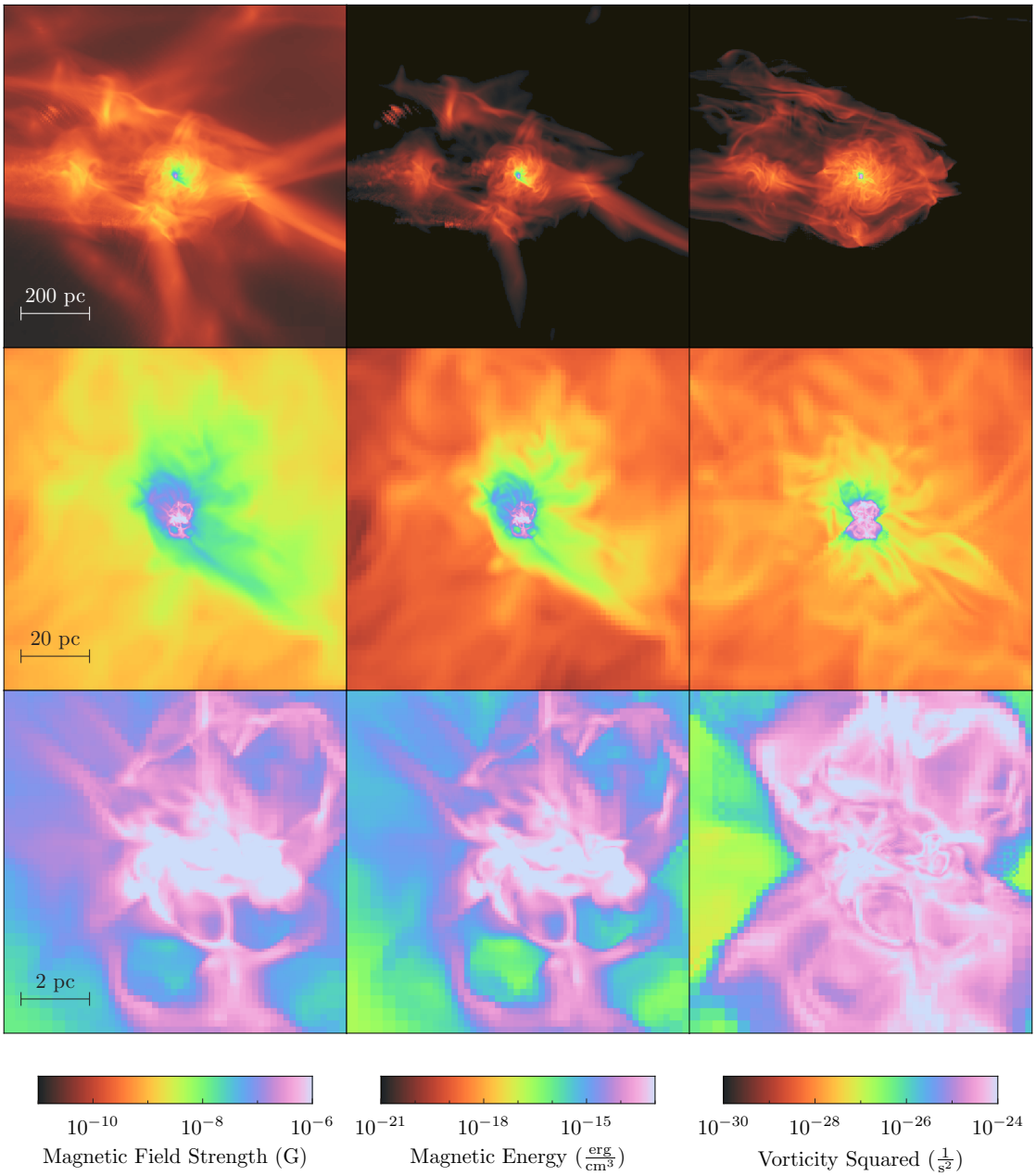


Figure 3.5: Projections of magnetic field strength, magnetic energy, and vorticity squared centered around the peak vorticity point of the B1 run shortly before the birth of the star. From top to bottom, the widths are 1kpc, 100 pc, and 10 pc. The magnetic fields are highly compressed at this time resulting in amplification.

middle plot, immediately following the supernova, there is evidence of amplification in the remnant when comparing the field strength at similar densities in the unaffected regions with $T \leq 10^4$ K. This peak evolves to lower temperatures as the remnant expands and dissipates into the surrounding medium. The bottom right plot shows the $\rho - T$ diagram at the end of the magnetized run. The magnetic field within the blastwave and the accompanying shell has been amplified, as seen by the enhanced field strengths below the adiabatic relation in $\rho - T$ phase space and in the hot and diffuse phase. This additional magnetic energy is not apparent in the bulk of the mass-weighted phase space because of the limited mass affected by the blastwave.

### 3.3.3 Amplification of Magnetic Field

*Maximum Magnetic Energies*

To characterize the significance of the magnetic field in this system, we calculated several key values at the point of peak vorticity. Figure 3.5 shows projections of magnetic field and vorticity centered around the point of peak vorticity from the entire simulation. This particular point was found to be at the point of collapse immediately preceding the insertion of the star particle. The peak density at this time is $3.8 \times 10^{-18}$ g cm$^{-3}$ with a magnetic field strength of $3.2 \times 10^{-5}$ G, consistent with the results from Turk *et al.* [29] and Latif *et al.* [137]. The first is the plasma $\beta \equiv (nkT)/(B^2/8\pi)$ which consistently remains $\beta \gg 1$ throughout the simulation. At the time of collapse, minimum, mean, and max values are 3.0, $4.1 \times 10^6$, and $1.7 \times 10^{11}$, respectively. This implies that the gas dynamics dominate the behavior while magnetic fields have minimal influence. Next, we calculated the Alfvénic mach number $M_{\rm A} \equiv V/v_{\rm A}$ where $V$ is the characteristic velocity and $v_{\rm A} = B/\sqrt{4\pi\rho}$ is the Alfvén speed within a sphere of radius $r = 300$ pc right after the formation of the star. $M_{\rm A}$ remained consistently $M_{\rm A} \gg 1$, typically having values $\sim$1000 outside the shock dropping to $\sim 50$ within a pc around the star. At the time of collapse, minimum,

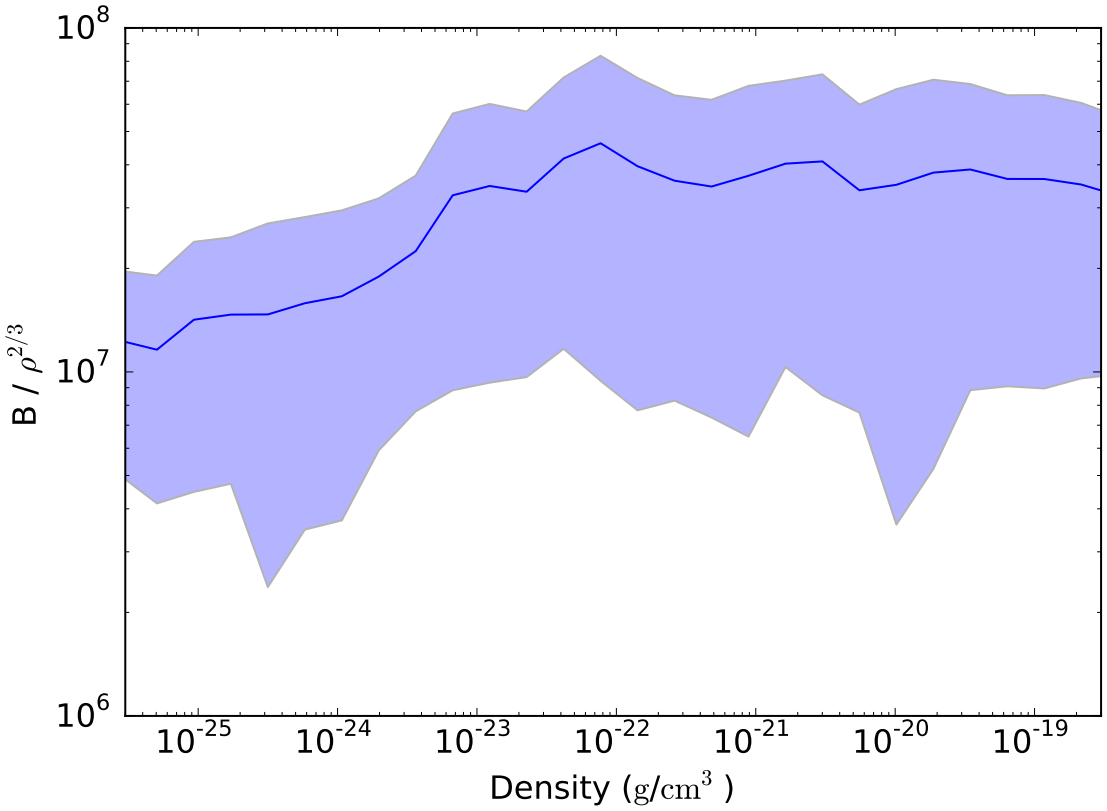


Figure 3.6: 1D mass-weighted profile of the magnetic field strength scaled by $\rho^{2/3}$ against the density at the time of collapse before the formation of the star. The blue line shows the mean where the shaded regions indicate the variance.

mean, and max values are 2.5, 1400, and $5.4 \times 10^5$. These values also indicate that the magnetic term is not dynamically important.

In Figure 3.6, we show the magnetic field strength scaled by $\rho^{2/3}$ as a function of density weighted by mass at the time of the halo's collapse. The blue line shows the mean with the shaded region indicating the variance. We see a small deviation from the expected flat relation indicating some dynamo action. Comparing the two relations shows that the field strength to density relation is steeper than 2/3 but not as high as 0.89 as reported by Turk *et al.* [29]. This is likely caused by the shorter integration time because we form the star at $1 \times 10^6$ cm$^{-3}$, far below $10^{13}$ cm$^{-3}$ from Turk *et al.* [29]. This is also consistent with the results from Sur *et al.* [88] which showed little deviation in the amplification from the $\rho^{2/3}$ relation at a density of $10^{-18}$ g cm$^{-3}$.

*Distribution*

In the case of a uniform spherical collapse for a magnetic field frozen into the gas, $B \propto \rho^{\alpha}$ where $\alpha = 2/3$. This relation approximates the amplification due to the compression of magnetic field lines as density increases. Thus, we define the amplification factor to be the ratio

$$\text{Amplification Factor} = \frac{u_{\rm B}\rho^{4/3}}{u_{\rm B_0}\rho_0^{4/3}} \tag{3.4}$$

where $u_{\rm B_0}$ is the initial seed field energy and $\rho_0 = \Omega_{\rm b}\rho_c(z = 150)$ is the cosmic mean baryon density. Any value of the amplification factor $> 1$ implies some amplification beyond the compressional scaling which can be attributed to turbulent dynamo effects.

The phase diagram in Figure 3.7 shows this amplification factor as a function of the density weighted by the mass within a sphere of radius 250 pc in run H2R.B1. The blastwave radius is approximately 100 pc at this time. Within this volume, nearly all regions have had its field amplified beyond the expected density scaling, implying

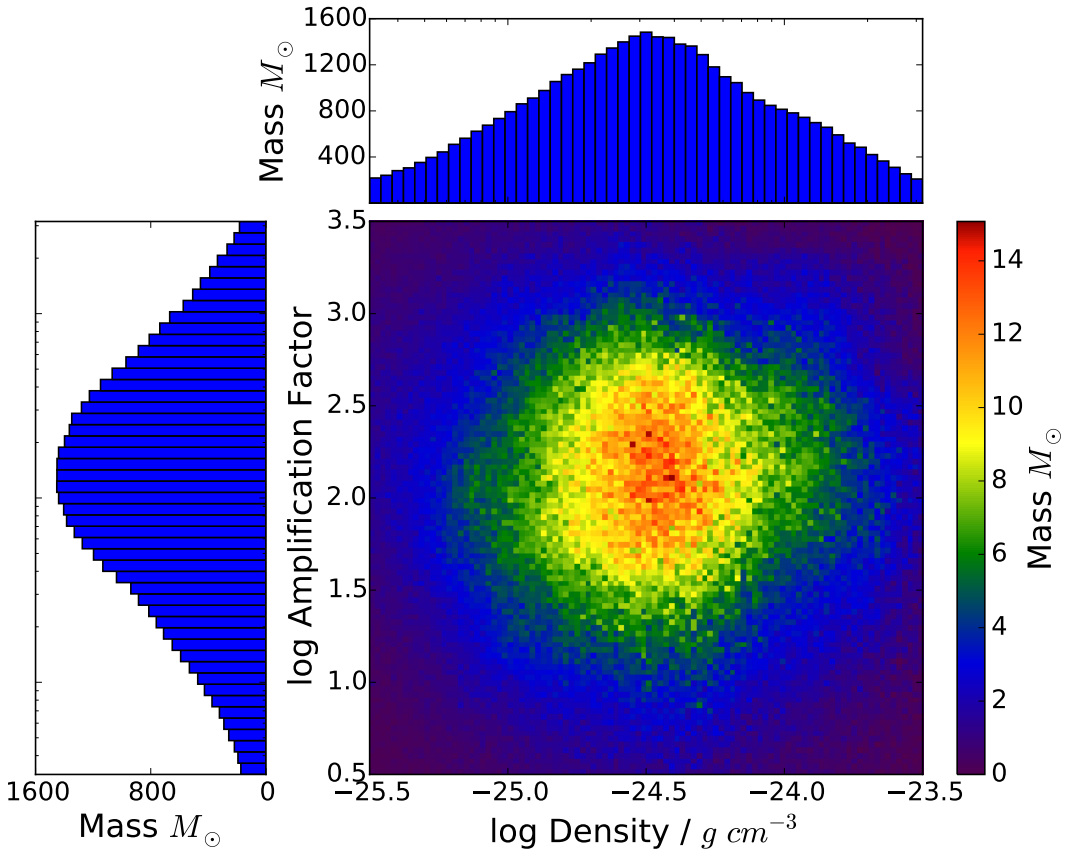


Figure 3.7: 2D mass-weighted histogram of the amplification factor and density at the end of the H2R.B1. Above each respective axes shows the projection to a 1D histogram. The amplification factor shows a clear Gaussian distribution with a mean around 120.

dynamo action is efficient during the blast wave propagation, especially during its momentum-conserving phase. To the left of the phase diagram is a histogram showing the distribution of the amplification factor weighted by mass. The amplification factor is log normally distributed with a weighted mean of $10^{2.08}$ and standard deviation of $10^{0.75}$. This is equivalent to a mean field strength amplification by a factor of $\sim$120.

Figure 3.8 shows a slice of the density and amplification factor at this time showing the distribution of the amplified magnetic field. The relative low densities in the central region evacuated by the supernova leads to high amplification factors. However, the highest magnetic field strengths are located in the shock front, where the gas has

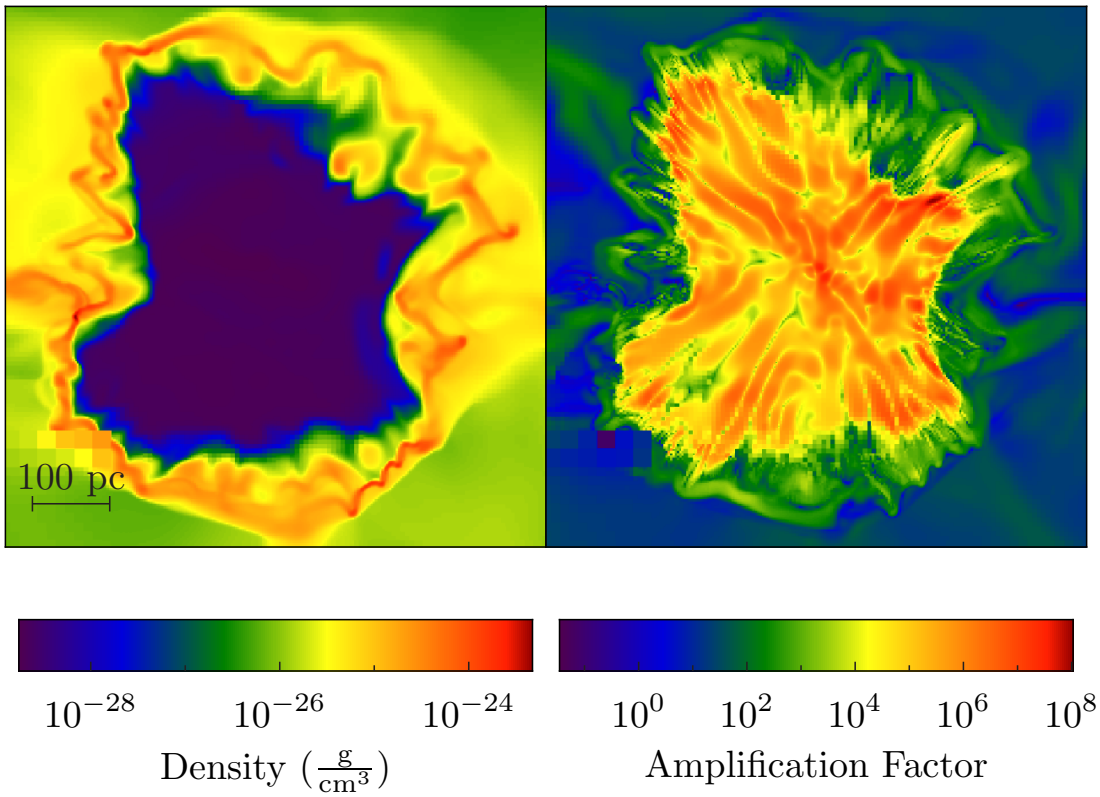


Figure 3.8: Slice of density (left) and amplification factor (right) centered around the stellar remnant at the end of the H2R.B1 run. Each slice spans 700 pc. Relatively strong magnetic field strengths exist inside the shell having been significantly amplified in the wake of the forward and reverse shocks. The strongest magnetic fields on the order of a few nG exist in the shell.

been compressed and vortical motions have begun to grow leading to amplification factors on the order of 100.

*Time Evolution*

In Figure 3.9, we show the distribution of the proper field strengths and amplification factor in a sphere of approximately 37.5 kpc centered at the most massive halo which approximately captures the entire Lagrangian volume of the collapsing large-scale environment. The total gas mass in this volume is approximately $3 \times 10^8$ $M_\odot$, which can be used to estimate the gas mass above each multiple of the standard deviation. We plot these quantities as a function of lookback time from the end of the simulation.

Only the top half of the distribution of field strengths is shown through filled in colors while the very bottom line shows the mass-weighted median. The median proper field strength decreases as the scale factor increases since $B \propto a^2$.

In the top panel showing the magnetic field strength, there are two prominent peaks. The first peak is at the gravitational collapse of the halo immediately prior to the formation of the Pop III star when the density reaches a peak at $3.8 \times 10^{-18}$ g cm$^{-3}$. As the H II region grows and evacuates the gas from the halo, the magnetic field strength decreases along with the gas density. The radial forcing and lack of vortical motions in the ionization front suppresses any field amplification. The second peak follows the death of the star when the supernova produces a shock that compresses the field as it propagates outwards. The first peak hits a maximum at $10^{-4}$ G indicating an amplification of over six orders of magnitude. This is consistent with the results of Sur *et al.* [88] who also saw similar levels of amplification. Only a small fraction of the magnetic field in the total volume manages to reach this high level of amplification. While the shock is able to significantly compress the gas, the highest densities are reached at the birth of the star.

The amplification factor evolution differentiates itself from the magnetic field strength evolution with only a single significant peak following the death of the star. To start, the amplification factor shows a sharp increase around 100 Myr before the end of the simulation. This can be attributed to the virialization of the halo generating some turbulence [138]. Following this period, there is a slight steady increase in the amplification factor as the halo collapses. King and Coles [125] demonstrated that for an anisotropic collapse, $\alpha$ may fluctuate as high as 0.9, where recall $B \propto \rho^{\alpha}$. As the initial peak in the magnetic field evolution was due to compressional effects, which is removed by our scaling of the amplification factor, we observe no significant peak at this point. The most significant amplification occurs following the supernova where the instabilities formed as the supernova cools results in increased turbulence.

This turbulent field will then induce stretching and twisting of the magnetic fields through dynamo action resulting in amplification.

In order to get the magnetic field amplification at larger scales, we calculated the magnetic energy spectrum taking a 1 kpc box with a resolution of 0.71 proper pc (AMR level 7) centered about the star particle at the end of the simulation, 2 Myr after the supernova. We found the peak of this spectra to be $k \sim 50\text{kpc}^{-1}$, corresponding with a coherence length of 20 pc using the definition in Seifried *et al.* [139]. At the end of the run, the radius of the blast wave is around 100 pc. This ratio between the blast wave radius and the coherence length is in agreement with Seifried *et al.*

We also show the time evolution of magnetic, kinetic, and thermal energies in Fig. 3.10. The quantities are the total energies within a sphere of radius 200 pc, which is approximately the virial radius of the host halo, centered around the star particle. The evolution of the magnetic energy shows the two peaks previously described in Fig. 3.9. In the bottom panel, we plot the ratio of the magnetic energy to both the kinetic energy and total energy. At the time of collapse, when the magnetic energy is at a global maximum, we see that the kinetic energy dominates the magnetic term by 5 orders of magnitude. This shows that the magnetic term is never dynamically significant consistent with our earlier conclusions.

## 3.4 Discussion

Our simulations show that magnetic fields are amplified mostly strongly via self-consistent turbulence generated by mechanical compression and the initial field strength plays little role in the subsequent level of amplification.

In our simulations, we have required that the Jeans length be resolved by 64 cells along each dimension. As Turk *et al.* [128] and Sur *et al.* [88] has shown, although 64 cells is sufficient to resolve the action of the dynamos, it may not be enough to fully

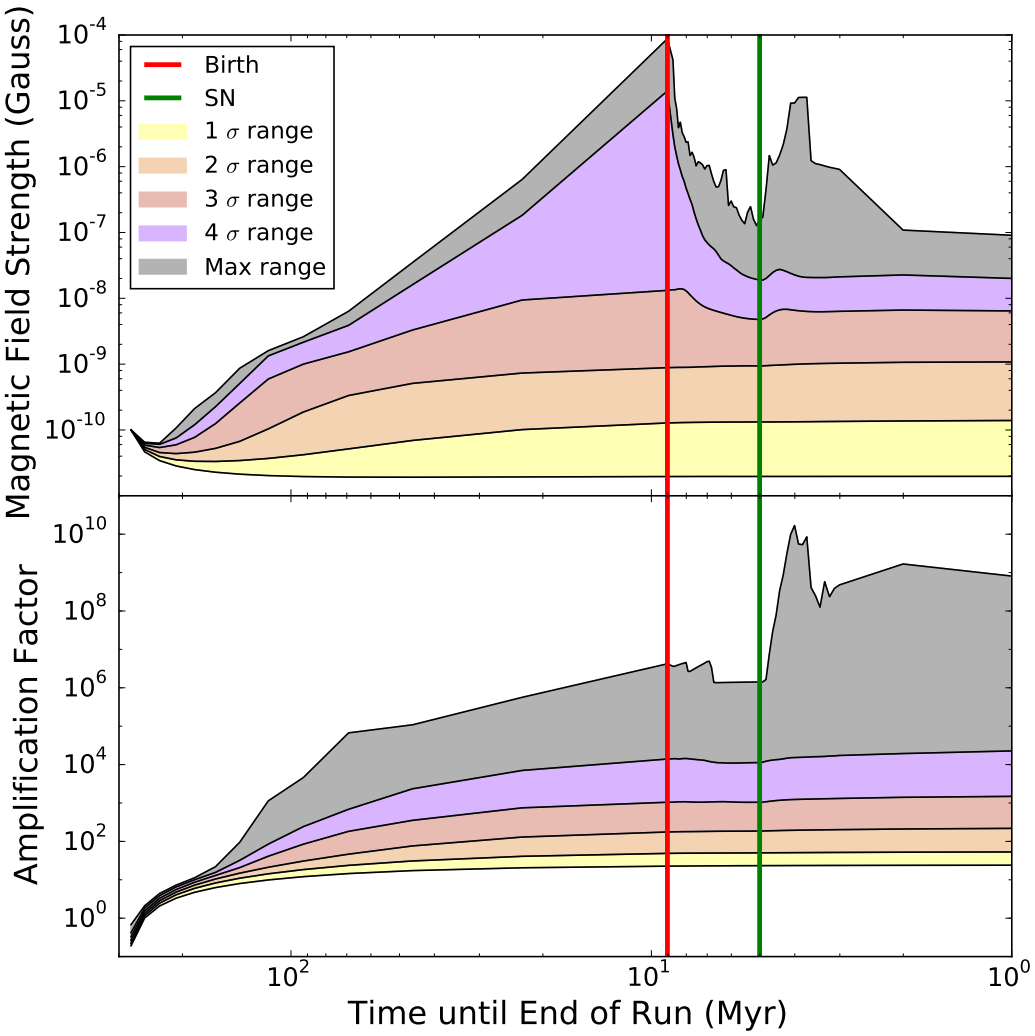


Figure 3.9: Magnetic field strength (top) and amplification factor (bottom) as a function of time until the end of the simulation in the B1 run. We define the amplification factor to be the ratio $u_{\rm B}/\rho^{4/3}$ normalized by $u_{\rm B_0}/\rho_0^{4/3}$ where $u_{\rm B_0}$ is the initial seed field energy and $\rho_0$ is the cosmic mean baryon density. $u_{\rm B}$ is defined as $\rm B^2/8\pi$. Only the $+\sigma$ distributions are shown. The field strength shows two peaks, once at the birth of the star and once following the supernova while the amplification factor shows only one peak.

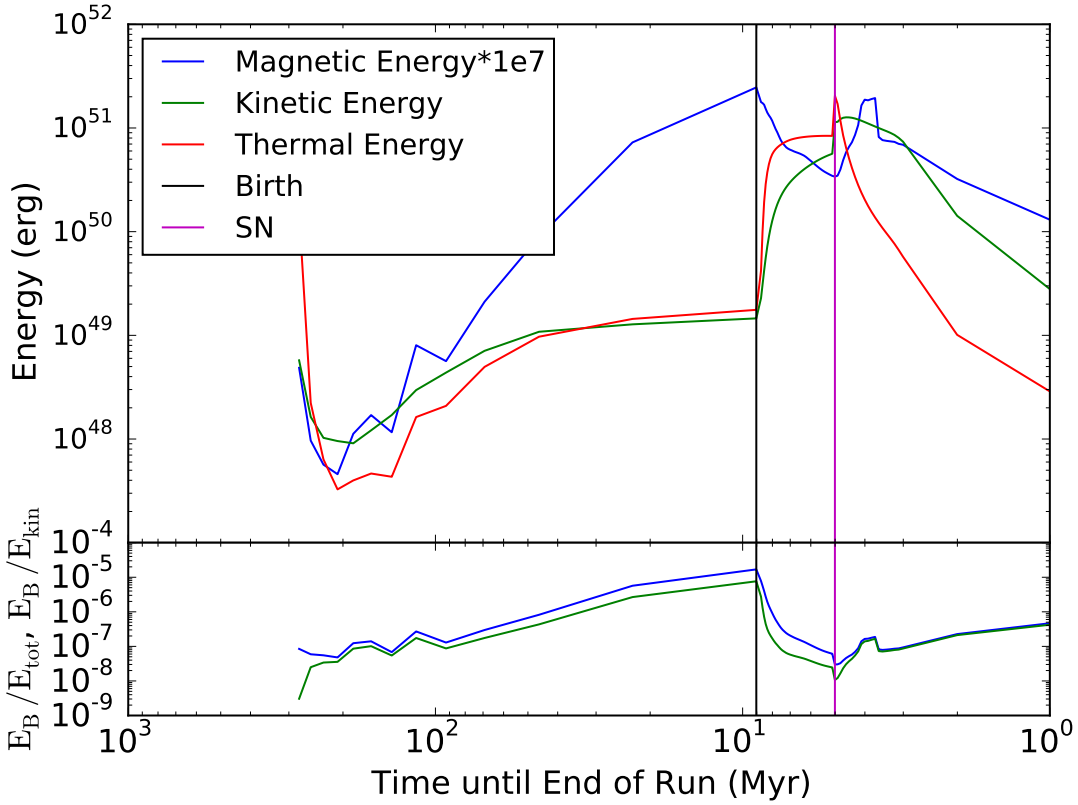


Figure 3.10: Magnetic, kinetic, and thermal energies as a function of time until the end of the simulation in the B1 run. These total energies are computed within a sphere with a radius of 200 pc, approximately the virial radius of the host halo, centered around the star particle. The magnetic energy has been scaled by $10^7$ for better comparison to the other quantities. The vertical black and magenta lines denote the birth and death of the star. The panel below shows the ratio of the magnetic energy to the kinetic energy (blue) and total energy (green).

resolve the amplification of the fields as a result of the dynamos. Our simulations do not show any signs of magnetic saturation, and thus equipartition, and our results can thus be taken as a lower limit to the field strength. However, due to computational constraints, we were unable to increase the resolution preventing any declarative statement about convergence.

In our simulations, we have only considered the ideal MHD limit in which the flux-freezing approximation holds. The only dissipation observed is a numerical artifact resulting from the finite resolution of the simulation. We do not consider the effects of Ohmic resistivity, ambipolar diffusion, nor magnetic reconnection. Although the calculated values of plasma $\beta \gg 1$ and $M_{\rm A} \gg 1$ validate the approximation, our need for higher resolution may require taking non-ideal effects into account as a result. In particular, the effects due to magnetic reconnection in the vicinity of the star may produce significant deviations in the amplification process.

Missing physics that may have dynamical effects include streaming velocities and stellar magnetic fields. First, the relative velocity differences of dark matter and baryonic gas [110] results in a delayed collapse of halos which may have important dynamical impact [e.g. 111, 112, 140]. Namely, the increased velocity in the gas may produce a greater shearing effect which would increase the turbulence, invoking greater amplification of the magnetic fields.

Secondly, stars can themselves generate powerful magnetic fields. A fraction of galactic O-type stars with masses up to 60 $M_\odot$ have been observed to have surface magnetic field strengths of $\sim$ 100 G [141]. Moreover, magnetic fields in protostellar disks can be sufficiently amplified leading to field strengths capable of driving jets [142]. These fields are coherent at scales up to 1000 AU with a corresponding jet luminosity of $\sim 10^6$ $L_\odot$. Furthermore, the magnetic fields produced in the form of supernova feedback can also play a significant role [143]. While these fields may be significantly below our current effective computational resolution, future simulations

where higher resolutions are demanded may need to include these effects.

## 3.5 Conclusions

In this paper, we present the amplification of the magnetic field in the H II region throughout the lifetime of a single Pop III star and its supernova. We simulated three different runs including a base case without any magnetic fields, and two others with an uniform initial background proper field strength of $10^{-10}$ G and $10^{-14}$ G. In each simulation, a single Pop III star of 40 $M_\odot$ forms in the most massive halo at $z \sim 15$ in the central metal-free molecular cloud and subsequently emits radiation until its death in the form of a supernova injecting $10^{51}$ erg into its surroundings. The simulation ends after about 2 Myr after the death of the star as the shockwave continues to propagate outwards. We tracked the evolution of the magnetic field throughout each of the simulations and found the following main results.

1. Magnetic fields are amplified primarily through compression during the gravitational collapse prior to star formation and scales as $\rho^{2/3}$ as expected from ideal collapse scenarios.

2. We find no significant amplification during the growth of the H II region as the star evacuates the gas from its host halo and photoevaporates nearby halos and filaments.

3. Once the supernova remnant begins to cool and fragment, the resulting turbulent velocity in and near the the supernova shell further amplify the magnetic field through small-scale dynamo action. Here the field strengths have a log-normal distribution with an average amplification factor of 120. Within the shell, the field strength is on the order of a few nG at a number of 1 $cm^{-3}$.

4. The amplitude of the amplification is largely independent of the initial seed field strength. The peak level of amplification occurs in the interior of the blastwave,

where the resulting field strength is six orders of magnitude greater than the amplification levels expected in a spherical collapse.

Our simulations show the potential for dynamically important magnetic fields to be produced in the first galaxies. With stronger background field strengths closer to observed limits and the inclusion of fields generated by stars, the amplification mechanisms described in this paper can produce dynamically important fields. Our work elucidates the magnetic field "initial conditions" in the protogalactic gas that will collapse in descendant halos, forming low-mass metal-enriched galaxies. Future calculations will follow its evolution to study the impact of magnetic fields on the transition from Population III stars to the first generations of galaxies, possibly affecting the nature of star formation in such objects.

# CHAPTER 4
# EXTENDING SEMI-NUMERIC REIONISATION MODELS TO THE FIRST STARS AND GALAXIES

Our simulation work from the previous chapters have been limited computationally for us to study the long-term impact of this primordial structures on the Epoch of Reionization. The large dynamical range required to accurately treat the physics of this process necessarily leads to compromises in accuracy. In this chapter, we extend a popular semi-numeric model to study the Epoch of Reionization and the effect of mini-halos on the progression of reionization. This method enables us to quickly generate large volumes and the time evolution of such volumes. This work has been submitted for publication in the Monthly Notices of the Royal Astronomical Society. This work was co-authored by John Wise who provided the initial idea to use 21cmFAST.

## 4.1 Introduction

Models of the Epoch of Reionisation (EoR) have been extensively improved over the years as tighter observational constraints are provided. This particular phase transition of the universe can provide a number of insights into the details of the beginnings of structure formation [144].

The biggest current observational constraint in modeling EoR comes from the Thomson scattering optical depth, $\tau_{\rm e}$, to the cosmic microwave background (CMB). Improvements to the measurement have progressively driven down this particular value, where the latest results estimate $\tau_{\rm e} = 0.0596 \pm 0.0089$ corresponding to a redshift of instantaneous reionsation of $z = 8.0^{+0.9}_{-1.1}$ [58]. Next, the transmission fraction of quasar light through the intergalactic medium shows that the EoR ended by $z \sim$

6 [61, 60], though there are some recent observations implying that it may not have been completed until z $\sim$ 5.6 [145, 146]. Interestingly, it was previously expected that quasars alone could not produce the needed number of ionising photons to complete reionisation as earlier constraints from Wilkinson Microwave Anisotropy Probe (WMAP) introduced a need for high-redshift sources [e.g. 147, 148]. However, with the updated Planck results requiring a later start to reionisation, quasars have come back in recent models, in some of which they are the only sources [149].

Theoretical efforts in the modeling EoR has ranged from relative simple analytic models [150, 151, 152] all the way to high-resolution numerical simulations with various detailed star and galaxy formation prescriptions that include self-consistent ray tracing [153, 154]. Reionisation necessitates a large number of approaches due to the wide range of scales involved in the process. Moreover, a full numerical solution would require parsec scale resolution to correctly follow sources and feedback in, at minimum, a 100 comoving $\mathrm{Mpc}^3$ box to get convergent histories [155]. Such simulations would be an enormous computational cost.

Semi-numeric models are thus an attractive alternative. Such models can accurately generate full three-dimensional density, velocity, and ionisation fields without the need to follow the underlying physics [156, 157, 158]. These models make the following fundamental assumption that overdense regions drive the ionisation process. With this assumption, one asserts that if the number of available photons exceeds the number of baryons in a cell, the cell must be ionised. This simple model provides a powerful tool that compares favorably with high-resolution radiative transfer numerical simulations [159].

Within the numerous models, there have been many efforts to understand the role of the various potential sources in the reionisation process. Typical models only consider galaxies hosted by atomic-cooling halos above $T_{\mathrm{vir}} \sim 10^4$ K. However, an often neglected source is mini-halos with $M < 10^8\,\mathrm{M}_\odot$ containing massive, metal-

free Pop III stars. Pop III stars have been studied extensively over the past decade detailing their formation [21, 29, 111], their spectral properties [121, 122], and their final fates [42, 43, 96]. Of more interest to the EoR, these massive stars also produce extended H II regions in their immediate vicinity spanning 1-3 kpc [38, 37, 39, 40]. These H II regions will then grow out further as mini-halos merge together to form the first galaxies providing additional ionising flux. Ahn *et al.* [160] used a sub-grid model to populate mini-halos in a 114 Mpc $h^{-1}$ simulation and showed their addition had a significant effect in determining the onset of reionisation. Furthermore, Wise *et al.* [161] calculated the escape fraction of ionising photons in a 1 comoving Mpc radiation hydrodynamics simulation showing that mini-halos can contribute up to 30 percent of the ionising photon budget.

Given the extensive volume of data available from large volume high-resolution simulations at high redshifts, we can take simulated physical properties of ionising sources, such as the photon escape fraction and star formation efficiency. In this work, we take these calculated properties to create a new parameterization extending existing semi-numeric models to include the effects of mini-halos.

In the immediately following Section 4.2, we introduce our new parameterization. In Section 4.3, we compare the ionisation histories produced from our model and show the resulting bubble size distributions. Finally, in section 4.4, we provide a short discussion and summarize our results.

## 4.2 Methods

### 4.2.1 Simulating Reionisation

Our treatment involves use of the semi-numerical reionisation simulation code 21CM-FAST [162]. In this code, the ionisation field is generated following an excursion-set

approach [156]. Namely, a cell is considered to be ionised when

$$f_{\rm coll}(x, M_{\rm min}, R, z) \geq \zeta^{-1} \tag{4.1}$$

where $\zeta$ is the ionisation efficiency, and $f_{\rm coll}$ is the fraction of collapsed mass inside a region of size $R$ in halos whose mass is greater than $M_{\rm min}$ [157, 158]. This value $R$ is iterated from $R_{\rm max}$, which is typically taken to be the maximum horizon of ioinising photons, or the effective mean free path down to the length of a single cell. These three parameters then fully determine the ionisation state at any given redshift. Our simulations are run on a box with a 100 comoving Mpc side length using $2048^3$ cells down-sampled to $1024^3$ cells to generate the ionisation field. The main contribution in this work is our detailed treatment of the parameter $\zeta$ which is outlined in the following sections.

### 4.2.2 Calculating the Ionising Efficiency

In previous treatments, $\zeta$ typically represents a homogeneous ionising efficiency factor for all star-forming galaxies in any environment. A typical parameterization is provided in Greig and Mesinger [163] as

$$\zeta = 30 \left(\frac{f_{\rm esc}}{0.2}\right)\left(\frac{f_*}{0.03}\right)\left(\frac{f_{\rm b}}{\Omega_{\rm b}/\Omega_{\rm m}}\right)\left(\frac{N_{\gamma/{\rm b}}}{4000}\right)\left(\frac{1.5}{1+n_{rec}}\right) \tag{4.2}$$

where $f_{\rm esc}$ is the fraction of ionising photons escaping into the intergalactic medium (IGM), $f_*$ is the fraction of galactic gas in stars, $f_{\rm b}$ is the baryon fraction inside haloes hosting galaxies in units of the cosmic baryon fraction, $N_{\gamma/{\rm b}}$ is the number of ionising photons per baryon in stars, and $n_{\rm rec}$ is the average number of recombinations per baryon in the IGM. These values are all assumed to be mass- and redshift-independent to produce a single $\zeta$ value. We take this model to be the Fiducial case and compare our new parameterization against it in Sec 4.3.

The main improvement of this work is to model $\zeta$ as a function of the host halo mass at a given redshift. This class of parameterizations has been initially explored by Furlanetto *et al.* [164] but they only considered a simple power-law function setting $\zeta \sim m^{\alpha}$ for various values of $\alpha$. In our work, we consider a more extensive dependence on the host halo mass that is better physically motivated. This allows us to incorporate the distribution of ionising efficiencies at different masses as well including the contribution of mini-halos to the photon budget for reionisation.

In particular, $\zeta$ has been parameterized as follows.

$$\zeta(M_{vir}) = \begin{cases} \zeta_{0,3}\ f_{\rm esc}\ f_*\ N_{3,\gamma/\rm b}\ f_{t*} & M_{\rm min} \leq M_{\rm vir} < M_{\rm filter} \\ \zeta_{0,2}\ f_{\rm esc}(M_{\rm h})\ f_*(M_{\rm h})\ f_{\rm occ}(M_{\rm h})\ N_{2,\gamma/\rm b} & M_{\rm vir} \geq M_{\rm filter} \end{cases} \tag{4.3}$$

where $N_{3,\gamma/\rm b}$ is $N_{\gamma/\rm b}$ for Pop III stars, $f_{\rm t*}$ is the fractional star-formation timescale for Pop III stars, $f_{\rm occ}$ is the fraction of halos containing star-forming galaxies, and $N_{2,\gamma/\rm b}$ is $N_{\gamma/\rm b}$ for galaxies. Lastly, $\zeta_{0,3}$ and $\zeta_{0,2}$ are constants calibrated to the desired reionisation history. In this work, we take these values to be 2 and 3 respectively.

Furthermore, the domain of $\zeta$ is characterized by two different masses. First is $M_{\rm min}$, which is the minimum mass of mini-halos that is required to collapse to form Pop III stars. This mass is determined by the strength of the soft $H_2$ photodissociating Lyman-Werner (LW) flux by

$$M_{\rm min}({\rm F_{LW}}) = 1.25 \text{ x } 10^5 + 8.7 \text{ x } 10^5 \left(\frac{\rm F_{LW}}{10^{-21}}\right)^{0.47} \tag{4.4}$$

taken from Machacek *et al.* [33], where $\rm F_{LW}$ is the strength of the LW background in units of erg $\rm s^{-1}$ $\rm cm^{-2}$ $\rm Hz^{-1}$. The magnitude of this flux as a function of redshift is

modeled as

$$\log\ J_{21}(z) = A + Bz + Cz^2 + Dz^3 + Ez^4 \tag{4.5}$$

where (A,B,C,D,E) = (-2.567, 0.4562, -0.02680, 5.882 x $10^{-4}$, -5.056 x $10^{-6}$) taken from Wise *et al.* [132]. Here $J_{21}$ is the specific intensity in units of erg $s^{-1}$ $cm^{-2}$ $Hz^{-1}$ $sr^{-1}$. In this fit, the strength of the background peaks at z = 13.765 with a value of $J_{21} = 0.97$ after which galaxies would dominate the contribution. As the actual minimum mass for collapse would be dependent on the exact environment of the halos, we set the LW background to be this maximum value of this fit at subsequent redshifts. At these redshifts, the exact value has minimal impact on the resulting reionisation history because galaxies provide the bulk of the photon budget.

The other relevant characteristic mass is the filtering mass, $M_{\rm filter}$, which is the characteristic mass scale below which reionisation suppresses gas fraction in low-mass halos [165] given by

$$M_{filter}^{2/3} = \frac{3}{a}\int_0^a da' M_J^{2/3}(a')\left[1 - \left(\frac{a'}{a}\right)^{1/2}\right] \tag{4.6}$$

where $M_J$ is the Jeans mass and $a$ is the cosmological scale factor. We calculated $M_{\rm filter}$ from the simulations of Wise *et al.* [132] and created a polynomial fit as a function of redshift for computational ease given by

$$\log\ M_{\rm filter}(z) = A + Bz + Cz^2 + Dz^3 \tag{4.7}$$

where (A,B,C,D) = (9.065, -0.15611, 0.0063, -1.9577 x $10^{-4}$). This $M_{\rm filter}$ is then used as the mass cut-off above which galaxy formation occurs at a given redshift. From $M_{\rm min}$ to $M_{\rm filter}$, we assume Pop III stars are the dominant contributors, while for $M_{\rm vir} > M_{\rm filter}$, galaxies dominate. For the rest of this work, we define mini-halos as halos with masses in the range $M_{\rm min} \leq M_{\rm vir} < M_{\rm filter}$ whose dominant ionising source

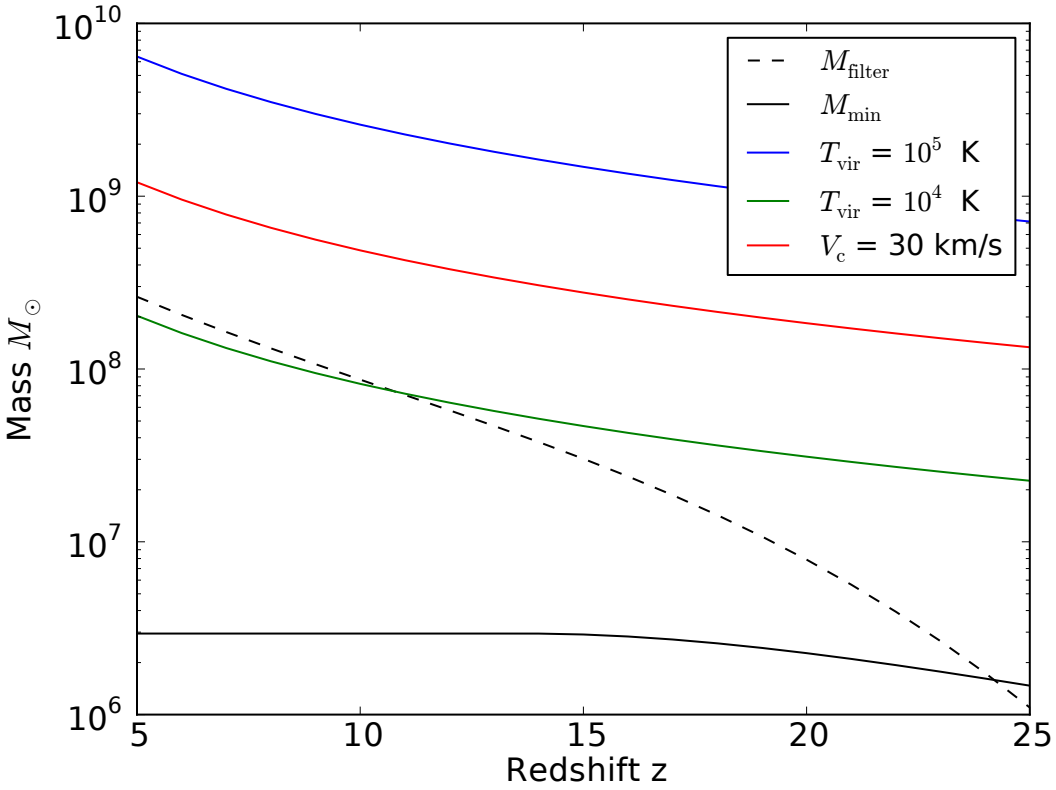


Figure 4.1: Characteristic masses as a function of redshift. The minimum mass, $M_{\rm min}$ (black, solid), is the mass above which ionising sources exist. The filtering mass, $M_{\rm filter}$ (black, dashed), is the threshold between Pop III mini-halos and galaxies. That is, any mass range between these two lines will be assumed to be a mini-halo, while any mass range above the dashed line will host galaxies. For comparison, we also show commonly assumed minimum masses corresponding to a virial temperature $T_{\rm vir} = 10^4$ K (green), $T_{\rm vir} = 10^5$ K (blue), and circular velocity, $V_{\rm c} = 30$ km/s (red).

is Pop III stars.

These characteristic masses are shown in Fig 4.1. When $M_{\rm filter} > M_{\rm min}$, which happens at z $>$ 24, we set $\zeta$ to be 0 as no galaxies can be formed. We can see that our adopted $M_{\rm filter}$ is much less than any of the typically adopted minimum mass values at z $>$ 15, greatly increasing the number of available galaxies to produce ionising photons.

*Mini-halos*

For mini-halos ($M_{\rm min} \leq M_{\rm vir} < M_{\rm filter}$), the photon contribution is assumed to be entirely from Pop III stars. Given the large uncertainty and lack of observational constraints for the relevant parameters for the first stars, we take each value in the parameterization to be mass- and redshift-independent in the relevant ranges for Pop III stars. Instead, we consider the possible range of values in Sec. 4.2.2.

First, $f_{\rm esc}$ is the parameter with the largest uncertainty [39], which we adopt a value of 0.6. We set $f_*$ to be a constant at $100\,{\rm M}_\odot/10^6\,{\rm M}_\odot$ which is a typical ratio found in cosmological simulations of Pop III star formation [118, 41]. The number of photons per baryon, $N_{3,\gamma/{\rm b}}$ is largely determined by the surface temperature of the star. We take this value to be 50,000 [122]. Lastly, we introduce a term $f_{{\rm t}*}$, the fractional star-formation timescale defined as the average lifetime of a Pop III star over the recovery time, to account for the fact that Pop III formation events are bursty. Pop III stars can very efficiently photoevaporate their surroundings and their supernova completely disrupt the host halo [45, 114]. This results in a significant delay until the subsequent generation of star formation [50]. We take this value to be 5 Myr/30 Myr.

*Galaxies*

For halos with $M_{\rm h} > M_{\rm filter}$, galaxies dominate the photon budget following the death of Pop III stars. For this range of masses, we take a number of fits from cosmological galaxy simulations to calculate $\zeta$.

The photon escape fraction, $f_{\rm esc}$, is modeled using the piece-wise fit below

$$\log\ f_{\rm esc}(M_{vir}) = \begin{cases} -0.51 - 0.039\ \log\ M_{\rm vir} & \log\ M_{\rm vir} \geq 8.5 \\ 2.669 - 0.413\ \log\ M_{\rm vir} & 7 \leq \log\ M_{\rm vir} < 8.5 \\ -0.222 & \log\ M_{\rm vir} < 7 \end{cases} \tag{4.8}$$

taken from Kimm and Cen [166] who used high-resolution zoom-in simulations to construct the fit. This fit takes a nominal value of $f_{\rm esc} = 0.6$ for halos below log $M_{\rm vir}/\,{\rm M}_\odot < 7$, matching our assumed value for mini-halos, with a steep decrease for $7 <$ log $M_{\rm vir}/\,{\rm M}_\odot < 8.5$ and then flattens off for log $M_{\rm vir}/\,{\rm M}_\odot > 8.5$ to $f_{\rm esc} \sim 0.1$. This is consistent with other simulations showing high escape fractions for low mass galaxies [167, 168].

To determine the stellar mass fraction, we use a combination of fits taken from O'Shea *et al.* [169] and Behroozi *et al.* [170]. From the former, valid for the range log $M_{\rm vir}/\,{\rm M}_\odot < 10$, we have

$$f_*(M_{\rm vir}) = 1.26\ {\rm x}\ 10^{-3} \left(\frac{{\rm M}_{\rm vir}}{10^8\,{\rm M}_\odot}\right)^{0.74} \tag{4.9}$$

fitted using data from the Renaissance Simulations that focus on galaxy formation during the EoR. These simulations have found that galaxy properties during EoR are largely independent of redshift [171]. From the latter, valid for the range log $M_{\rm vir} \geq 10$, we have

$$\log\ f_*(M_{\rm vir}, z = 6) = \log\ (\epsilon M_1) + f\left(\log\ \left(\frac{M_{\rm vir}}{M_1}\right)\right) - f(0) - \log\ M_{\rm vir} \tag{4.10}$$

where $\epsilon$, $M_1$, and the function $f$ are heavily involved parameters.The exact details of this parameterization can be found in Behroozi *et al.* [170]. We take this fit at only z

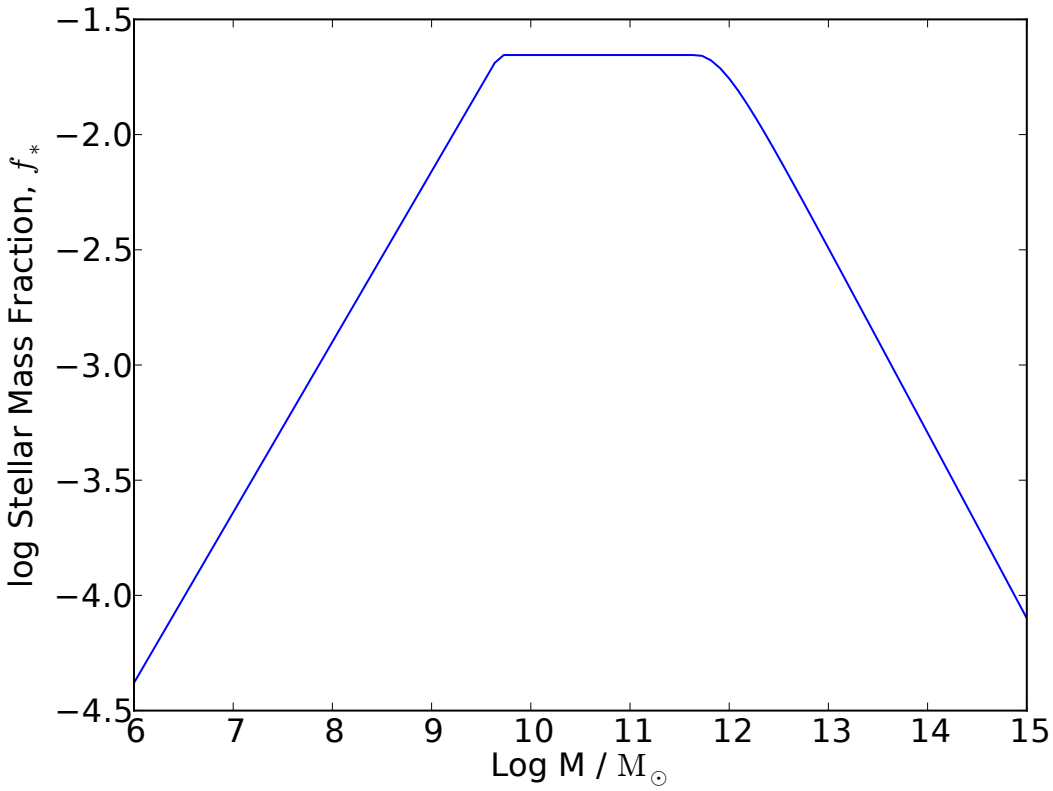


Figure 4.2: Stellar mass fraction as a function of host halo mass. The lower mass end power law is taken from O'Shea *et al.* [169] while the high mass end is taken from Behroozi *et al.* [170] at z = 6. We approximate the stellar mass fraction in the central mass ranges to be equivalent to the peaks of both ends to maintain continuity.

= 6 and apply for all redshifts to maintain continuity for all mass ranges. Figure 4.2 shows the combined fits of $f_*$ at various redshifts. In order to remove discontinuities in combining the two fits, we extrapolate Eq. 4.9 until $f_* = 0.022$, or equal to the maximum of Eq. 4.10 at z = 6. Then we assume a constant $f_*$ in the range between the two fits to connect them continuously. This imposed ceiling is largely consistent with the results from high-redshift numerical simulations which show a maximum stellar fraction [172, 166, 173, 174].

One component in the $\zeta$ for galaxies that is not in the $\zeta$ for mini-halos is the halo occupation fraction, $f_{\rm occ}$. This parameter takes into account for the fact that not every halo has a stellar population that provides ionising photons. Thus, it dampens

the contribution from young low-mass halos which have bursty star formation periods. This relation is given by

$$f_{\rm occ}(M_{\rm h}) = \left[1 + \left(2^{\alpha/3} - 1\right)\left(\frac{M_{\rm h}}{M_{\rm c}}\right)^{-\alpha}\right]^{-3/\alpha} \tag{4.11}$$

taken from O'Shea *et al.* [169] based on the form from Okamoto *et al.* [175] where $\alpha = 1.5$ and $M_{\rm c} = 6.0$ x $10^7\,{\rm M}_\odot$. This function exponentially drops off below 1 for masses below the characteristic mass, $M_{\rm c}$. Above this mass, the fraction quickly approaches unity implying every halo contains ionising sources. Finally, we take $N_{2,\gamma/{\rm b}}$ to be a constant 4000 photons per baryon [176].

*Putting it Together*

Figure 4.3 shows $\zeta$ as a function of halo mass for a number of redshifts. The biggest contribution in the range $9 \leq \log M_{\rm vir}/\,{\rm M}_\odot < 12$ is due to the peaking of $f_*$. These galaxies have large $f_*$ while still having $f_{\rm esc} > 0.1$ and thus provide the largest fraction of ionising photons. For $\log M_{\rm vir}/\,{\rm M}_\odot > 12$, star formation becomes inefficient represented by a steep decline in $\zeta$. At the lower mass end below $\log M_{\rm vir}/\,{\rm M}_\odot < 8$, the star forming halo occupation fraction greatly depresses $\zeta$. Because we assume redshift-independent star formation parameters for $\zeta$ above the filtering mass, we see the values of $\zeta$ overlapping.

Given these distributions, we take a weighted average to get a single $\zeta$ value for a given redshift. First, we take the halo mass function (HMF) at a given redshift. We use the following form

$$\frac{dn}{dM} = f(\sigma)\frac{\bar{\rho}_m}{M}\frac{d\,\ln\,\sigma^{-1}}{dM} \tag{4.12}$$

taken from Tinker *et al.* [108] calculated using the python software package Rabacus [109]. We then normalize the HMF at $M_{\rm min}(z)$ to be 1. Now we can define $n_{\rm frac}$ to be the fraction of halos at a mass range between $M$ and $M + dm$ by taking the difference

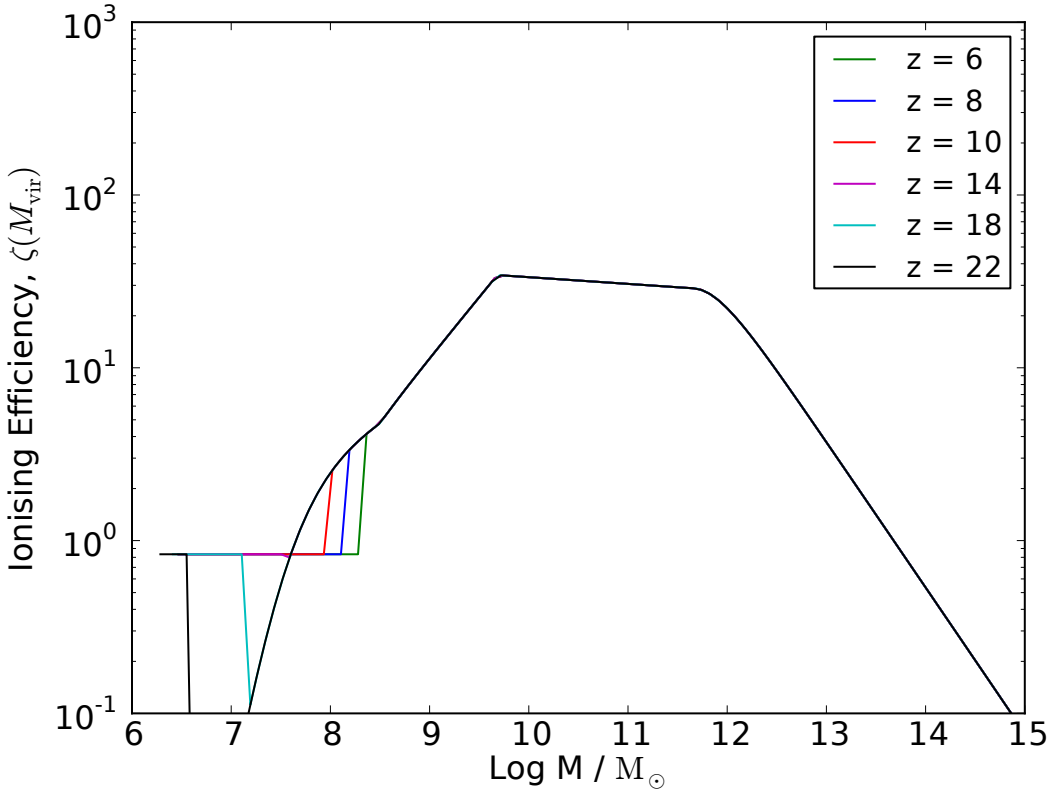


Figure 4.3: Ionising efficiency, $\zeta$, as a function of host halo mass at various redshifts. For masses $M_{\rm min} \leq M_{\rm vir} < M_{\rm filter}$, we assume Pop III stars are the dominant ioinisation sources and assume a constant $\zeta$. Both $M_{\rm min}$ and $M_{\rm filter}$ evolve with redshift and the latter acts a moving threshold between mini-halos and galaxies. For galaxies, we take the distribution of ionising efficiencies as a function of the halo mass to be independent of redshift. The values of $\zeta$ all overlap above $M_{\rm filter}$ as we assume a redshift-independent $f_*$ for galaxies.

of the normalized HMF at those values.

We can then take the integrated average of $\zeta$ weighted by halo number density fraction and halo mass as

$$\zeta(z) = \frac{1}{1+n_{\rm rec}} \frac{\int_{M_{\rm min}}^{M_{\rm max}} \zeta(M_{\rm h})\ n_{\rm frac}\ M_{\rm h}\ dm}{\int_{M_{\rm min}}^{M_{\rm max}} n_{\rm frac}\ M_{\rm h}\ dm} \tag{4.13}$$

where $n_{\rm frac}$ is the fraction of halos within a mass range between $M_{\rm h}$ and $M_{\rm h} + dm$. We take $M_{\rm max} = 10^{15}\,{\rm M}_{\odot}$ to consider the full range of halo masses. This integral is similar to that introduced in Furlanetto *et al.* [164], where they took $\zeta$ to have a power-law dependence on the host halo mass instead.

Furthermore, we introduce a mean recombination number per baryon as

$$n_{\rm rec} = C(z)\ t_{\rm H,0}\ \alpha_{\rm B}\ \bar{n}_{\rm H,0}\ (1+z)^{3/2} \tag{4.14}$$

where $t_{\rm H,0}$ is the Hubble time at the present day, $\bar{n}_{\rm H,0}$ is the mean hydrogen number density at the present day, and $\alpha_{\rm B}$ is the case B recombination coefficient at $10^4$ K which is taken as 2.6 x $10^{-13}{\rm cm}^3\ {\rm s}^{-1}$. As our treatment of the recombination number is a global value that only depends on redshift, and not on the halo mass, we can safely evaluate it outside the integral. We also include the clumping factor given by

$$C(z) = \begin{cases} 1 + \exp(-0.28z + 3.50) & z \geq 10 \\ 3.2 & z < 10 \end{cases} \tag{4.15}$$

taken from Pawlik *et al.* [177] to account for the boosted recombination rates in a clumpy IGM. An increased recombination rate requires an increased number of photons to keep the IGM reionised which has the effect of dampening $\zeta$ overall. This is in contrast to the method of Sobacchi and Mesinger [178] where the recombination rate was calculated in each cell to produce the time-integrated number of recombinations per baryon to adjust $\zeta$. We find, however, that both treatments result in a similar

Table 4.1: Coefficients for fits of $\zeta$

| Model | A | B | C | D | E |
|---|---|---|---|---|---|
| Mean | 30.27 | -6.293 | 0.506 | -1.801 x $10^{-2}$ | -2.366 x $10^{-4}$ |
| Lo | 14.74 | -3.088 | 0.248 | -8.902 x $10^{-3}$ | -1.189 x $10^{-4}$ |
| Hi | 51.71 | -1.061 | 0.852 | -2.995 x $10^{-2}$ | -3.820 x $10^{-4}$ |

effect.

Finally, we can then calculate a $\zeta$ for any given redshift. Figure 4.4 shows the calculated $\zeta$ as a function of redshift. The line shows a polynomial fit to $\zeta$ with the functional form given by

$$\zeta(z) = A + Bz^2 + Cz^2 + Dz^3 + Ez^4 \tag{4.16}$$

where the coefficients are shown in Table 4.1. At high redshifts, $\zeta$ remains mostly constant. This is because at these redshifts, the vast majority of ionising sources are mini-halos whose ionising efficiencies we have taken to be a constant value significantly lower than that of galaxies. These smaller objects form smaller H II regions and thus cover only a small volume fraction of the total universe. In contrast, the general trend shows an exponential increase in the ionising efficiency at lower redshifts. Recall that the ionising efficiencies peak in the range $9.5 < \log M_{\rm vir}/\,{\rm M}_\odot < 12$. At these lower redshifts, the number of halos available to produce ionising photons at these mass ranges continually increases as halos merge to form larger structures which results in the boosted $\zeta$. These galaxies with large $f_*$ provide the bulk of ionising photon budget necessary for reionisation. We stress that Eq. 4.16 is only valid for the range $5 < {\rm z} < 25$ as all the parameters have been calibrated from high-redshift simulations.

*Quantifying the Uncertainties*

In order to consider the full range of values given the large uncertainties in certain parameters, we calculated the upper and lower limits to $\zeta$ as a function of redshift.

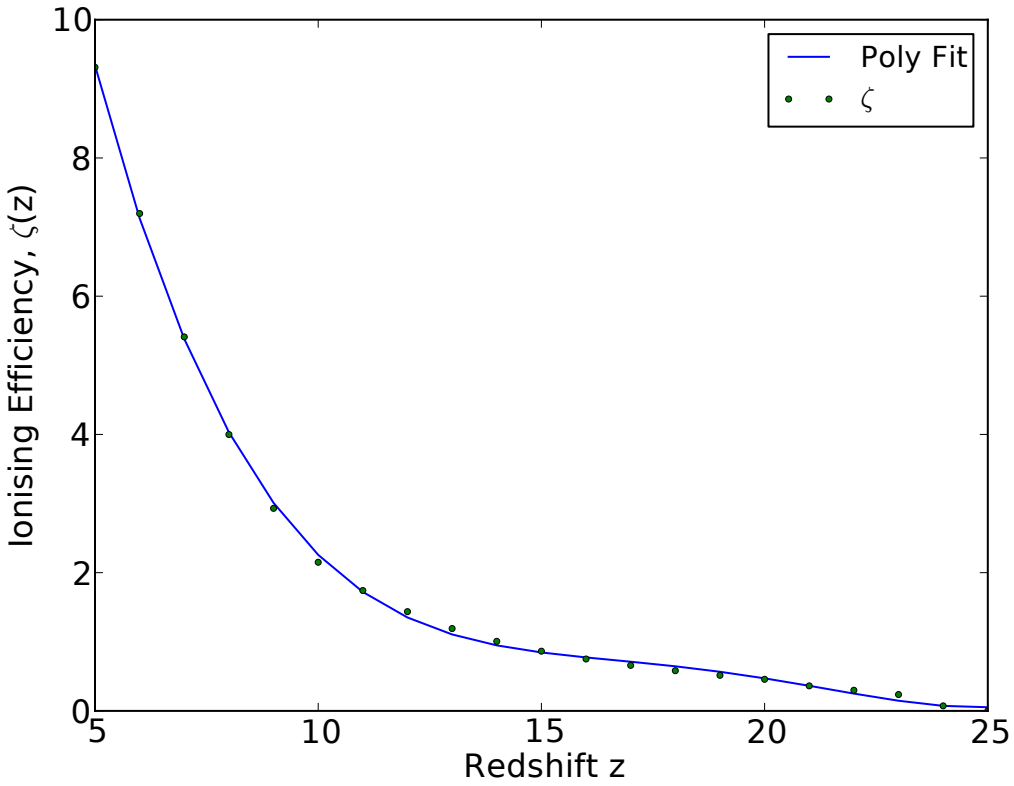


Figure 4.4: Integrated ionising efficiency $\zeta$ as a function of redshift. The dots show the calculated $\zeta$ values at each redshift while the line shows a 4th-order polynomial fit. See Eq. 4.16 for the fit parameters. At high-z, the contribution from mini-halos dominates and suppresses $\zeta$. At low-z, massive galaxies begin to dominate and greatly increases the ionising efficiency.

Table 4.2: Varied parameters and their values

| Parameter | Mean Value | Lo Value | Hi Value |
|---|---|---|---|
| Pop III $f_{\rm esc}$ | 0.6 | 0.05 | 0.9 |
| $f_{t*}$ | $\frac{5\ \rm Myr}{30\ \rm Myr}$ | $\frac{5\ \rm Myr}{100\ \rm Myr}$ | $\frac{5\ \rm Myr}{10\ \rm Myr}$ |
| Galaxy $f_{\rm esc}$ | $f_{\rm esc}\ (M_{\rm h})$ | $f_{\rm esc}\ (M_{\rm h})$ x 0.7 | $f_{\rm esc}\ (M_{\rm h})$ x 1.3 |
| Galaxy $f_*$ | $f_*(M_{\rm h}, z)$ | $f_*(M_{\rm h}, z)$ x 0.7 | $f_*(M_{\rm h}, z)$ x 1.3 |

Table 4.2 shows the list of parameters that we have chosen to vary along with the range. The greatest variances are in $f_{\rm esc}$ reported by Wise *et al.* [161] and Kimm and Cen [166]. For $f_{t*}$, we assume the same lifetime for Pop III stars and only vary the recovery times as reported by Muratov *et al.* [179] and Jeon *et al.* [50]. For the galactic $f_*$, we take the average variances found in Behroozi *et al.* [170]. All other parameters not listed in the table remain as their original definitions.

These values are used to produce the ionisation fields for the upper, lower, and standard values of $\zeta$. They provide a first order approximation to the possible distribution of $\zeta$ values. For both the lower and upper limits, we take a polynomial fit of the same form as Eq. 4.16 to calculate $\zeta$. The coefficients for the resulting fits are found in Table 4.1.

Figure 4.5 shows the corresponding variances in the $\zeta$ function. The blue shaded region shows the resulting variance due to Pop III parameters while the red region shows it for galaxies. The effective combined range of values are represented by the grey area. At high redshifts (i.e. z $>$ 15), the spread is entirely blue indicating only the mini-halos contribute significantly to the photon budget. As structure formation continues, the galactic contribution dominates after z $<$ 10. This is expected as the Pop III star formation rate plateaus as their own formation results in the metal-enrichment of their surroundings suppressing further Pop III formation [97, 180] . Instead, these mini-halos merge together to assemble galaxies with greater star formation rates and larger collapsed structures. Once reionisation is fully underway, the galactic contribution increases exponentially which also increases the spread of

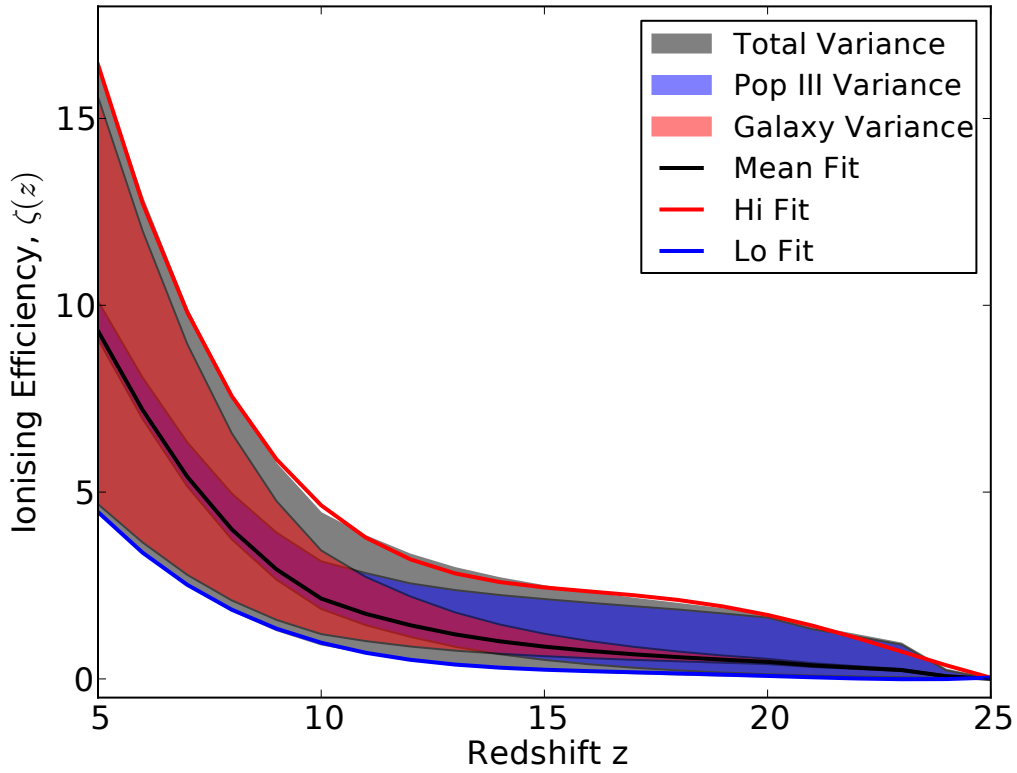


Figure 4.5: Integrated ionising efficiency $\zeta$ as a function of redshift including the spread using both low and high limit values for the various parameters in Eq. 4.3. The blue and red shaded regions show the spread of $\zeta$ due to Pop III and galaxies respectively, while the grey shows the total spread due to the combined variance. The lines also show the polynomial fit to each of the Lo (blue), Hi (red), and Mean (black) values of $\zeta$.

uncertainties at lower redshifts [181].

### 4.3 Results

We run a total of four simulations from the same cosmological initial conditions at z = 300 each with varying $\zeta$ . The high resolution density grid is sampled by $2048^3$ cells which is smoothed over a $1024^3$ grid to produce the ionisation field. We produce 50 snapshots equally spaced in time starting from z = 25 down to z = 6 to produce the entire ionisation history. The fiducial case takes the three parameter model from

Greig and Mesinger [163] consisting of $T_{\rm vir}^{\rm min}$, the minimum virial temperature hosting ionising sources, $\zeta$, the ionisation efficiency, and $R_{\rm mfp}$, the maximum horizon for ionising photons which defines the maximum filtering scale. From their results, we take the best fit values for each of the parameters which are $T_{\rm vir}^{\rm min} = 10^5$ K, $\zeta = 50$, and $R_{\rm mfp} = 20$ Mpc.

In comparison with the fiducial case, we run a total of three simulations with varying values of $\zeta$ as a function of redshift. In each of the runs, rather than taking the minimum virial temperature as a proxy for the minimum mass of ionising halos, we use the minimum mass calculated by Eq. 4.4. The three runs are then the Mean, Hi, and Lo cases which represent the base fit to $\zeta$ and its upper and lower variance values with their fits given in Table 4.1. We keep the same maximum horizon as $R_{\rm mfp} = 20$ Mpc as Sobacchi and Mesinger [178] and Greig and Mesinger [163] have shown that the resulting ionisation fields are largely insensitive to the choice.

### 4.3.1 Reionisation Histories

Figure 4.6 shows the ionisation histories calculated from each of the four runs. We define the start of reionisation, $z_{\rm start}$, to be when the ionised fraction, $x(z)$, is at 10%. Similarly, the end, $z_{\rm end}$, is when $x(z) = 99\%$. The blue line shows the fiducial case which does not quite end up fully ionised at the end at z = 6.0, while $z_{\rm start} = 9.8$. The green line shows the Mean case which also has $z_{\rm start} = 9.8$ and $z_{\rm end} = 6.0$. The fiducial model has a much steeper rise at $z_{\rm start}$ while the Mean case shows a gradual rise in the ionised fraction. In the former, as only halos with $T_{\rm vir} > 10^5$ K are considered, there is a more abrupt increase in the ionised fraction as these halos do not exist in large numbers until lower redshifts. In the latter, as mini-halos begin forming early on at high redshifts, there is a gradual increase in the ionised fraction as Pop III stars continually add on to the photon budget. Moreover, since the value of $\zeta$ is relatively sensitive to Pop III parameters at $z \sim 10$, mini-halos must play a role in determining

the exact starting point of reionisation. Once reionisation is underway, the Mean case shows a steeper increase in the ionised fraction resulting in a slightly earlier end to the EoR. This is mostly due to the steep incline in $\zeta$ at these low redshifts corresponding to the presence of bigger halos with large $f_*$ emitting a significant amount of ionising photons.

The shaded region in green shows the spread in histories where the edges represent the Hi and Lo value cases. The Hi value case has $z_{\rm start} = 11$ and $z_{\rm end} = 6.9$ while the Lo value case has $z_{\rm start} = 8.8$ and only reaches x = 0.45 at z = 6. Given the constraint that the universe is fully ionised by z = 6, much of the lower spread in histories is effectively ruled out. This broadly constrains our parameters, in particular $f_{\rm esc}$ and $f_*$ for galactic populations. However, even considering just the Hi case, there is a broad range of $z_{\rm start}$ as the large mini-halo population quickly drives up the ionised fraction to the threshold fairly early on.

We also calculate the optical depth due to Thomson scattering for each of the runs by

$$\tau_e = \int_0^\infty dz \frac{c(1+z)^2}{H(z)} x(z) \sigma_{\rm T} \bar{n_{\rm H}} (1 + \eta Y/4X) \tag{4.17}$$

where H(z) is the Hubble parameter, $x(z)$ is the ionised fraction of hydrogen, $\sigma_{\rm T}$ is the Thomson cross-section, and $X$ and $Y = 1 - X$ are the hydrogen and helium number fractions respectively. We also assume that helium is singly ionised ($\eta = 1$) at z > 3 and doubly ionised at later times ($\eta = 2$).

The fiducial case produces $\tau_e = 0.0567$ while the Mean case has $\tau_e = 0.0569^{+0.0121}_{-0.0125}$, where the Hi and Lo case $\tau_e$ are represented as uncertainties. Taking the estimated value from the *Planck* 2016 intermediate results of $\tau_e = 0.0596 \pm 0.0089$ [59], we see that our value is still well within the margin of error albeit lower.

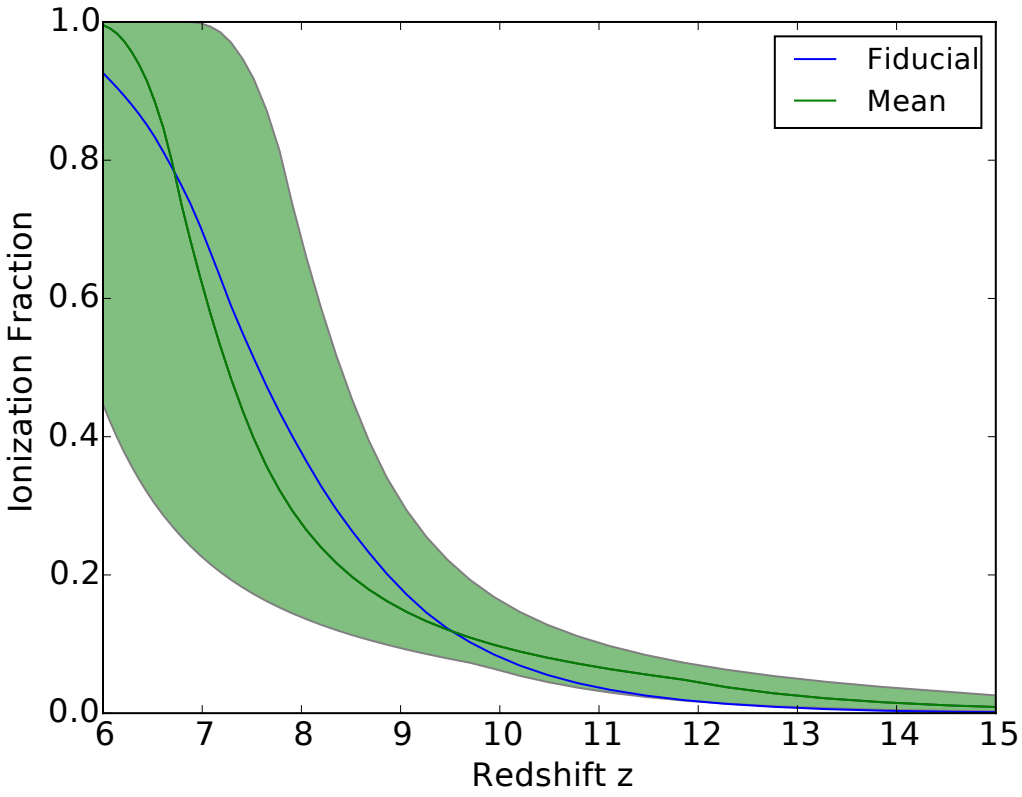


Figure 4.6: Ionisation histories of all four runs. The blue line represents the fiducial run using the three parameter model from Greig and Mesinger [163]. The green line shows the Mean value run using our new parameterization. The shaded region shows the spread in ionisation histories using our Lo and Hi value parameterizations.

### 4.3.2 Bubble Size Distributions

In order to further characterize the differences between our models, we generate ionised bubble size distributions. These distributions tell us about the morphology of reionisation as the H II regions grow and expand. We use the same methodology found in Mesinger and Furlanetto [157] to maintain consistency in generating the distributions. First, we smooth out the ionisation field and remove the partial ionisation values by setting a threshold. We choose this threshold to be 0.5. We then choose an ionised cell and a direction vector at random and measure the distance to the nearest neutral cell. We repeat the process $10^7$ times to get a distribution. This method has been shown to be a good approximation to getting the true distributions [182].

Figure 4.7 shows the generated bubble size distributions for the Mean and Fiducial cases at different ionisation fractions. At any given ionisation fraction, the peak in the distribution function, or characteristic size, of the Mean model is at a lower value compared to the Fiducial case. This can be understood as due to the presence of mini-halos which make up a larger fraction of ionised cells in our model driving the peak down. These mini-halos have small ionising photon luminosities, which would correspond to smaller H II regions. We also see a broadening of the peaks as $x$ increases, which can be attributed to the heightened number of mergers of the bubbles. There are a larger number of small bubbles that merge with the larger bubbles that artificially increase the size. At high $x$, the characteristic size quickly approaches the size of the box in both cases as expected.

Recently Paranjape and Choudhury [183] showed that a correction to remove the correlation in the random walk introduced by the smoothing filter can result in a significant increase in the characteristic sizes. We expect a similar impact should the correction be included.

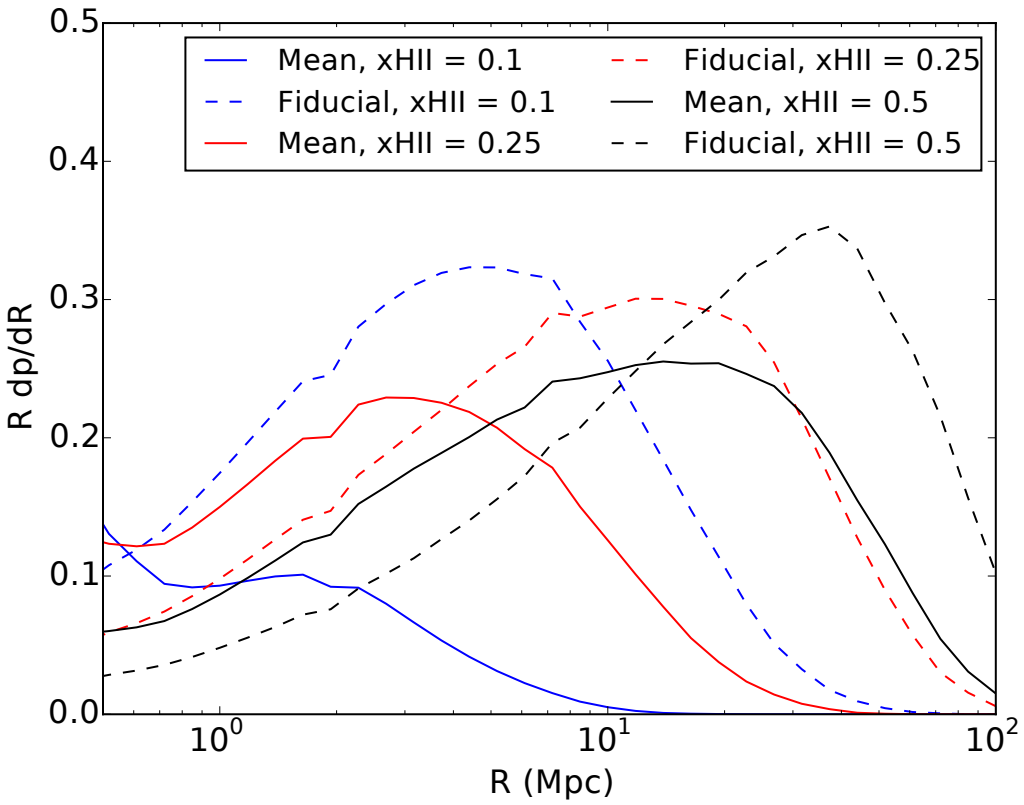


Figure 4.7: Bubble size distributions at $x \approx 0.1$ (blue), $x \approx 0.25$ (red), $x \approx 0.5$ (black) . The Mean case is represented with solid lines and the Fiducial with dashed lines. The dip and peak at R $\sim$ 2 Mpc and $\sim$ 8 Mpc are artifacts from the numerical bubble size distribution calculation.

## 4.4 Discussion and Summary

The greatest strength in our parameterization is that the assumed values are those constrained by the latest numerical simulations including full range of physical process including radiative and supernova feedback effects. This enables us to consider the full range of mass scales rather than assuming a single ionising efficiency for all halos. However, one large downside to this particular semi-numerical treatise is that the method is still fundamentally a single parameter model that only depends on the collapse mass fraction. There is no consideration of the environment that the sources live in, whether it is in a ionised region or not, and we take a relatively crude average over all halos in different environments to get a single efficiency coefficient. This may result in an improper weighting of $\zeta$. This is a problem that is well treated in contrast in full radiation hydrodynamics simulations, which is now starting to be computationally feasible at large scales [184].

A number of instruments will be coming online within the next several years to help put tighter constraints on models of reionisation. 21 cm interferometry performed by the Square Kilometer Array (SKA)[1] and the Hydrogen Epoch of Reionization Array (HERA)[2] will produce accurate mapping of the morphology of the reionisation process. Moreover, the James Webb Space Telescope should extend the current limits to the luminosity function of galaxies constraining parameters such as the stellar mass fraction. With these observations, we expect that our models can be utilized to study the onset of reionisation.

In this work, we extended the semi-numeric simulation code 21CMFAST to include a redshift-dependent minimum mass threshold for ionising source containing halos, $M_{\rm min}$, as well as a mass- and redshift-dependent ionising efficiency, $\zeta$. Our model produces reionisation histories that have subtle differences in comparison with

[1] http://www.skatelescope.org/
[2] http://reionization.org

the default model implemented in 21CMFAST while still being broadly consistent with the constraints from *Planck*. Moreover, we find significant differences in the bubble size distribution due to the presence of mini-halos which drive the characteristic scales down. We find that our model broadly constrains the minimum ionising efficiency contribution from galaxies while mini-halos only contribute near the beginning of reionisation, having no significant impact after z = 10.

# CHAPTER 5
# EFFICIENT IONIZATION IN MULTI-SCALE COSMOLOGICAL SIMULATIONS OF THE EPOCH OF REIONIZATION

## 5.1 Introduction

The Epoch of Reionization (EoR) is the final phase transition in the universe. As galaxies form during hierarchical structure formation, they host stars who emit starlight that ionizes the plasma pervading the universe in a highly non-linear fashion [For a review, see 10]. Thus, this particular process is an intimate coupling between light emitted by stellar sources and the large-scale intercluster medium. The massive dynamic range required to fully understand the process has made it a challenging problem in cosmology.

Initial attempts to understand the EoR were entirely analytic in nature [185, 150]. These works considered the ionization fraction of the universe as a continuous function balanced by the ionization and recombination rates into a single differential equation. These works were further extended to include halo mass dependence to consider the inhomogeneity of the sources [151, 152] but such extensions naturally led to the development of more computing-heavy methods. In a much more direct way, full hydrodynamical simulations were employed to resolve individual sources of photon emission in large boxes [153, 154, 184]. In order to get proper convergent histories of ionization, a minimum of 100 comoving $\mathrm{Mpc}^3$ box is required [155], and stellar sources are properly treated on parsec scales. This wide range of required scales has significantly hindered the use of cosmological simulations in the execution of fully consistent models.

A natural compromise between the two ends resulted in the development of semi-

numeric models. With the basic assumption that over-dense regions are the primary drivers of reionization, the ionization rate can be replaced by a single excursion set condition [156]. This can be understood as stating that if the number of photons available to ionize the region exceeds the number of baryons, the region must be ionized. This was initially implemented for complete three-dimensional realizations of cosmological initial conditions by Mesinger and Furlanetto [157] and Zahn *et al.* [158]. These models have the advantage of quickly being able to generate ioinization fields for large boxes at any given redshift in parallel, independent of one another. In particular, the code 21cmFAST [162] is an implementation that lends itself to be simply extended beyond the the single excursion set criterion. Sobacchi and Mesinger [178] considered the effect of inhomogeneous recombinations on the topology by calculating the self-consistent recombination rates at each given cell. Greig and Mesinger [163] used a Monte-Carlo scheme on top of the code to generate a best-fit range of parameters given the various constraints we have for the EoR. Koh and Wise [186] then extended the code to include the mass-dependence in the ionization efficiency parameter to explore the role of mini-halos and first dwarf galaxies on reionization. These works demonstrate 21cmFAST to be a capable tool to study the EoR.

In this work, we propose a novel method to tie in the results generated from semi-numeric codes in tandem with full hydrodynamical calculations to study the EoR. In the immediately following Section 5.2, we will describe the proposed method in detail along with the proof-of-concept plan. Then in Section 5.3, we will conclude by describing the potential applications of the proposed method.

## 5.2 Methods

The goal here is to generate ionization fields separately using a semi-numeric technique and then take the fields and couple them into a traditional hydro solver without turning on ray tracing. This should, with appropriate sampling of the ionization field

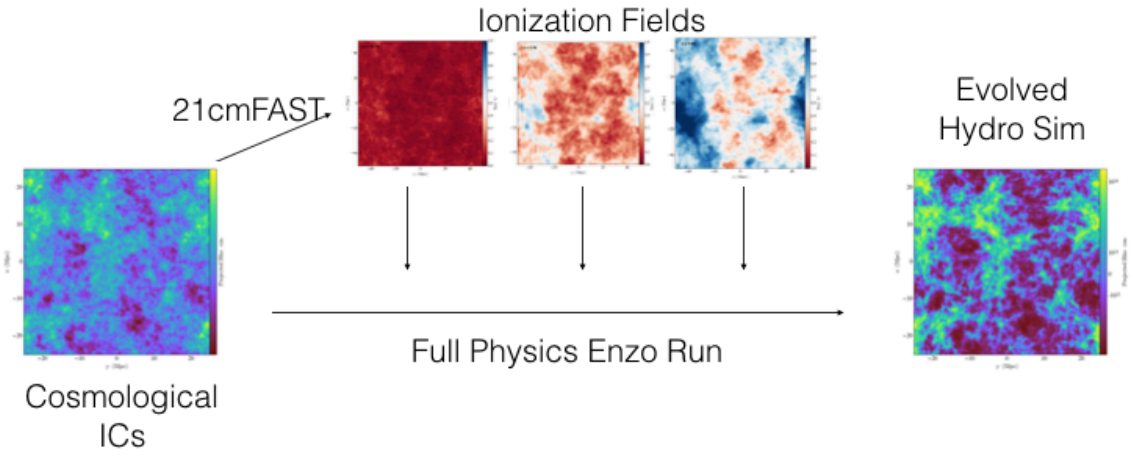


Figure 5.1: Overview schematic of the implementation of efficient ionization.

evolution, give largely consistent overall evolution of the system. Figure 5.1 shows an overview schematic detailing the process described.

### 5.2.1 Ionization Model

The first step is to produce an accurate set of cosmological initial conditions. We employ the MUSIC initial condition generator [104] using second-order Lagrangian perturbation theory to produce initial conditions in real-space and write them out to a file. We then extend the semi-numeric code 21cmFAST [162] to read in these initial conditions. The original code base generates initial conditions directly in k-space using first-order perturbation theory. The use of MUSIC enables a fluid transition between 21cmFAST and other cosmological hydrodynamics simulations which typically

require initial conditions to be inputted in real-space.

Furthermore, we use the modifications to 21cmFAST as detailed in [186]. As our simulations typically employ high-resolution to trace the formation of mini-halos, using this modification is important in generating the corresponding ionization maps. In order to accurately sample the time evolution of the ionization field, spatial data needs to outputted at a minimum of every 10 Myrs to match typical formation time-scales of Pop III stars. Moreover, the spatial resolution of the ionization field will be $2^3$ times the root grid resolution of the hydrodynamical simulations.

### 5.2.2 Coupling to Hydrodynamics

The next step is to couple in the ionization fields that are calculated in the previous section to hydrodynamic simulations. For our proof of concept, we use the cosmological simulation code Enzo [90]. From the generated ionization maps, we create a single spatial grid that stores the redshift at which the individual cells are ionized. This acts as a filter map through which an ionization background radiation can be triggered. Once the listed ionization redshift is reached, the cell is then considered ionized and we turn on the ionization background. As for the strength of this radiation, we use the ionization fields that are calculated in [187]. Since the grid cells in the hydrodynamical simulations can be of higher resolution than the ionization maps previously generated, we then employ nearest-neighbor interpolation to smooth out the high resolution details.

### 5.2.3 Proof-of-Concept

We will first produce a single simulation including radiative transfer as the base model to which we will compare the accuracy of our new method. This simulation will be a $(4\ \mathrm{Mpc})^3$ box focused on a single dwarf galaxy ($\mathrm{M} \simeq 10^9\ \mathrm{M}_\odot$) which we will run down to $\mathrm{z} = 10$. Our test case will be using our method on the same identical cosmological

initial conditions. We will compare the properties of the resulting most massive galaxy at the end of the simulation time at z = 10. We will tolerate errors that are introduced on the order of 5-10% which are comparable to the uncertainties that are inherent in astrophysical contexts. Larger discrepancies can be addressed by adjustments to the semi-numeric calculations which are comparably cheap in computation time.

## 5.3 Applications

There are two key applications to this implementation: (1) survey simulations and (2) zoom-in simulations. The former involves the simulation of a large sample volume from cosmological initial conditions. Because this implementation removes the need for the full radiative transfer module, we can then efficiently generate such large volumes while reaching high-spatial resolution comparable to the current state-of-the-art high redshift simulations.

Secondly, having a spatially-varying ionization map in place enhances zoom-in simulations which can often underestimate the outflow of radiation from regions outside of the region of interest. As the outside regions are not properly resolved, the sources that should be formed are never formed resulting in some inaccuracies at the outer ends of the Lagrangian volume. The preprocessing of the gas through ionization is required to accurately model the formation of present-day galaxies, which can significantly impact star formation rates.

The method proposed in this Chapter will lead to significant speed-up benefits in cosmological simulations. Radiative transfer modules can take up to 2/3rds of the total computation time in typical cosmological simulations. Therefore, in an idealistic scenario, this particular protocol can lead to an increased computational speedup of a factor of three. Once the proof-of-concept is demonstrated, we propose to release the modifications to the codes to the public. Both 21cmFAST and Enzo are available to the public using common version control software. We expect that the method

introduced will be widely used by community for the applications listed above.

# CHAPTER 6
# CONCLUSIONS AND FUTURE WORK

In this thesis, we explored the dynamics and role of mini-halos during the Epoch of Reionization. These are the fundamental building blocks which host the formation of the very first stars in the universe. Understanding the precise formation of these objects are essential to forming a consistent theory of galaxy formation. We will summarize the main conclusions and detail potential future extensions from our work in this chapter.

## 6.1 Summary of Thesis

In Chapter 2, we investigated the effect of the metallicity on the collapse dynamics of mini-halos. The main conclusions of this study are

- The effects of self-shielding are important in accurately treating the formation of stars in mini-halos.
- Metallicity has minimal impact on the minimum collapse mass of mini-halos below the critical metallicity between $10^3 Z_\odot < Z < 10^2 Z_\odot$. Once this critical metallicity is met, the minimum collapse mass drops down to $10^5 M_\odot$.

Then in Chapter 3, we investigated the amplification of magnetic fields in the early universe. This was done using a set of *ab-initio* simulations that followed the birth, main sequence, and death of a single Population III star with varying initial magnetic field strengths. The main conclusions of this study are

- Magnetic fields are primarily amplified by compression during the gravitational collapse prior to star formation, following the $B \sim \rho^{2/3}$ scaling.

- Magnetic fields are again amplified shortly following the supernova from the Pop III, but primarily through turbulent motions formed in the wake of the expanding blast wave.

- The magnitude of the amplification is largely independent of the strength of the initial background field. This implies that the peak field strength is strongly dependent on the initial field strength.

Then in Chapter 4, we explored the role of these primordial objects in reionizing the universe by extending an existing semi-numeric method to account for the mass-dependence of the ionizing efficiency. Thus, we were able to account for the role that mini-halos would have. The main conclusions of this study are

- Mini-halos can have significant impact during the start of the Epoch of Reionization, but are dwarfed by larger halos which began to dominate after $z > 10$.

- Mini-halos can also alter the ionization bubble topology as they form smaller H II regions.

Finally, in Chapter 5, we propose an application of our extension from the previous chapter to provide an efficient method of accurately generating ionization histories in cosmological simulations without the use of fully-resolved radiative transfer protocols. This implementation will enable the efficient generation of a large sample of cosmological simulations of the Epoch of Reionization. Furthermore, this can provide an accurate treatment of ionization effects from outside the target region in zoom-in cosmological simulations.

## 6.2 Future Work

We have explored the potential sites of the first-metal poor stars and the growth of magnetic fields in the first mini-halos that are formed during the Epoch of Reionization. The natural progression from this work is to push the ab-initio magnetic field

simulations from cosmological simulations to the formation of the first dwarf galaxy of mass, $M > 10^9 M_\odot$. This work can be limited to a zoom-in simulation centered about the most massive halo that will first reach this mass threshold. By incorporating magnetic fields, we can further trace the growth of magnetic fields which follows structure formation in parallel. As multiple supernovae blast waves collide, they can promote turbulence and lead to greater growth and dynamically significant field strengths. Then, we can study the impact these fields have on the formation of the subsequent generations of stars.

There are still lots of unanswered questions in the process of galaxy formation in the early universe. With the upcoming James Webb Space Telescope, Square Kilometer Array, and other next generation instrumentation, we will be able to probe further back into the Epoch of Reionization. Combined with the growing computing capacity and algorithms, such as the method proposed in Chapter 5, we will be ever closer to accurately studying this unique period in the universe.

## REFERENCES


[1] H. Poincaré, "The Milky Way and the Theory of Gases," *Pop. Astron.*, vol. 14, pp. 475–488, 1906.

[2] F. Zwicky, "Die Rotverschiebung von extragalaktischen Nebeln," *Helv. Phys. Acta*, vol. 6, pp. 110–127, 1933.

[3] V. C. Rubin, J. Burtley, A. Kiasatpoor, B. Klock, G. Pease, E. Rutscheidt, and C. Smith, "Kinematic studies of early-type stars. I. Photometric survey, space motions, and comparison with radio observations.," *ApJ*, vol. 67, p. 491, 1962.

[4] J. R. Bond, G. Efstathiou, and J. Silk, "Massive Neutrinos and the Large-Scale Structure of the Universe," *Phys. Rev. Lett.*, vol. 45, no. 24, pp. 1980–1984, 1980.

[5] S. D. M. White, M. Davis, and C. S. Frenk, "The size of clusters in a neutrino-dominated universe," *MNRAS*, vol. 209, no. 1, 27P–31P, 1984.

[6] M. Davis, G. Efstathiou, C. S. Frenk, and S. D. M. White, "The evolution of large-scale structure in a universe dominated by cold dark matter," *ApJ*, vol. 292, p. 371, 1985.

[7] A. G. Riess, A. V. Filippenko, P. Challis, A. Clocchiattia, A. Diercks, P. M. Garnavich, R. L. Gilliland, C. J. Hogan, S. Jha, R. P. Kirshner, B. Leibundgut, M. M. Phillips, D. Reiss, B. P. Schmidt, R. A. Schommer, R. C. Smith, J. Spyromilio, C. Stubbs, N. B. Suntzeff, and J. Tonry, "Observational Evidence from Supernovae for an Accelerating Universe and a Cosmological Constant," *ApJ*, vol. 116, no. 3, pp. 1009–1038, 1998. arXiv:`9805201 [astro-ph]`.

[8] S. Perlmutter, G. Aldering, G. Goldhaber, R. A. Knop, P. Nugent, P. G. Castro, S. Deustua, S. Fabbro, A. Goobar, D. E. Groom, I. M. Hook, A. G. Kim, M. Y. Kim, J. C. Lee, N. J. Nunes, R. Pain, C. R. Pennypacker, R. Quimby, C. Lidman, R. S. Ellis, M. Irwin, R. G. McMahon, P. Ruiz-Lapuente, N. Walton, B. Schaefer, B. J. Boyle, A. V. Filippenko, T. Matheson, A. S. Fruchter, N. Panagia, H. J. M. Newberg, W. J. Couch, and T. S. C. Project, "Measurements of Omega and Lambda from 42 High-Redshift Supernovae," *ApJ*, vol. 517, no. 2, pp. 565–586, 1999. arXiv:`9812133 [astro-ph]`.

[9] E. Hubble and Edwin, "A relation between distance and radial velocity among extra-galactic nebulae," *Proc. Natl. Acad. Sci.*, vol. 15, no. 3, pp. 168–173, 1929.

[10] J. H. Wise, "Introductory Review of Cosmic Reionization," *Contemp. Physics, Submitt.*, 2017.

[11] Y. B. Zeldovich and Y. B., "A Hypothesis, Unifying the Structure and the Entropy of the Universe," *MNRAS*, vol. 160, no. 1, 1P–3P, 1972.

[12] H. M. P. Couchman and M. J. Rees, "Pregalactic evolution in cosmologies with cold dark matter," *MNRAS*, vol. 221, no. 1, pp. 53–62, 1986.

[13] M. Tegmark, J. Silk, M. Rees, A. Blanchard, T. Abel, and F. Palla, "How small were the first cosmological objects?," *ApJ*, vol. 474, p. 1, 1997. arXiv:9603007 [astro-ph].

[14] S. P. Oh and Z. Haiman, "Second-Generation Objects in the Universe: Radiative Cooling and Collapse of Halos with Virial Temperatures Above 10^4 Kelvin," *ApJ*, vol. 569, no. 2, pp. 558–572, 2002. arXiv:0108071 [astro-ph].

[15] W. Saslaw and D. Zipoy, "Molecular Hydrogen in Pre-galactic Gas Clouds," *Nature*, vol. 216, no. 5119, pp. 976–978, 1967.

[16] P. J. E. Peebles and R. H. Dicke, "Origin of the Globular Star Clusters," *ApJ*, vol. 154, p. 891, 1968.

[17] S. Lepp and J. M. Shull, "Molecules in the early universe," *ApJ*, vol. 280, p. 465, 1984.

[18] T. Abel, P. Anninos, Y. Zhang, and M. L. Norman, "Modeling primordial gas in numerical cosmology," *New Astron.*, vol. 2, no. 3, pp. 181–207, 1997. arXiv:9608040 [astro-ph].

[19] Z. Haiman, A. A. Thoul, and A. Loeb, "Cosmological Formation of Low-Mass Objects," *ApJ*, vol. 464, p. 523, 1996. arXiv:9507111 [astro-ph].

[20] N. Yoshida, T. Abel, L. Hernquist, and N. Sugiyama, "Simulations of Early Structure Formation: Primordial Gas Clouds," *ApJ*, vol. 592, no. 2, pp. 645–663, 2003. arXiv:0301645 [astro-ph].

[21] T. Abel, G. L. Bryan, and M. L. Norman, "The Formation of the First Star in the Universe," *Science*, vol. 295, no. 5552, pp. 93–98, 2002.

[22] V. Bromm and C. J. Clarke, "The Formation of the First Globular Clusters in Dwarf Galaxies before the Epoch of Reionization," *ApJ*, vol. 566, no. 1, pp. L1–L4, 2002. arXiv:0201066 [astro-ph].

[23] A. Whitworth and D. Summers, "Self-similar condensation of spherically symmetric self-gravitating isothermal gas clouds," *MNRAS*, vol. 214, no. 1, pp. 1–25, 1985.

[24] K. Omukai and R. Nishi, "Formation of Primordial Protostars," *ApJ*, vol. 508, no. 1, pp. 141–150, 1998. arXiv:9811308 [astro-ph].

[25] R. B. Larson and R. B., "Numerical Calculations of the Dynamics of a Collapsing Proto-Star*," *MNRAS*, vol. 145, no. 3, pp. 271–295, 1969.

[26] M. V. Penston and M. V., "Dynamics of Self-Gravitating Gaseous Spheres–II: Collapses of Gas Spheres with Cooling and the Behaviour of Polytropic Gas Spheres," *MNRAS*, vol. 145, no. 4, pp. 457–485, 1969.

[27] K. Omukai and F. Palla, "On the Formation of Massive Primordial Stars," *ApJ*, vol. 561, no. 1, pp. L55–L58, 2001.

[28] K. Omukai and F. Palla, "Formation of the First Stars by Accretion," *ApJ*, vol. 589, no. 2, pp. 677–687, 2003. arXiv:0302345 [astro-ph].

[29] M. J. Turk, T. Abel, and B. O'Shea, "The formation of Population III binaries from cosmological initial conditions.," *Science*, vol. 325, no. 5940, pp. 601–5, 2009.

[30] P. C. Clark, S. C. O. Glover, R. J. Smith, T. H. Greif, R. S. Klessen, and V. Bromm, "The formation and fragmentation of disks around primordial protostars.," *Science*, vol. 331, no. 6020, pp. 1040–2, 2011.

[31] T. H. Greif, V. Bromm, P. C. Clark, S. C. O. Glover, R. J. Smith, R. S. Klessen, N. Yoshida, and V. Springel, "Formation and evolution of primordial protostellar systems," *MNRAS*, vol. 424, no. 1, pp. 399–415, 2012.

[32] S. C. O. Glover and P. W. J. L. Brand, "On the photodissociation of H2 by the first stars," *MNRAS*, vol. 321, no. 3, pp. 385–397, 2001. arXiv:0005576 [astro-ph].

[33] M. E. Machacek, G. L. Bryan, and T. Abel, "Simulations of Pregalactic Structure Formation with Radiative Feedback," *ApJ*, vol. 548, no. 2, pp. 509–521, 2001.

[34] B. T. Draine and F. Bertoldi, "Structure of Stationary Photodissociation Fronts," *ApJ*, vol. 468, p. 269, 1996. arXiv:9603032 [astro-ph].

[35] J. Wolcott-Green, Z. Haiman, and G. L. Bryan, "Photodissociation of H2 in protogalaxies: modelling self-shielding in three-dimensional simulations," *MNRAS*, vol. 418, no. 2, pp. 838–852, 2011. arXiv:1106.3523.

[36] J. H. Wise and T. Abel, "Resolving the Formation of Protogalaxies. III. Feedback from the First Stars," *ApJ*, vol. 685, no. 1, pp. 40–56, 2008.

[37] D. Whalen, T. Abel, and M. L. Norman, "Radiation Hydrodynamic Evolution of Primordial H ii Regions," *ApJ*, vol. 610, no. 1, pp. 14–22, 2004.

[38] T. Kitayama, N. Yoshida, H. Susa, and M. Umemura, "The Structure and Evolution of Early Cosmological H ii Regions," *ApJ*, vol. 613, no. 2, pp. 631–645, 2004.

[39] M. A. Alvarez, V. Bromm, and P. R. Shapiro, "The H ii Region of the First Star," *ApJ*, vol. 639, no. 2, pp. 621–632, 2006.

[40] T. Abel, J. H. Wise, and G. L. Bryan, "The H II Region of a Primordial Star," *ApJ*, vol. 659, no. 2, pp. L87–L90, 2007. arXiv:0606019 [astro-ph].

[41] S. Hirano, T. Hosokawa, N. Yoshida, K. Omukai, and H. W. Yorke, "Primordial star formation under the influence of far ultraviolet radiation: 1540 cosmological haloes and the stellar mass distribution," *MNRAS*, vol. 448, no. 1, pp. 568–587, 2015.

[42] S. E. Woosley and T. A. Weaver, "The Evolution and Explosion of Massive Stars. II. Explosive Hydrodynamics and Nucleosynthesis," *ApJS*, vol. 101, p. 181, 1995.

[43] A. Heger and S. E. Woosley, "The Nucleosynthetic Signature of Population III," *ApJ*, vol. 567, no. 1, pp. 532–543, 2002.

[44] T. Kitayama and N. Yoshida, "Supernova Explosions in the Early Universe: Evolution of Radiative Remnants and the Halo Destruction Efficiency," *ApJ*, vol. 630, no. 2, pp. 675–688, 2005.

[45] T. H. Greif, J. L. Johnson, V. Bromm, and R. S. Klessen, "The First Supernova Explosions: Energetics, Feedback, and Chemical Enrichment," *ApJ*, vol. 670, no. 1, pp. 1–14, 2007.

[46] D. Whalen, B. van Veelen, B. W. O'Shea, and M. L. Norman, "The Destruction of Cosmological Minihalos by Primordial Supernovae," *ApJ*, vol. 682, no. 1, pp. 49–67, 2008. arXiv:0801.3698.

[47] V. Bromm, P. S. Coppi, and R. B. Larson, "Forming the First Stars in the Universe: The Fragmentation of Primordial Gas," *ApJ*, vol. 527, no. 1, pp. L5–L8, 1999. arXiv:9910224 [astro-ph].

[48] T. Abel, G. L. Bryan, and M. L. Norman, "The Formation and Fragmentation of Primordial Molecular Clouds," *ApJ*, vol. 540, no. 1, pp. 39–44, 2000. arXiv:0002135 [astro-ph].

[49] B. D. Smith, J. H. Wise, B. W. O'Shea, M. L. Norman, and S. Khochfar, "The first Population II stars formed in externally enriched mini-haloes," *MNRAS*, vol. 452, no. 3, pp. 2822–2836, 2015.

[50] M. Jeon, A. H. Pawlik, V. Bromm, and M. Milosavljevic, "Recovery from population III supernova explosions and the onset of second generation star formation," *MNRAS*, vol. 444, no. 4, pp. 3288–3300, 2014. arXiv:1407.0034.

[51] A. Frebel, J. L. Johnson, and V. Bromm, "Probing the Formation of the First Low-Mass Stars with Stellar Archaeology," *MNRAS*, vol. 380, no. 1, pp. L40–L44, 2007. arXiv:0701395 [astro-ph].

[52] S. Salvadori, A. Skuladottir, and E. Tolstoy, "Carbon-enhanced metal-poor stars in dwarf galaxies," *MNRAS*, vol. 454, no. 2, pp. 1320–1331, 2015. arXiv:1506.03451.

[53] E. N. Kirby, J. D. Simon, M. Geha, P. Guhathakurta, and A. Frebel, "Uncovering Extremely Metal-Poor Stars in the Milky Way's Ultra-Faint Dwarf Spheroidal Satellite Galaxies," *Astrophys. J. Lett.*, vol. 685, no. 1, 2008. arXiv:0807.1925.

[54] R. Zinn, "The globular cluster system of the galaxy. IV - The halo and disk subsystems," *ApJ*, vol. 293, p. 424, 1985.

[55] M. A. Beasley, C. M. Baugh, D. A. Forbes, R. M. Sharples, and C. S. Frenk, "On the formation of globular cluster systems in a hierarchical Universe," *MNRAS*, vol. 333, no. 2, pp. 383–399, 2002. arXiv:0202191 [astro-ph].

[56] B. Strömgren and Bengt, "The Physical State of Interstellar Hydrogen.," *ApJ*, vol. 89, p. 526, 1939.

[57] N. Kashikawa, Y. Ishizaki, C. J. Willott, M. Onoue, M. Im, H. Furusawa, J. Toshikawa, S. Ishikawa, Y. Niino, K. Shimasaku, M. Ouchi, and P. Hibon,

"The Subaru high-z quasar survey: discovery of faint z˜6 quasars," *ApJ*, vol. 798, no. 1, 2015. arXiv:1410.7401.

[58] Planck Collaboration, R. Adam, N. Aghanim, M. Ashdown, J. Aumont, C. Baccigalupi, M. Ballardini, A. J. Banday, R. B. Barreiro, N. Bartolo, S. Basak, R. Battye, K. Benabed, J. P. Bernard, M. Bersanelli, P. Bielewicz, J. J. Bock, A. Bonaldi, L. Bonavera, J. R. Bond, J. Borrill, F. R. Bouchet, M. Bucher, C. Burigana, E. Calabrese, J. F. Cardoso, J. Carron, H. C. Chiang, L. P. L. Colombo, C. Combet, B. Comis, A. Coulais, B. P. Crill, A. Curto, F. Cuttaia, R. J. Davis, P. de Bernardis, A. de Rosa, G. de Zotti, J. Delabrouille, E. Di Valentino, C. Dickinson, J. M. Diego, O. Doré, M. Douspis, A. Ducout, X. Dupac, F. Elsner, T. A. Enßlin, H. K. Eriksen, E. Falgarone, Y. Fantaye, F. Finelli, F. Forastieri, M. Frailis, A. A. Fraisse, E. Franceschi, A. Frolov, S. Galeotta, S. Galli, K. Ganga, R. T. Génova-Santos, M. Gerbino, T. Ghosh, J. González-Nuevo, K. M. Górski, A. Gruppuso, J. E. Gudmundsson, F. K. Hansen, G. Helou, S. Henrot-Versillé, D. Herranz, E. Hivon, Z. Huang, S. Ili_, A. H. Jaffe, W. C. Jones, E. Keihänen, R. Keskitalo, T. S. Kisner, L. Knox, N. Krachmalnicoff, M. Kunz, H. Kurki-Suonio, G. Lagache, A. Lähteenmäki, J. M. Lamarre, M. Langer, A. Lasenby, M. Lattanzi, C. R. Lawrence, M. L. Jeune, F. Levrier, A. Lewis, M. Liguori, P. B. Lilje, M. López-Caniego, Y. Z. Ma, J. F. Macías-Pérez, G. Maggio, A. Mangilli, M. Maris, P. G. Martin, E. Martínez-González, S. Matarrese, N. Mauri, J. D. McEwen, P. R. Meinhold, A. Melchiorri, A. Mennella, M. Migliaccio, M. A. Miville-Deschênes, D. Molinari, A. Moneti, L. Montier, G. Morgante, A. Moss, P. Naselsky, P. Natoli, C. A. Oxborrow, L. Pagano, D. Paoletti, B. Partridge, G. Patanchon, L. Patrizii, O. Perdereau, L. Perotto, V. Pettorino, F. Piacentini, S. Plaszczynski, L. Polastri, G. Polenta, J. L. Puget, J. P. Rachen, B. Racine, M. Reinecke, M. Remazeilles, A. Renzi, G. Rocha, M. Rossetti, G. Roudier, J. A. Rubiño-Martín, B. Ruiz-Granados, L. Salvati, M. Sandri, M. Savelainen, D. Scott, G. Sirri, R. Sunyaev, A. S. Suur-Uski, J. A. Tauber, M. Tenti, L. Toffolatti, M. Tomasi, M. Tristram, T. Trombetti, J. Valiviita, F. Van Tent, P. Vielva, F. Villa, N. Vittorio, B. D. Wandelt, I. K. Wehus, M. White, A. Zacchei, and A. Zonca, *Planck 2016 intermediate results. XLVII. Planck constraints on reionization history*, 2016. arXiv:1605.03507.

[59] Planck Collaboration, N. Aghanim, M. Ashdown, J. Aumont, C. Baccigalupi, M. Ballardini, A. J. Banday, R. B. Barreiro, N. Bartolo, S. Basak, R. Battye, K. Benabed, J. P. Bernard, M. Bersanelli, P. Bielewicz, J. J. Bock, A. Bonaldi, L. Bonavera, J. R. Bond, J. Borrill, F. R. Bouchet, F. Boulanger, M. Bucher, C. Burigana, R. C. Butler, E. Calabrese, J. F. Cardoso, J. Carron, A. Challinor, H. C. Chiang, L. P. L. Colombo, C. Combet, B. Comis, A. Coulais, B. P. Crill, A. Curto, F. Cuttaia, R. J. Davis, P. de Bernardis, A. de Rosa, G. de Zotti, J. Delabrouille, J. M. Delouis, E. Di Valentino, C. Dickinson, J. M. Diego, O. Doré, M. Douspis, A. Ducout, X. Dupac, G. Efstathiou, F. Elsner, T. A. Enßlin, H. K. Eriksen, E. Falgarone, Y. Fantaye, F. Finelli, F. Forastieri, M. Frailis,

A. A. Fraisse, E. Franceschi, A. Frolov, S. Galeotta, S. Galli, K. Ganga, R. T. Génova-Santos, M. Gerbino, T. Ghosh, J. González-Nuevo, K. M. Górski, S. Gratton, A. Gruppuso, J. E. Gudmundsson, F. K. Hansen, G. Helou, S. Henrot-Versillé, D. Herranz, E. Hivon, Z. Huang, S. Ilic, A. H. Jaffe, W. C. Jones, E. Keihänen, R. Keskitalo, T. S. Kisner, L. Knox, N. Krachmalnicoff, M. Kunz, H. Kurki-Suonio, G. Lagache, J. M. Lamarre, M. Langer, A. Lasenby, M. Lattanzi, C. R. Lawrence, M. L. Jeune, J. P. Leahy, F. Levrier, M. Liguori, P. B. Lilje, M. López-Caniego, Y. Z. Ma, J. F. Macías-Pérez, G. Maggio, A. Mangilli, M. Maris, P. G. Martin, E. Martínez-González, S. Matarrese, N. Mauri, J. D. McEwen, P. R. Meinhold, A. Melchiorri, A. Mennella, M. Migliaccio, M. A. Miville-Deschênes, D. Molinari, A. Moneti, L. Montier, G. Morgante, A. Moss, S. Mottet, P. Naselsky, P. Natoli, C. A. Oxborrow, L. Pagano, D. Paoletti, B. Partridge, G. Patanchon, L. Patrizii, O. Perdereau, L. Perotto, V. Pettorino, F. Piacentini, S. Plaszczynski, L. Polastri, G. Polenta, J. L. Puget, J. P. Rachen, B. Racine, M. Reinecke, M. Remazeilles, A. Renzi, G. Rocha, M. Rossetti, G. Roudier, J. A. Rubiño-Martín, B. Ruiz-Granados, L. Salvati, M. Sandri, M. Savelainen, D. Scott, G. Sirri, R. Sunyaev, A. S. Suur-Uski, J. A. Tauber, M. Tenti, L. Toffolatti, M. Tomasi, M. Tristram, T. Trombetti, J. Valiviita, F. Van Tent, L. Vibert, P. Vielva, F. Villa, N. Vittorio, B. D. Wandelt, R. Watson, I. K. Wehus, M. White, A. Zacchei, and A. Zonca, *Planck intermediate results. XLVI. Reduction of large-scale systematic effects in HFI polarization maps and estimation of the reionization optical depth*, 2016. arXiv:1605.02985.

[60] X. Fan, M. A. Strauss, R. H. Becker, R. L. White, J. E. Gunn, G. R. Knapp, G. T. Richards, D. P. Schneider, J. Brinkmann, and M. Fukugita, "Constraining the Evolution of the Ionizing Background and the Epoch of Reionization with z ˜ 6 Quasars. II. A Sample of 19 Quasars," *ApJ*, vol. 132, no. 1, pp. 117–136, 2006.

[61] J. E. Gunn and B. A. Peterson, "On the Density of Neutral Hydrogen in Intergalactic Space.," *ApJ*, vol. 142, p. 1633, 1965.

[62] D. Scott and M. J. Rees, "The 21-cm line at high redshift: a diagnostic for the origin of large scale structure," *MNRAS*, vol. 247, p. 510, 1990.

[63] K. S. S. Barrow, J. H. Wise, M. L. Norman, B. W. O'Shea, and H. Xu, "First Light: Exploring the Spectra of High-Redshift Galaxies in the Renaissance Simulations," *eprint arXiv:1701.02749*, 2017. arXiv:1701.02749.

[64] A. R. Neben, R. F. Bradley, J. N. Hewitt, D. R. DeBoer, A. R. Parsons, J. E. Aguirre, Z. S. Ali, C. Cheng, A. Ewall-Wice, N. Patra, N. Thyagarajan, J. Bowman, R. Dickenson, J. S. Dillon, P. Doolittle, D. Egan, M. Hedrick, D. C. Jacobs, S. A. Kohn, P. J. Klima, K. Moodley, B. R. B. Saliwanchik, P. Schaffner, J. Shelton, H. A. Taylor, R. Taylor, M. Tegmark, B. Wirt, and H. Zheng, "The

Hydrogen Epoch of Reionization Array Dish I: Beam Pattern Measurements and Science Implications," *ApJ*, vol. 826, no. 2, 2016. arXiv:1602.03887.

[65] L. V. E. Koopmans, J. Pritchard, G. Mellema, F. Abdalla, J. Aguirre, K. Ahn, R. Barkana, I. van Bemmel, G. Bernardi, A. Bonaldi, F. Briggs, A. G. de Bruyn, T. C. Chang, E. Chapman, X. Chen, B. Ciardi, K. K. Datta, P. Dayal, A. Ferrara, A. Fialkov, F. Fiore, K. Ichiki, I. T. Illiev, S. Inoue, V. Jelić, M. Jones, J. Lazio, U. Maio, S. Majumdar, K. J. Mack, A. Mesinger, M. F. Morales, A. Parsons, U. L. Pen, M. Santos, R. Schneider, B. Semelin, R. S. de Souza, R. Subrahmanyan, T. Takeuchi, C. Trott, H. Vedantham, J. Wagg, R. Webster, and S. Wyithe, "The Cosmic Dawn and Epoch of Reionization with the Square Kilometre Array," *Proc. Adv. Astrophys. with Sq. Km. Array*, 2015. arXiv:1505.07568.

[66] P. P. Kronberg, "Extragalactic magnetic fields," *Reports Prog. Phys.*, vol. 57, no. 4, pp. 325–382, 1994.

[67] R. Beck, M. Ehle, V. Shoutenkov, A. Shukurov, and D. Sokoloff, "Magnetic field as a tracer of sheared gas flow in barred galaxies," *Nature*, vol. 397, no. 6717, pp. 324–327, 1999.

[68] R. Beck, "Galactic and extragalactic magnetic fields a concise review," *Astrophys. Sp. Sci. Trans.*, vol. 5, no. 1, pp. 43–47, 2009.

[69] M. R. Krumholz and M. R., "Notes on Star Formation," *eprint arXiv:1511.03457*, 2015. arXiv:1511.03457.

[70] L. M. Widrow and L. M., "Origin of galactic and extragalactic magnetic fields," *Rev. Mod. Phys.*, vol. 74, no. 3, pp. 775–823, 2002. arXiv:0207240 [astro-ph].

[71] D. Boyanovsky and D., "Phase transitions in the early and the present Universe: from the big bang to heavy ion collisions," *Proc. NATO Adv. Study Inst. Phase Transitions Early Universe*, p. 3, 2001. arXiv:0102120 [hep-ph].

[72] C. J. Hogan, "Magnetohydrodynamic Effects of a First-Order Cosmological Phase Transition," *Phys. Rev. Lett.*, vol. 51, no. 16, pp. 1488–1491, 1983.

[73] J. M. Quashnock, A. Loeb, and D. N. Spergel, "Magnetic field generation during the cosmological QCD phase transition," *ApJ*, vol. 344, p. L49, 1989.

[74] G. Sigl, A. V. Olinto, and K. Jedamzik, "Primordial magnetic fields from cosmological first order phase transitions," *Phys. Rev. D*, vol. 55, no. 8, pp. 4582–4590, 1997.

[75] B. Ratra, "Cosmological 'seed' magnetic field from inflation," *ApJ*, vol. 391, p. L1, 1992.

[76] A. Kandus, E. A. Calzetta, F. D. Mazzitelli, and C. E. M. Wagner, "Cosmological Magnetic Fields from Gauge-Mediated Supersymmetry-Breaking Models," *Phys. Lett. B*, vol. 472, no. 3-4, pp. 287–294, 2000. arXiv:9908524 [hep-ph].

[77] R. M. Kulsrud and R. M., *Plasma physics for astrophysics*. 2005.

[78] L. Biermann, "Über den Ursprung der Magnetfelder auf Sternen und im interstellaren Raum," *Zeitschrift Für Naturforsch.*, vol. 5a, pp. 65–71, 1950.

[79] H. Xu, B. W. O'Shea, D. C. Collins, M. L. Norman, H. Li, and S. Li, "The Biermann Battery in Cosmological MHD Simulations of Population III Star Formation," *ApJ*, vol. 688, no. 2, pp. L57–L60, 2008.

[80] G. S. Bisnovatyi-Kogan, A. A. Ruzmaikin, and R. A. Syunyaev, "Star Contraction and Magnetic-Field Generation in Protogalaxies.," *Sov. Astron.*, vol. 17, p. 137, 1973.

[81] R. E. Pudritz and J. Silk, "The origin of magnetic fields and primordial stars in protogalaxies," *ApJ*, vol. 342, p. 650, 1989.

[82] R. R. Mellon and Z.-Y. Li, "Magnetic Braking and Protostellar Disk Formation: The Ideal MHD Limit," *ApJ*, vol. 681, no. 2, 2008. arXiv:0709.0445.

[83] M. N. Machida and K. Doi, "The formation of Population III stars in gas accretion stage: effects of magnetic fields," *MNRAS*, vol. 435, no. 4, pp. 3283–3305, 2013. arXiv:1308.2754.

[84] Planck Collaboration, P. A. R. Ade, N. Aghanim, M. Arnaud, F. Arroja, M. Ashdown, J. Aumont, C. Baccigalupi, M. Ballardini, A. J. Banday, R. B. Barreiro, N. Bartolo, E. Battaner, K. Benabed, A. Benoît, A. Benoit-Lévy, J. P. Bernard, M. Bersanelli, P. Bielewicz, J. J. Bock, A. Bonaldi, L. Bonavera, J. R. Bond, J. Borrill, F. R. Bouchet, M. Bucher, C. Burigana, R. C. Butler, E. Calabrese, J. F. Cardoso, A. Catalano, A. Chamballu, H. C. Chiang, J. Chluba, P. R. Christensen, S. Church, D. L. Clements, S. Colombi, L. P. L. Colombo, C. Combet, F. Couchot, A. Coulais, B. P. Crill, A. Curto, F. Cuttaia, L. Danese, R. D. Davies, R. J. Davis, P. de Bernardis, A. de Rosa, G. de Zotti, J. Delabrouille, F. X. Désert, J. M. Diego, K. Dolag, H. Dole, S. Donzelli, O. Doré, M. Douspis, A. Ducout, X. Dupac, G. Efstathiou, F. Elsner, T. A. Enßlin, H. K. Eriksen, J. Fergusson, F. Finelli, E. Florido, O. Forni, M. Frailis, A. A. Fraisse, E. Franceschi, A. Frejsel, S. Galeotta, S. Galli, K. Ganga, M. Giard, Y. Giraud-Héraud, E. Gjerløw, J. González-Nuevo, K. M. Górski, S. Gratton, A. Gregorio, A. Gruppuso, J. E. Gudmundsson, F. K. Hansen, D. Hanson, D. L. Harrison,

G. Helou, S. Henrot-Versillé, C. Hernández-Monteagudo, D. Herranz, S. R. Hildebrandt, E. Hivon, M. Hobson, W. A. Holmes, A. Hornstrup, W. Hovest, K. M. Huffenberger, G. Hurier, A. H. Jaffe, T. R. Jaffe, W. C. Jones, M. Juvela, E. Keihänen, R. Keskitalo, J. Kim, T. S. Kisner, J. Knoche, M. Kunz, H. Kurki-Suonio, G. Lagache, A. Lähteenmäki, J. M. Lamarre, A. Lasenby, M. Lattanzi, C. R. Lawrence, J. P. Leahy, R. Leonardi, J. Lesgourgues, F. Levrier, M. Liguori, P. B. Lilje, M. Linden-Vørnle, M. López-Caniego, P. M. Lubin, J. F. Macías-Pérez, G. Maggio, D. Maino, N. Mandolesi, A. Mangilli, M. Maris, P. G. Martin, E. Martínez-González, S. Masi, S. Matarrese, P. McGehee, P. R. Meinhold, A. Melchiorri, L. Mendes, A. Mennella, M. Migliaccio, S. Mitra, M. A. Miville-Deschênes, D. Molinari, A. Moneti, L. Montier, G. Morgante, D. Mortlock, A. Moss, D. Munshi, J. A. Murphy, P. Naselsky, F. Nati, P. Natoli, C. B. Netterfield, H. U. Nørgaard-Nielsen, F. Noviello, D. Novikov, I. Novikov, N. Oppermann, C. A. Oxborrow, F. Paci, L. Pagano, F. Pajot, D. Paoletti, F. Pasian, G. Patanchon, O. Perdereau, L. Perotto, F. Perrotta, V. Pettorino, F. Piacentini, M. Piat, E. Pierpaoli, D. Pietrobon, S. Plaszczynski, E. Pointecouteau, G. Polenta, L. Popa, G. W. Pratt, G. Prézeau, S. Prunet, J. L. Puget, J. P. Rachen, R. Rebolo, M. Reinecke, M. Remazeilles, C. Renault, A. Renzi, I. Ristorcelli, G. Rocha, C. Rosset, M. Rossetti, G. Roudier, J. A. Rubiño-Martín, B. Ruiz-Granados, B. Rusholme, M. Sandri, D. Santos, M. Savelainen, G. Savini, D. Scott, M. D. Seiffert, E. P. S. Shellard, M. Shiraishi, L. D. Spencer, V. Stolyarov, R. Stompor, R. Sudiwala, R. Sunyaev, D. Sutton, A. S. Suur-Uski, J. F. Sygnet, J. A. Tauber, L. Terenzi, L. Toffolatti, M. Tomasi, M. Tristram, M. Tucci, J. Tuovinen, G. Umana, L. Valenziano, J. Valiviita, B. Van Tent, P. Vielva, F. Villa, L. A. Wade, B. D. Wandelt, I. K. Wehus, D. Yvon, A. Zacchei, and A. Zonca, "Planck 2015 results. XIX. Constraints on primordial magnetic fields," p. 29, 2015. arXiv:1502.01594.

[85] R. Beck, A. Brandenburg, D. Moss, A. Shukurov, and D. Sokoloff, "GALACTIC MAGNETISM: Recent Developments and Perspectives," *ARA&A*, vol. 34, no. 1, pp. 155–206, 1996.

[86] A. A. Ruzmaikin, A. M. Shukurov, and D. D. Sokoloff, *Magnetic Fields of Galaxies*, ser. Astrophysics and Space Science Library. Dordrecht: Springer Netherlands, 1988, vol. 133, ISBN: 978-94-010-7776-7.

[87] A. Kazantsev, "ENHANCEMENT OF A MAGNETIC FIELD BY A CONDUCTING FLUID," *Sov. Phys. JETP*, vol. 26, no. 53, pp. 1806–1813, 1968.

[88] S. Sur, D. R. G. Schleicher, R. Banerjee, C. Federrath, and R. S. Klessen, "THE GENERATION OF STRONG MAGNETIC FIELDS DURING THE FORMATION OF THE FIRST STARS," *ApJ*, vol. 721, no. 2, pp. L134–L138, 2010.

[89] J. Schober, D. Schleicher, C. Federrath, S. Glover, R. S. Klessen, and R. Banerjee, "THE SMALL-SCALE DYNAMO AND NON-IDEAL MAGNETOHYDRODYNAMICS IN PRIMORDIAL STAR FORMATION," *ApJ*, vol. 754, no. 2, p. 99, 2012.

[90] G. L. Bryan, M. L. Norman, B. W. O'Shea, T. Abel, J. H. Wise, M. J. Turk, D. R. Reynolds, D. C. Collins, P. Wang, S. W. Skillman, B. Smith, R. P. Harkness, J. Bordner, J.-h. Kim, M. Kuhlen, H. Xu, N. Goldbaum, C. Hummels, A. G. Kritsuk, E. Tasker, S. Skory, C. M. Simpson, O. Hahn, J. S. Oishi, G. C. So, F. Zhao, R. Cen, and Y. Li, "ENZO: AN ADAPTIVE MESH REFINEMENT CODE FOR ASTROPHYSICS," *ApJS*, vol. 211, no. 2, p. 19, 2014.

[91] A. Dekel and M. J. Rees, "Physical mechanisms for biased galaxy formation," *Nat. (ISSN 0028-0836)*, vol. 326, no. 6112, pp. 455–462, 1987.

[92] Z. Haiman, T. Abel, and M. J. Rees, "The Radiative Feedback of the First Cosmological Objects," *ApJ*, vol. 534, no. 1, pp. 11–24, 2000. arXiv:9903336 [astro-ph].

[93] F. Haardt and P. Madau, "Radiative Transfer in a Clumpy Universe: II. The Utraviolet Extragalactic Background," *ApJ*, vol. 461, p. 20, 1996. arXiv:9509093 [astro-ph].

[94] S. C. O. Glover and M. M. Mac Low, "Simulating the formation of molecular clouds. I. Slow formation by gravitational collapse from static initial conditions," *ApJS*, vol. 169, no. 2, pp. 239–268, 2007. arXiv:0605120 [astro-ph].

[95] T. Hartwig, S. C. O. Glover, R. S. Klessen, M. A. Latif, and M. Volonteri, "How an improved implementation of H2 self-shielding influences the formation of massive stars and black holes," *MNRAS*, vol. 452, no. 2, pp. 1233–1244, 2015. arXiv:1505.00263.

[96] A. Heger and S. E. Woosley, "Nucleosynthesis and Evolution of Massive Metal-Free Stars," *ApJ*, vol. 724, no. 1, pp. 341–373, 2010. arXiv:0803.3161.

[97] J. H. Wise, M. J. Turk, M. L. Norman, and T. Abel, "THE BIRTH OF A GALAXY: PRIMORDIAL METAL ENRICHMENT AND STELLAR POPULATIONS," *ApJ*, vol. 745, no. 1, p. 50, 2012.

[98] C. Safranek-Shrader, M. Milosavljevic, and V. Bromm, "Star formation in the first galaxies - II. Clustered star formation and the influence of metal line cooling," *MNRAS*, vol. -1, p. 19, 2014. arXiv:1307.1982.

[99] K. Omukai, "Primordial Star Formation under Far-ultraviolet radiation," *ApJ*, vol. 546, no. 2, pp. 635–651, 2000. arXiv:0011446 [astro-ph].

[100] V. Bromm, R. P. Kudritzki, and A. Loeb, "Generic Spectrum and Ionization Efficiency of a Heavy Initial Mass Function for the First Stars," *ApJ*, vol. 552, no. 2, pp. 464–472, 2001.

[101] V. Bromm and A. Loeb, "The Formation of the First Low-Mass Stars From Gas With Low Carbon and Oxygen Abundances," *Nature*, vol. 425, no. 6960, pp. 812–814, 2003. arXiv:0310622 [astro-ph].

[102] S. C. O. Glover and T. Abel, "Uncertainties in H 2 and HD chemistry and cooling and their role in early structure formation," *MNRAS*, vol. 388, no. 4, pp. 1627–1651, 2008. arXiv:0803.1768.

[103] J. K. Truelove, R. I. Klein, C. F. McKee, J. H. Holliman II, L. H. Howell, and J. A. Greenough, "The Jeans Condition: A New Constraint on Spatial Resolution in Simulations of Isothermal Self-gravitational Hydrodynamics," *ApJ*, vol. 489, no. 2, pp. L179–L183, 1997.

[104] O. Hahn and T. Abel, "Multi-scale initial conditions for cosmological simulations," *MNRAS*, vol. 415, no. 3, pp. 2101–2121, 2011. arXiv:1103.6031.

[105] P. Planck Collaboration, P. A. R. Ade, N. Aghanim, M. Arnaud, M. Ashdown, J. Aumont, C. Baccigalupi, A. J. Banday, R. B. Barreiro, J. G. Bartlett, N. Bartolo, E. Battaner, R. Battye, K. Benabed, A. Benoit, A. Benoit-Levy, J. P. Bernard, M. Bersanelli, P. Bielewicz, J. J. Bock, A. Bonaldi, L. Bonavera, J. R. Bond, J. Borrill, F. R. Bouchet, F. Boulanger, M. Bucher, C. Burigana, R. C. Butler, E. Calabrese, J. F. Cardoso, A. Catalano, A. Challinor, A. Chamballu, R. R. Chary, H. C. Chiang, J. Chluba, P. R. Christensen, S. Church, D. L. Clements, S. Colombi, L. P. L. Colombo, C. Combet, A. Coulais, B. P. Crill, A. Curto, F. Cuttaia, L. Danese, R. D. Davies, R. J. Davis, P. de Bernardis, A. de Rosa, G. de Zotti, J. Delabrouille, F. X. Desert, E. Di Valentino, C. Dickinson, J. M. Diego, K. Dolag, H. Dole, S. Donzelli, O. Dore, M. Douspis, A. Ducout, J. Dunkley, X. Dupac, G. Efstathiou, F. Elsner, T. A. Ensslin, H. K. Eriksen, M. Farhang, J. Fergusson, F. Finelli, O. Forni, M. Frailis, A. A. Fraisse, E. Franceschi, A. Frejsel, S. Galeotta, S. Galli, K. Ganga, C. Gauthier, M. Gerbino, T. Ghosh, M. Giard, Y. Giraud-Heraud, E. Giusarma, E. Gjerlow, J. Gonzalez-Nuevo, K. M. Gorski, S. Gratton, A. Gregorio, A. Gruppuso, J. E. Gudmundsson, J. Hamann, F. K. Hansen, D. Hanson, D. L. Harrison, G. Helou, S. Henrot-Versille, C. Hernandez-Monteagudo, D. Herranz, S. R. Hildebrandt, E. Hivon, M. Hobson, W. A. Holmes, A. Hornstrup, W. Hovest, Z. Huang, K. M. Huffenberger, G. Hurier, A. H. Jaffe, T. R. Jaffe, W. C. Jones, M. Juvela, E. Keihanen, R. Keskitalo, T. S. Kisner, R. Kneissl, J. Knoche, L. Knox, M. Kunz, H. Kurki-Suonio, G. Lagache, A. Lahteenmaki, J. M. Lamarre, A. Lasenby, M. Lattanzi, C. R. Lawrence, J. P. Leahy, R. Leonardi, J. Lesgourgues, F. Levrier, A. Lewis, M. Liguori, P. B. Lilje, M. Linden-Vornle, M. Lopez-Caniego, P. M. Lubin, J. F. Macias-Perez, G. Maggio, D. Maino, N.

Mandolesi, A. Mangilli, A. Marchini, P. G. Martin, M. Martinelli, E. Martinez-Gonzalez, S. Masi, S. Matarrese, P. Mazzotta, P. McGehee, P. R. Meinhold, A. Melchiorri, J. B. Melin, L. Mendes, A. Mennella, M. Migliaccio, M. Millea, S. Mitra, M. A. Miville-Deschenes, A. Moneti, L. Montier, G. Morgante, D. Mortlock, A. Moss, D. Munshi, J. A. Murphy, P. Naselsky, F. Nati, P. Natoli, C. B. Netterfield, H. U. Norgaard-Nielsen, F. Noviello, D. Novikov, I. Novikov, C. A. Oxborrow, F. Paci, L. Pagano, F. Pajot, R. Paladini, D. Paoletti, B. Partridge, F. Pasian, G. Patanchon, T. J. Pearson, O. Perdereau, L. Perotto, F. Perrotta, V. Pettorino, F. Piacentini, M. Piat, E. Pierpaoli, D. Pietrobon, S. Plaszczynski, E. Pointecouteau, G. Polenta, L. Popa, G. W. Pratt, G. Prezeau, S. Prunet, J. L. Puget, J. P. Rachen, W. T. Reach, R. Rebolo, M. Reinecke, M. Remazeilles, C. Renault, A. Renzi, I. Ristorcelli, G. Rocha, C. Rosset, M. Rossetti, G. Roudier, B. R. D'Orfeuil, M. Rowan-Robinson, J. A. Rubino-Martin, B. Rusholme, N. Said, V. Salvatelli, L. Salvati, M. Sandri, D. Santos, M. Savelainen, G. Savini, D. Scott, M. D. Seiffert, P. Serra, E. P. S. Shellard, L. D. Spencer, M. Spinelli, V. Stolyarov, R. Stompor, R. Sudiwala, R. Sunyaev, D. Sutton, A. S. Suur-Uski, J. F. Sygnet, J. A. Tauber, L. Terenzi, L. Toffolatti, M. Tomasi, M. Tristram, T. Trombetti, M. Tucci, J. Tuovinen, M. Turler, G. Umana, L. Valenziano, J. Valiviita, B. Van Tent, P. Vielva, F. Villa, L. A. Wade, B. D. Wandelt, I. K. Wehus, M. White, S. D. M. White, A. Wilkinson, D. Yvon, A. Zacchei, and A. Zonca, "Planck 2015 results. XIII. Cosmological parameters," *A&A*, vol. 594, no. A13, p. 63, 2015. arXiv:1502.01589.

[106] B. Smith, S. Sigurdsson, and T. Abel, "Metal cooling in simulations of cosmic structure formation," *MNRAS*, vol. 385, no. 3, pp. 1443–1454, 2008. arXiv:0706.0754.

[107] P. S. Behroozi, R. H. Wechsler, and H.-Y. Wu, "THE ROCKSTAR PHASE-SPACE TEMPORAL HALO FINDER AND THE VELOCITY OFFSETS OF CLUSTER CORES," *ApJ*, vol. 762, no. 2, p. 109, 2013. arXiv:1110.4372.

[108] J. L. Tinker, A. V. Kravtsov, A. Klypin, K. Abazajian, M. S. Warren, G. Yepes, S. Gottlober, and D. E. Holz, "Toward a halo mass function for precision cosmology: the limits of universality," *ApJ*, vol. 688, no. 2, pp. 709–728, 2008. arXiv:0803.2706.

[109] G. Altay and J. Wise, "Rabacus: A Python Package for Analytic Cosmological Radiative Transfer Calculations," *Astron. Comput.*, vol. 10, pp. 73–87, 2015. arXiv:1502.02798.

[110] D. Tseliakhovich, R. Barkana, and C. M. Hirata, "Suppression and spatial variation of early galaxies and minihaloes," *MNRAS*, vol. 418, no. 2, pp. 906–915, 2011.

[111] T. H. Greif, V. Springel, S. D. M. White, S. C. O. Glover, P. C. Clark, R. J. Smith, R. S. Klessen, and V. Bromm, "SIMULATIONS ON A MOVING MESH: THE CLUSTERED FORMATION OF POPULATION III PROTOSTARS," *ApJ*, vol. 737, no. 2, p. 75, 2011.

[112] A. Stacy, V. Bromm, and A. Loeb, "EFFECT OF STREAMING MOTION OF BARYONS RELATIVE TO DARK MATTER ON THE FORMATION OF THE FIRST STARS," *ApJ*, vol. 730, no. 1, p. L1, 2011.

[113] K. Ahn, "How Density Environment Changes the Influence of the Dark Matter-Baryon Streaming Velocity on the Cosmological Structure Formation," *ApJ*, vol. 830, no. 2, p. 15, 2016. arXiv:1603.09356.

[114] D. Koh and J. H. Wise, "Amplification of magnetic fields in a primordial H ii region and supernova," *MNRAS*, vol. 462, no. 1, pp. 81–91, 2016.

[115] J. M. Wagstaff, R. Banerjee, D. Schleicher, and G. Sigl, "Magnetic field amplification by the small-scale dynamo in the early Universe," *Phys. Rev. D*, vol. 89, no. 10, p. 103 001, 2014.

[116] A. Neronov and I. Vovk, "Evidence for strong extragalactic magnetic fields from Fermi observations of TeV blazars.," *Science*, vol. 328, no. 5974, pp. 73–5, 2010. arXiv:1006.3504.

[117] S. Naoz and R. Narayan, "Generation of primordial magnetic fields on linear overdensity scales.," *Phys. Rev. Lett.*, vol. 111, no. 5, p. 051 303, 2013.

[118] H. Susa, K. Hasegawa, and N. Tominaga, "THE MASS SPECTRUM OF THE FIRST STARS," *ApJ*, vol. 792, no. 1, p. 32, 2014.

[119] N. Yoshida, K. Omukai, and L. Hernquist, "Formation of Massive Primordial Stars in a Reionized Gas," *ApJ*, vol. 667, no. 2, pp. L117–L120, 2007.

[120] A. Stacy, V. Bromm, and A. T. Lee, "Building up the Population III initial mass function from cosmological initial conditions," *MNRAS*, vol. 462, no. 2, pp. 1307–1328, 2016. arXiv:1603.09475.

[121] J. Tumlinson and J. M. Shull, "Zero-Metallicity Stars and the Effects of the First Stars on Reionization," *ApJ*, vol. 528, no. 2, pp. L65–L68, 2000.

[122] D. Schaerer, "On the properties of massive Population III stars and metal-free stellar populations," *A&A*, vol. 382, no. 1, pp. 28–42, 2002.

[123] J. P. Ostriker and C. F. McKee, "Astrophysical blastwaves," *Rev. Mod. Phys.*, vol. 60, no. 1, pp. 1–68, 1988.

[124] T. H. Greif, S. C. O. Glover, V. Bromm, and R. S. Klessen, "THE FIRST GALAXIES: CHEMICAL ENRICHMENT, MIXING, AND STAR FORMATION," *ApJ*, vol. 716, no. 1, pp. 510–520, 2010.

[125] E. J. King and P. Coles, "Amplification of primordial magnetic fields by anisotropic gravitational collapse," *MNRAS*, vol. 365, no. 4, pp. 1288–1294, 2006. arXiv:0508370 [astro-ph].

[126] D. R. G. Schleicher, D. Galli, S. C. O. Glover, R. Banerjee, F. Palla, R. Schneider, and R. S. Klessen, "THE INFLUENCE OF MAGNETIC FIELDS ON THE THERMODYNAMICS OF PRIMORDIAL STAR FORMATION," *ApJ*, vol. 703, no. 1, pp. 1096–1106, 2009.

[127] C. Federrath, S. Sur, D. R. G. Schleicher, R. Banerjee, and R. S. Klessen, "A NEW JEANS RESOLUTION CRITERION FOR (M)HD SIMULATIONS OF SELF-GRAVITATING GAS: APPLICATION TO MAGNETIC FIELD AMPLIFICATION BY GRAVITY-DRIVEN TURBULENCE," *ApJ*, vol. 731, no. 1, p. 62, 2011.

[128] M. J. Turk, J. S. Oishi, T. Abel, and G. L. Bryan, "MAGNETIC FIELDS IN POPULATION III STAR FORMATION," *ApJ*, vol. 745, no. 2, p. 154, 2012.

[129] A. Dedner, F. Kemm, D. Kröner, C.-D. Munz, T. Schnitzer, and M. Wesenberg, "Hyperbolic Divergence Cleaning for the MHD Equations," *J. Comput. Phys.*, vol. 175, no. 2, pp. 645–673, 2002.

[130] P. Wang and T. Abel, "MAGNETOHYDRODYNAMIC SIMULATIONS OF DISK GALAXY FORMATION: THE MAGNETIZATION OF THE COLD AND WARM MEDIUM," *ApJ*, vol. 696, no. 1, pp. 96–109, 2009.

[131] Planck Collaboration, P. A. R. Ade, N. Aghanim, C. Armitage-Caplan, M. Arnaud, M. Ashdown, F. Atrio-Barandela, J. Aumont, C. Baccigalupi, A. J. Banday, R. B. Barreiro, J. G. Bartlett, E. Battaner, K. Benabed, A. Benoît, A. Benoit-Lévy, J.-P. Bernard, M. Bersanelli, P. Bielewicz, J. Bobin, J. J. Bock, A. Bonaldi, J. R. Bond, J. Borrill, F. R. Bouchet, M. Bridges, M. Bucher, C. Burigana, R. C. Butler, E. Calabrese, B. Cappellini, J.-F. Cardoso, A. Catalano, A. Challinor, A. Chamballu, R.-R. Chary, X. Chen, H. C. Chiang, L.-Y Chiang, P. R. Christensen, S. Church, D. L. Clements, S. Colombi, L. P. L. Colombo, F. Couchot, A. Coulais, B. P. Crill, A. Curto, F. Cuttaia, L. Danese, R. D. Davies, R. J. Davis, P. de Bernardis, A. de Rosa, G. de Zotti, J. Delabrouille, J.-M. Delouis, F.-X. Désert, C. Dickinson, J. M. Diego, K. Dolag, H. Dole, S. Donzelli, O. Doré, M. Douspis, J. Dunkley, X. Dupac, G. Efstathiou, F. Elsner, T. A. Enßlin, H. K. Eriksen, F. Finelli, O. Forni, M. Frailis, A. A. Fraisse, E. Franceschi, T. C. Gaier, S. Galeotta, S. Galli, K. Ganga, M. Giard, G. Giardino, Y. Giraud-Héraud, E. Gjerløw, J. González-Nuevo, K. M.

Górski, S. Gratton, A. Gregorio, A. Gruppuso, J. E. Gudmundsson, J. Haissinski, J. Hamann, F. K. Hansen, D. Hanson, D. Harrison, S. Henrot-Versillé, C. Hernández-Monteagudo, D. Herranz, S. R. Hildebrandt, E. Hivon, M. Hobson, W. A. Holmes, A. Hornstrup, Z. Hou, W. Hovest, K. M. Huffenberger, A. H. Jaffe, T. R. Jaffe, J. Jewell, W. C. Jones, M. Juvela, E. Keihänen, R. Keskitalo, T. S. Kisner, R. Kneissl, J. Knoche, L. Knox, M. Kunz, H. Kurki-Suonio, G. Lagache, A. Lähteenmäki, J.-M. Lamarre, A. Lasenby, M. Lattanzi, R. J. Laureijs, C. R. Lawrence, S. Leach, J. P. Leahy, R. Leonardi, J. León-Tavares, J. Lesgourgues, A. Lewis, M. Liguori, P. B. Lilje, M. Linden-Vørnle, M. López-Caniego, P. M. Lubin, J. F. Macías-Pérez, B. Maffei, D. Maino, N. Mandolesi, M. Maris, D. J. Marshall, P. G. Martin, E. Martínez-González, S. Masi, M. Massardi, S. Matarrese, F. Matthai, P. Mazzotta, P. R. Meinhold, A. Melchiorri, J.-B. Melin, L. Mendes, E. Menegoni, A. Mennella, M. Migliaccio, M. Millea, S. Mitra, M.-A. Miville-Deschênes, A. Moneti, L. Montier, G. Morgante, D. Mortlock, A. Moss, D. Munshi, J. A. Murphy, P. Naselsky, F. Nati, P. Natoli, C. B. Netterfield, H. U. Nørgaard-Nielsen, F. Noviello, D. Novikov, I. Novikov, I. J. O'Dwyer, S. Osborne, C. A. Oxborrow, F. Paci, L. Pagano, F. Pajot, R. Paladini, D. Paoletti, B. Partridge, F. Pasian, G. Patanchon, D. Pearson, T. J. Pearson, H. V. Peiris, O. Perdereau, L. Perotto, F. Perrotta, V. Pettorino, F. Piacentini, M. Piat, E. Pierpaoli, D. Pietrobon, S. Plaszczynski, P. Platania, E. Pointecouteau, G. Polenta, N. Ponthieu, L. Popa, T. Poutanen, G. W. Pratt, G. Prézeau, S. Prunet, J.-L. Puget, J. P. Rachen, W. T. Reach, R. Rebolo, M. Reinecke, M. Remazeilles, C. Renault, S. Ricciardi, T. Riller, I. Ristorcelli, G. Rocha, C. Rosset, G. Roudier, M. Rowan-Robinson, J. A. Rubiño-Martín, B. Rusholme, M. Sandri, D. Santos, M. Savelainen, G. Savini, D. Scott, M. D. Seiffert, E. P. S. Shellard, L. D. Spencer, J.-L. Starck, V. Stolyarov, R. Stompor, R. Sudiwala, R. Sunyaev, F. Sureau, D. Sutton, A.-S. Suur-Uski, J.-F. Sygnet, J. A. Tauber, D. Tavagnacco, L. Terenzi, L. Toffolatti, M. Tomasi, M. Tristram, M. Tucci, J. Tuovinen, M. Türler, G. Umana, L. Valenziano, J. Valiviita, B. Van Tent, P. Vielva, F. Villa, N. Vittorio, L. A. Wade, B. D. Wandelt, I. K. Wehus, M. White, S. D. M. White, A. Wilkinson, D. Yvon, A. Zacchei, and A. Zonca, "Planck 2013 results. XVI. Cosmological parameters," *A&A*, vol. 571, J. Tauber, Ed., A16, 2014. arXiv:1303.5076.

[132] J. H. Wise, T. Abel, M. J. Turk, M. L. Norman, and B. D. Smith, "The birth of a galaxy II. The role of radiation pressure," *MNRAS*, vol. 427, no. 1, pp. 311–326, 2012. arXiv:1206.1043.

[133] J. H. Wise and T. Abel, "The Number of Supernovae from Primordial Stars in the Universe," *ApJ*, vol. 629, no. 2, pp. 615–624, 2005.

[134] M. J. Turk, B. D. Smith, J. S. Oishi, S. Skory, S. W. Skillman, T. Abel, and M. L. Norman, "yt: A MULTI-CODE ANALYSIS TOOLKIT FOR ASTROPHYSICAL SIMULATION DATA," *ApJS*, vol. 192, no. 1, p. 9, 2011.

[135] K. Dolag, M. Kachelriess, S. Ostapchenko, and R. Tomàs, "LOWER LIMIT ON THE STRENGTH AND FILLING FACTOR OF EXTRAGALACTIC MAGNETIC FIELDS," *ApJ*, vol. 727, no. 1, p. L4, 2011.

[136] J. H. Wise and T. Abel, "Enzo+Moray: Radiation Hydrodynamics Adaptive Mesh Refinement Simulations With Adaptive Ray Tracing," *MNRAS*, vol. 414, no. 4, pp. 3458–3491, 2011.

[137] M. A. Latif, D. R. G. Schleicher, and W. Schmidt, "Magnetic fields during the formation of supermassive black holes," *MNRAS*, vol. 440, no. 2, pp. 1551–1561, 2014.

[138] J. H. Wise and T. Abel, "Resolving the Formation of Protogalaxies. I. Virialization," *ApJ*, vol. 665, no. 2, pp. 899–910, 2007.

[139] D. Seifried, R. Banerjee, and D. Schleicher, "Supernova explosions in magnetized, primordial dark matter haloes," *MNRAS*, vol. 440, no. 1, pp. 24–39, 2014.

[140] R. M. O'Leary and M. McQuinn, "THE FORMATION OF THE FIRST COSMIC STRUCTURES AND THE PHYSICS OF THE z 20 UNIVERSE," *ApJ*, vol. 760, no. 1, p. 4, 2012.

[141] G. A. Wade and MiMeS Collaboration, "Review: Magnetic fields of O stars," *Phys. Evol. Magn. Relat. Stars*, vol. 494, p. 30, 2014. arXiv:1411.3604.

[142] M. A. Latif and D. R. G. Schleicher, "Magnetic fields in primordial accretion disks," *A&A*, vol. 585, A151, 2016.

[143] J. Schober, D. R. G. Schleicher, and R. S. Klessen, "Magnetic field amplification in young galaxies," *A&A*, vol. 560, A87, 2013. arXiv:1310.0853.

[144] B. E. Robertson, R. S. Ellis, J. S. Dunlop, R. J. McLure, and D. P. Stark, "Early star-forming galaxies and the reionization of the Universe.," *Nature*, vol. 468, no. 7320, pp. 49–55, 2010.

[145] A. Mesinger, "Was reionization complete by z ˜ 5-6?," *MNRAS*, vol. 407, no. 2, pp. 1328–1337, 2010. arXiv:0910.4161.

[146] G. D. Becker, J. S. Bolton, P. Madau, M. Pettini, E. V. Ryan-Weber, and B. P. Venemans, "Evidence of patchy hydrogen reionization from an extreme Ly-alpha trough below redshift six," *MNRAS*, vol. 447, no. 4, pp. 3402–3419, 2015. arXiv:1407.4850.

[147] C. J. Willott, P. Delorme, C. Reyle, L. Albert, J. Bergeron, D. Crampton, X. Delfosse, T. Forveille, J. B. Hutchings, R. J. McLure, A. Omont, and D. Schade, "The Canada-France High-z Quasar Survey: nine new quasars and the luminosity function at redshift 6," *ApJ*, vol. 139, no. 3, pp. 906–918, 2010. arXiv:0912.0281.

[148] R. L. Grissom, D. R. Ballantyne, and J. H. Wise, "On the contribution of active galactic nuclei to reionization (Research Note)," *A&A*, vol. 561, p. 5, 2013. arXiv:1312.1358.

[149] P. Madau and F. Haardt, "Cosmic Reionization after Planck: Could Quasars Do It All?," *Astrophys. J. Lett.*, vol. 813, no. 1, p. L8, 2015. arXiv:1507.07678.

[150] P. Madau, F. Haardt, and M. J. Rees, "Radiative Transfer in a Clumpy Universe: III. The Nature of Cosmological Ionizing Sources," *ApJ*, vol. 514, no. 2, pp. 648–659, 1999. arXiv:9809058 [astro-ph].

[151] M. Kuhlen and C. A. Faucher-Giguere, "Concordance models of reionization: implications for faint galaxies and escape fraction evolution," *MNRAS*, vol. 423, no. 1, pp. 862–876, 2012. arXiv:1201.0757.

[152] M. A. Alvarez, K. Finlator, and M. Trenti, "Constraints on the Ionizing Efficiency of the First Galaxies," *Astrophys. J. Lett.*, vol. 759, no. 2, 2012. arXiv:1209.1387.

[153] I. T. Iliev, G. Mellema, P. R. Shapiro, P. McDonald, and U.-L. Pen, "Large-scale Radiative Transfer Simulations of Reionization: Models and Observability," *Edge Universe Latest Results from Deep. Astron. Surv. ASP Conf. Ser.*, vol. 380, 2007.

[154] H. Trac and N. Y. Gnedin, "Computer Simulations of Cosmic Reionization," *Adv. Sci. Lett.*, vol. 4, no. 2, pp. 228–243, 2011. arXiv:0906.4348.

[155] I. T. Iliev, G. Mellema, K. Ahn, P. R. Shapiro, Y. Mao, and U.-L. Pen, "Simulating cosmic reionization: how large a volume is large enough?," *MNRAS*, vol. 439, no. 1, pp. 725–743, 2014.

[156] S. R. Furlanetto, M. Zaldarriaga, and L. Hernquist, "THE GROWTH OF H ii REGIONS DURING REIONIZATION," *ApJ*, vol. 613, pp. 1–15, 2004.

[157] A. Mesinger and S. Furlanetto, "Efficient Simulations of Early Structure Formation and Reionization," *ApJ*, vol. 669, no. 2, pp. 663–675, 2007. arXiv:0704.0946.

[158] O. Zahn, A. Lidz, M. McQuinn, S. Dutta, L. Hernquist, M. Zaldarriaga, and S. R. Furlanetto, "Simulations and Analytic Calculations of Bubble Growth during Hydrogen Reionization," *ApJ*, vol. 654, no. 1, pp. 12–26, 2007.

[159] O. Zahn, A. Mesinger, M. McQuinn, H. Trac, R. Cen, and L. E. Hernquist, "Comparison of reionization models: radiative transfer simulations and approximate, seminumeric models," *MNRAS*, vol. 414, no. 1, pp. 727–738, 2011.

[160] K. Ahn, I. T. Iliev, P. R. Shapiro, G. Mellema, J. Koda, and Y. Mao, "DETECTING THE RISE AND FALL OF THE FIRST STARS BY THEIR IMPACT ON COSMIC REIONIZATION," *ApJ*, vol. 756, no. 1, p. L16, 2012.

[161] J. H. Wise, V. G. Demchenko, M. T. Halicek, M. L. Norman, M. J. Turk, T. Abel, and B. D. Smith, "The birth of a galaxy - III. Propelling reionization with the faintest galaxies," *MNRAS*, vol. 442, no. 3, pp. 2560–2579, 2014.

[162] A. Mesinger, S. Furlanetto, and R. Cen, "21cmfast: a fast, seminumerical simulation of the high-redshift 21-cm signal," *MNRAS*, vol. 411, no. 2, pp. 955–972, 2011. arXiv:1003.3878.

[163] B. Greig and A. Mesinger, *The Global History of Reionisation*, 2016. arXiv:1605.05374.

[164] S. R. Furlanetto, M. McQuinn, and L. Hernquist, "Characteristic Scales During Reionization," *MNRAS*, vol. 365, no. 1, pp. 115–126, 2005. arXiv:0507524 [astro-ph].

[165] N. Y. Gnedin, "Effect of Reionization on the Structure Formation in the Universe," *ApJ*, vol. 542, no. 2, pp. 535–541, 2000. arXiv:0002151 [astro-ph].

[166] T. Kimm and R. Cen, "Escape fraction of ionizing photons during reionization: effects due to supernova feedback and runaway OB stars," *ApJ*, vol. 788, no. 2, p. 121, 2014. arXiv:1405.0552.

[167] J. H. Wise and R. Cen, "Ionizing Photon Escape Fractions From High-Redshift Dwarf Galaxies," *ApJ*, vol. 693, no. 1, pp. 984–999, 2009. arXiv:0808.2477.

[168] J.-P. Paardekooper, S. Khochfar, and C. D. Vecchia, "The First Billion Years Project: The escape fraction of ionizing photons in the epoch of reionization," *MNRAS*, vol. 451, no. 3, pp. 2544–2563, 2015. arXiv:1501.01967.

[169] B. W. O'Shea, J. H. Wise, H. Xu, and M. L. Norman, "The Ultraviolet Luminosity Function of the Earliest Galaxies," *ApJ*, vol. 807, no. 1, p. L12, 2015. arXiv:arXiv:1503.01110v1.

[170] P. S. Behroozi, R. H. Wechsler, H.-Y. Wu, M. T. Busha, A. A. Klypin, and J. R. Primack, "GRAVITATIONALLY CONSISTENT HALO CATALOGS AND MERGER TREES FOR PRECISION COSMOLOGY," *ApJ*, vol. 763, no. 1, p. 18, 2013. arXiv:1110.4370.

[171] H. Xu, J. H. Wise, M. L. Norman, K. Ahn, and B. W. O'Shea, "Galaxy Properties and UV Escape Fractions During Epoch of Reionization: Results from the Renaissance Simulations," p. 17, 2016. arXiv:1604.07842.

[172] P. F. Hopkins, D. Keres, J. Onorbe, C.-A. Faucher-Giguere, E. Quataert, N. Murray, and J. S. Bullock, "Galaxies on FIRE (Feedback In Realistic Environments): Stellar Feedback Explains Cosmologically Inefficient Star Formation," *MNRAS*, vol. 445, no. 1, pp. 581–603, 2014. arXiv:1311.2073.

[173] J. Schaye, R. A. Crain, R. G. Bower, M. Furlong, M. Schaller, T. Theuns, C. D. Vecchia, C. S. Frenk, I. G. McCarthy, J. C. Helly, A. Jenkins, Y. M. Rosas-Guevara, S. D. M. White, M. Baes, C. M. Booth, P. Camps, J. F. Navarro, Y. Qu, A. Rahmati, T. Sawala, P. A. Thomas, and J. Trayford, "The EAGLE project: Simulating the evolution and assembly of galaxies and their environments," *MNRAS*, vol. 446, no. 1, pp. 521–554, 2014. arXiv:1407.7040.

[174] A. H. Pawlik, A. Rahmati, J. Schaye, M. Jeon, and C. D. Vecchia, "The Aurora radiation-hydrodynamical simulations of reionization: calibration and first results," *eprint arXiv:1603.00034*, 2016. arXiv:1603.00034.

[175] T. Okamoto, L. Gao, and T. Theuns, "Massloss of galaxies due to a UV-background," *MNRAS*, vol. 390, no. 3, pp. 920–928, 2008. arXiv:0806.0378.

[176] D. Schaerer, "The transition from Population III to normal galaxies: Ly-a and HeII 1640 emission and the ionising properties of high redshift starburst galaxies," *A&A*, vol. 397, pp. 527–538, 2003. arXiv:0210462 [astro-ph].

[177] A. H. Pawlik, J. Schaye, and E. van Scherpenzeel, "Keeping the Universe ionised: Photo-heating and the clumping factor of the high-redshift intergalactic medium," *MNRAS*, vol. 394, no. 4, pp. 1812–1824, 2008. arXiv:0807.3963.

[178] E. Sobacchi and A. Mesinger, "Inhomogeneous recombinations during cosmic reionization," *MNRAS*, vol. 440, no. 2, pp. 1662–1673, 2014.

[179] A. L. Muratov, O. Y. Gnedin, N. Y. Gnedin, and M. Zemp, "Revisiting The First Galaxies: The effects of Population III stars on their host galaxies," *ApJ*, vol. 772, no. 2, p. 13, 2012. arXiv:1212.0909.

[180] H. Xu, M. L. Norman, B. W. O'Shea, and J. H. Wise, "Late Pop III Star Formation During the Epoch of Reionization: Results from the Renaissance Simulations," *ApJ*, vol. 823, no. 2, 2016. arXiv:1604.03586.

[181] M. Sharma, T. Theuns, C. S. Frenk, R. G. Bower, R. A. Crain, M. Schaller, and J. Schaye, "The brighter galaxies reionised the Universe," *MNRAS*, vol. 458, no. 1, pp. L94–L98, 2016. arXiv:1512.04537.

[182] Y. Lin, S. P. Oh, S. R. Furlanetto, and P. M. Sutter, "The Distribution of Bubble Sizes During Reionization," *MNRAS*, vol. 461, no. 3, pp. 3361–3374, 2015. arXiv:1511.01506.

[183] A. Paranjape and T. R. Choudhury, "An improved model of HII bubbles during the epoch of reionization," *MNRAS*, vol. 442, no. 2, pp. 1470–1482, 2014. arXiv:1401.7994.

[184] P. Ocvirk, N. Gillet, P. R. Shapiro, D. Aubert, I. T. Iliev, R. Teyssier, G. Yepes, J.-H. Choi, D. Sullivan, A. Knebe, S. Gottloeber, A. D'Aloisio, H. Park, Y. Hoffman, and T. Stranex, "Cosmic Dawn (CoDa): the First Radiation-Hydrodynamics Simulation of Reionization and Galaxy Formation in the Local Universe," *MNRAS*, 2015. arXiv:1511.00011.

[185] J Arons and R McCray, *The Astrophysical journal.* Published for the American Astronomical Society by IOS Publishing [etc.], 1970, vol. 5, p. 123.

[186] D. Koh and J. H. Wise, "Extending Semi-numeric Reionisation Models to the First Stars and Galaxies," 2016. arXiv:1609.04400.

[187] F. Haardt and P. Madau, "Radiative transfer in a clumpy universe: IV. New synthesis models of the cosmic UV/X-ray background," *ApJ*, vol. 746, no. 2, 2012. arXiv:1105.2039.